CALIFORNIA
ENERGY COMMISSION

CALIFORNIA
NATURAL
RESOURCES
AGENCY

ENERGY RESEARCH AND DEVELOPMENT DIVISION

FINAL PROJECT REPORT

Scaling Reliable, Next-Generation Perovskite Solar Cell Modules

June 2024 | CEC-500-2024-029

PREPARED BY:

Prof. David P. Fenning
Yanqi Luo
Shen Wang
Deniz Çakan
Prof. Shirley Meng
Moses Kodur
Rory Runser
So-Yeon Ham
Mincheol Kim
Prof. Darren Lipomi
University of California, San Diego
Primary Authors

Kaycee Chang
Prab Sethi
Project Manager
California Energy Commission

Agreement Number: EPC-16-050

Kevin Uy
Branch Manager
ENERGY GENERATION RESEARCH OFFICE

Jonah Steinbuck, Ph.D.
Director
ENERGY RESEARCH AND DEVELOPMENT DIVISION

Drew Bohan
Executive Director

ACKNOWLEDGEMENTS

Use of the Center for Nanoscale Materials and the Advanced Photon Source, both Office of Science facilities, was supported by the U.S. Department of Energy, Office of Science, Office of Basic Energy Sciences, under Contract No. DE-AC02-06CH11357. This work was performed in part at the San Diego Nanotechnology Infrastructure (SDNI) of U.C. San Diego, a member of the National Nanotechnology Coordinated Infrastructure, which was supported by the National Science Foundation (Grant ECCS-1542148).

PREFACE

The California Energy Commission's (CEC) Energy Research and Development Division supports energy research and development programs to spur innovation in energy efficiency, renewable energy and advanced clean generation, energy-related environmental protection, energy transmission, and distribution and transportation.

In 2012, the Electric Program Investment Charge (EPIC) was established by the California Public Utilities Commission to fund public investments in research to create and advance new energy solutions, foster regional innovation, and bring ideas from the lab to the marketplace. The EPIC Program is funded by California utility customers under the auspices of the California Public Utilities Commission. The CEC and the state's three largest investor-owned utilities—Pacific Gas and Electric Company, San Diego Gas and Electric Company, and Southern California Edison Company—were selected to administer the EPIC funds and advance novel technologies, tools, and strategies that provide benefits to their electric ratepayers.

The CEC is committed to ensuring public participation in its research and development programs that promote greater reliability, lower costs, and increase safety for the California electric ratepayer and include:

- Providing societal benefits.
- Reducing greenhouse gas emission in the electricity sector at the lowest possible cost.
- Supporting California's loading order to meet energy needs first with energy efficiency and demand response, next with renewable energy (distributed generation and utility scale), and finally with clean, conventional electricity supply.
- Supporting low-emission vehicles and transportation.
- Providing economic development.
- Using ratepayer funds efficiently.

For more information about the Energy Research and Development Division, please visit the CEC's research website (www.energy.ca.gov/research/) or contact the Energy Research and Development Division at ERDD@energy.ca.gov.

ABSTRACT

Hybrid halide perovskite materials emerged onto the photovoltaic (PV) research scene in 2009 and have since exploded in international research efforts, producing a meteoric rise in perovskite solar-to-electricity power conversion to rival that of silicon solar cells. Perovskite solar cells operate by combining an inorganic ion framework that creates an electronic structure for photovoltaics with organic ions. The nature of the perovskites allows synthesis of the cells at temperatures at or above 212°F (100°C) and manufacturing that can be as easy as printing a newspaper. Perovskite solar cells thus far, however, have not been stable under operating conditions for more than a few months – a far cry from the decades of durability provided by current commercial PV technologies.

This project advances technologies that stabilize perovskite PVs at the absorber, cell, and module levels to ensure robust reliability while enabling manufacturability. A large-area, scalable electrosynthesis approach for specific elements of the perovskite-based solar cells is explored. Research is also advanced into the chemistry of the current conducting layers that make contact with the perovskites. The project also evaluated large-area single-layer graphene synthesis and its use as an environmental barrier layer, produced by California-based startup and project partner GrollTex, Inc. To demonstrate the breakthrough advances in solar cell efficiency and reliability achieved, perovskite solar cell modules were fabricated at small scales and tested under laboratory conditions. Modules were also tested in an outdoor installation at a rooftop research facility at the University of California, San Diego.

Keywords: halide perovskite, solar cells, efficiency, graphene, manufacturing

Please use the following citation for this report:

Fenning, David P., Moses Kodur, Yanqi Luo, Rory Runser, Shen Wang, So-Yeon Ham, Deniz Çakan, Mincheol Kim, Shirley Meng, Darren Lipomi. 2021. *Scaling Reliable, Next-Generation Perovskite Solar Cell Modules*. California Energy Commission. Publication Number: CEC-500-2024-029.

TABLE OF CONTENTS

LIST OF FIGURES

Executive Summary

Introduction

Solar photovoltaic technology presents an enormous opportunity for contributing to California's ambitious global-warming emissions reduction and other related environmental mandates: the sun radiates more energy to Earth's surface in one hour than humans use in roughly one year. Solar photovoltaic cells convert this sunlight directly to electricity. Today's photovoltaics industry, however, relies predominantly on silicon-based technology, which requires both high capital costs and extremely pure materials, which in turn presents challenges for integrating solar photovoltaics into the electric grid. Perovskite solar cell materials, which are man-made semiconductor materials with similar properties to silicon, have recently emerged and could potentially address both cost and integration challenges.

Since their discovery, perovskite solar cells have failed to meet efficiency and durability requirements for commercialization; however, recent advances at laboratory scale have pushed their power conversion efficiency to greater than 25 percent, making them one of the most efficient solar technologies in existence today. These perovskite solar cells can be fabricated in a comparably simple process at low temperatures, holding a promise for dramatically cutting solar costs.

Challenges remain, however, because perovskite technology can be sensitive to moisture and degrades rapidly when dampness enters the cell, impacting both reliability and durability. Although promising, the photovoltaic industry still shows limited interest in perovskite commercialization despite in-lab demonstrations of high efficiencies. This project aims to demonstrate that improved efficiency, reliability, and durability of perovskite solar cells could prove the viable commercialization of this technology.

Project Purpose

The University of California, San Diego team developed a more robust perovskite absorber layer (the light-absorbing "engine" that powers the solar cell) and packaged these absorbers within materials that prevent water from entering the cells, improving both overall durability and reliability.

Part of the project objective was to lower the cost of perovskite solar cells and increase the economic competitiveness of photovoltaic manufacturing by reducing materials and manufacturing costs. The project focused on improving the reliability of the perovskite solar cells by increasing their relative efficiency to at least 80 percent (compared with initial efficiency) after 1,000 hours of testing in the lab. The team also explored an innovative perovskite manufacturing prototype that increases the size of the cells from a few square inches to more than three square feet, moving costs below the readily achievable by standard commercial silicon PVs manufactured internationally.

Project Approach

The team's focus was to advance the efficiency and durability of perovskite solar cells to achieve more than the 10-year product lifetime necessary to commercialize this technology. This required improvements at the absorber, cell, and module levels to ensure robust cell reliability while ensuring that the product can be manufactured cost effectively. A solar cell is a device that is unpackaged. A module is a solar cell that is packaged with encapsulation. First, the team developed a large-area, scalable electrodeposition approach for the synthesis of the perovskite absorbers, which rely on low-cost methods similar to those employed for glass coatings. Second, building on current research of the chemical makeup of the perovskites, the team redesigned the critical absorber layer to increase both the stability and manufacturability of the solar cells. Third, the project team explored the use of graphene as an environmental barrier layer to protect the perovskite solar cell and produce large-area single-layer absorber layers. This graphene technology is a single layer of carbon atoms produced in a honey-comb pattern and is the thinnest, lightest, and strongest compound known. It is licensed by startup and project partner GrollTex, Inc., which produced these unique barrier layers for the solar cells. Last, 24 solar cells were installed on a rooftop facility to test and measure results while simultaneously tracking the cells' performance under operating conditions.

During the project, the team dealt with non-technical challenges related to the COVID-19 pandemic, which affected the project team's efforts for module integration and testing, which in turn required a carefully orchestrated sequence to produce and integrate the layers. Although the team focused on testing the viability of the technology, learning was hampered and not ideal. Further outdoor testing will be required to validate the merit of the accelerated tests applied to this new technology.

Project Results

This project produced significant fundamental scientific and technical knowledge related to the engineering of the perovskite solar absorber and its carrier selective contact layers, scaling the device design, and designing for operational stability.

The project team successfully used the new absorber materials to improve stability. Perovskite solar-cell prototypes fabricated with carefully prepared alloy compositions exhibited more than 20 percent power conversion efficiency, which is the percentage of solar energy converted into electricity. Success was also achieved in fabricating high-quality perovskite solar cell prototypes to produce high-performing, stabilized perovskite films and devices with large surface areas.

In a degradation study of some of the project team's highest performing perovskite solar cells, silver electrodes performed similarly to gold electrodes at lower cost and higher stability. Project results also suggested that the addition of graphene in rigid, non-flexible, long-lasting applications is insufficient for generating a highly stable device. Project findings pointed, ultimately, to glass-glass encapsulation (with polyisobutylene edge seals) as sufficient for perovskite solar cell encapsulation.

Technology and Knowledge Transfer

The project team shared its critical advances to the scientific and academic communities and relevant industry stakeholders in photovoltaics, printing, and electrochemical processing. The project team published 16 articles in leading scientific journals regarding the technology and knowledge developed in this project, including *Nature, Advanced Functional Materials*, and *Advanced Materials*. The results were also presented to several photovoltaics industry players interested in project development. This knowledge transfer to industry resulted in one follow-on collaborative project led by an industry partner that will be supported by the United States Department of Energy for technology research, development, and demonstration. In addition, the project team provided findings at several meetings of professional societies and industry, including in-state conferences and national meetings, including the:

- Institute of Electrical and Electronics Engineers Photovoltaic Specialists Conference.
- University of California Solar Symposium.
- Spring Materials Research Society.
- Emerging Material Technologies Summit.
- Molecular Foundry User Meeting.

Benefits to California

This project advanced perovskite solar-cell technology by improving the efficiency, durability, and reliability of solar cells. Perovskite solar cells could drastically reduce the cost of photovoltaics while enabling applications beyond large capital projects, therefore providing more opportunities for electricity generation. Perovskites also have the potential to further reduce greenhouse gas emissions (over silicon solar technology) due to their low manufacturing temperature and capability for mass production. This project successfully extended the durability of perovskite solar cells to thousands of hours of operation, demonstrating that a low-cost photovoltaic solar cell is possible, which could ultimately reduce the cost to California ratepayers.

Advanced training of an innovative energy workforce is key to achieving California’s current and future statutory goals. The project supported up to 10 people working at UC San Diego, working 87 person-months during the project. This project also contributed to the education and training of at least seven graduate students and two postdoctoral researchers.

CHAPTER 1: Introduction

University of California, San Diego (UCSD) divided the next-generation perovskite solar cell project into the following five technical tasks to accomplish the goals of this project. The approach and results for each task are presented in the following chapters:

- CHAPTER 2 Perovskite Absorber Development: Synthesize stable, high-performing perovskite solar absorbers using the chemical flexibility of the perovskite crystal. Technical barriers addressed included alloying the perovskite absorber by combining a chemical vapor transport method with electrodeposition synthesis of the inorganic framework of the perovskite.
- CHAPTER 3 Hole Transport Layer Development: Evaluated the scalability of the hole transport layer materials commonly used in perovskite solar cells. The tendency of the most common hole transport layer to degrade in the presence of water was examined by varying the ratio of additives in a detailed study. The project team also validated the low-cost electrosynthesis of polymer hole transport layers that are currently prohibitively expensive if purchased in their polymeric form.
- CHAPTER 4: Develop and characterize graphene barrier layers for use in perovskite solar cell modules. Large-area synthesis of graphene was performed using GrollTex, Inc.'s proprietary process, which enabled realistic testing of barrier layer performance.
- CHAPTER 5: Integrate project advancements into high-efficiency perovskite solar cells to achieve 20 percent power conversion efficiency (PCE).
- CHAPTER 6: Fabricate and test operation of encapsulated solar cell mini-modules in challenging outdoor environments (rooftop installation on the UCSD campus) and in accelerated testing in the laboratory.

Introduction to Halide Perovskites

This chapter focuses on developing the composition and synthesis of the halide perovskite absorber, the light-absorbing engine that powers the solar cell.

Perovskites are a class of crystal structure. The perovskite crystal has three unique atomic sites to its makeup: the A, B, and X sites that sit within a repeating cubic arrangement in the crystal (Figure 1). This same cube repeats over and over in space to create the ABX_3 ratio of elements that corresponds to the perovskite structure.

Figure 1: The Basics of Perovskite Solar Cells

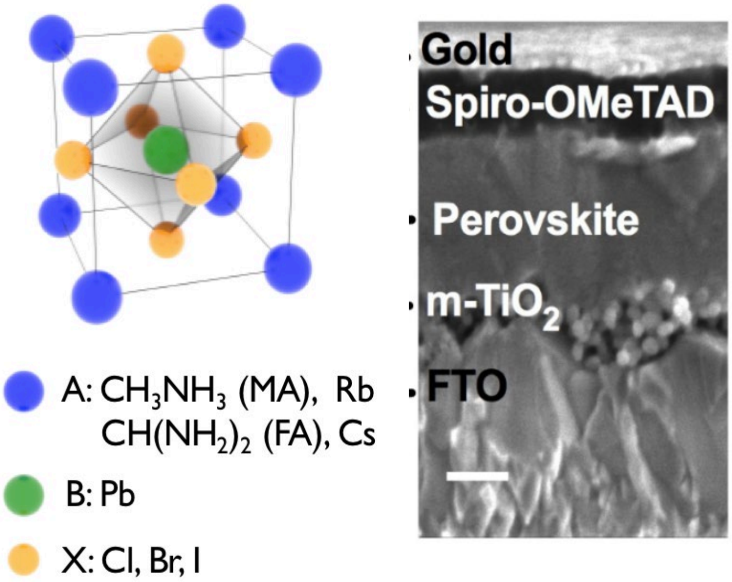

The perovskite structure (left) is flexibly substituted with different elements. The perovskite absorber (middle) is sandwiched between negative contact materials below it and positive contact materials above it.

Source: University of California, San Diego

Halide perovskite solar absorbers include the A-site, B-site, and X-site. The A-site is filled with organic cations (for example, methylammonium, MA, or formamidinium, FA) and/or inorganic cations (for example, cesium, Cs^+, rubidium, Rb^+), the B-site typically has lead, Pb^{2+}, or tin, Sn^{2+}, and the X-site has halides (chloride, Cl^-, bromide, Br^-, or iodide, I^-). Sunlight excites electrons within the perovskite, and with appropriate contacts to conduct charge out of the absorber, solar energy can be captured. Unfortunately, the perovskite absorbers are sensitive to moisture and will degrade over time in the presence of moisture. The goal of this project was to develop more robust perovskite chemistries, and to package these absorbers within materials that prevent water entry.

Typically, the hybrid perovskite solar absorber is sandwiched between positive and negative charge collecting layers, called the hole and electron transport layers, respectively. Sunlight excites electrons within the perovskite material in the middle of the cell, and electrons are transported out of the cell through the electron transport layer; the front transparent conducting oxide contact, and holes are transported out of the back of the cell via the hole transport layer in the opposite direction of the electrons.

CHAPTER 2:
Perovskite Absorber Development

Absorber Compositional Space Design

The purpose of this task was to synthesize stable, high-performing perovskite solar absorbers using the chemical flexibility of the perovskite crystal. The University of California, San Diego, divided this task into four subtasks to accomplish the goals of this project. The first subtask was to design the compositional space of the absorber.

Somewhat surprisingly, the champion performance came from a composition that exhibited strong performance only if the films were annealed with the existence of moisture (outside of a glovebox). This feature may be beneficial for scaling manufacturing in a less restrictive environment.

The project team found that the prototype devices often showed some performance degradation over a day of constant operation but exhibited self-recovery if stored in the dark for a subsequent 16 hours. Mild heating of the degraded device in the dark promoted a faster recovery process. Such performance recovery may be potentially applicable as needed overnight when the solar cell is idle.

The project team found that the perovskite composition homogenizes upon the addition of alkali halides, so used advanced microscopy techniques to understand why. Adding compositional complexity was shown by others in the field to lead to improved initial performance, but at times could also lead to undesired phase segregation that reduces durability. The project team found that compositions that successfully achieved more homogeneous material exhibited improved figures for solar cells and spatially homogenous optical and electrical properties. These insights provided a more comprehensive understanding of the role of alkali cations in alloyed perovskites. From these insights, the project team provided new guidance to further improve the performance and stability of perovskite solar cells (PSCs).

The team also concluded that substituting out lead for other materials could improve consumer acceptance of PSCs. Synthesis of lead-free perovskites and scrutiny of their usefulness for solar cell applications is needed to identify a suitable substitution. Inspired by anticipation of a new library of lead-free double perovskite and perovskite-like compounds from computational chemistry, the project team synthesized several new-to-science lead-free double perovskites based on their formability prediction and tested both their crystal structure and optoelectronic properties. These efforts did not ultimately identify a highly promising lead-free candidate.

Another avenue to make PSCs more environmentally friendly is to reduce the concentration of lead. The project team investigated the unconventional alloying of lead-based PSCs with a larger B-site cation, Ba^{2+}. Ba-alloyed perovskites show improved optoelectronic properties and a higher phase transition temperature, which may improve the thermal stability of PSCs under operating conditions.

The best performing and stable absorbers, with novel chemistries, were selected and integrated into functional solar cells, as described in CHAPTER 5 and CHAPTER 6.

A-Site Cation Mixing

The goal of A-site cation mixing was to obtain high-performing absorbers by incorporating different types and various concentrations of A-site cations. A-site mixing or alloying is a proven approach to stabilizing the perovskites away from the photo-inactive yellow phase (δ-$FAPbI_3$). This phase can be stabilized by adding MA^+ ions, as reported in literature. This chemistry is also known as a double cation (FA^+ and MA^+) perovskite, which is used as the baseline in the absorber development. The project team's approach to produce a stable black perovskite phase was to increase the chemistry complexity on both the A-site and X-site.

Absorbers prepared with different alkali ion additions produced films with different structural properties. Results from the absorbers appear in Figure 2. The black lines imposed on X-ray diffraction (XRD) measurements indicate the non-photoactive phases or compositions in the films. The peaks associated with the undesirable phases indicated by the black lines are fully suppressed upon 5 percent CsI and 5 percent RbI additions, which also yield the highest PCE in solar cells.

Figure 2: Structure and Device Performance of Absorbers With a Wide Range of A-site Cation Mixing

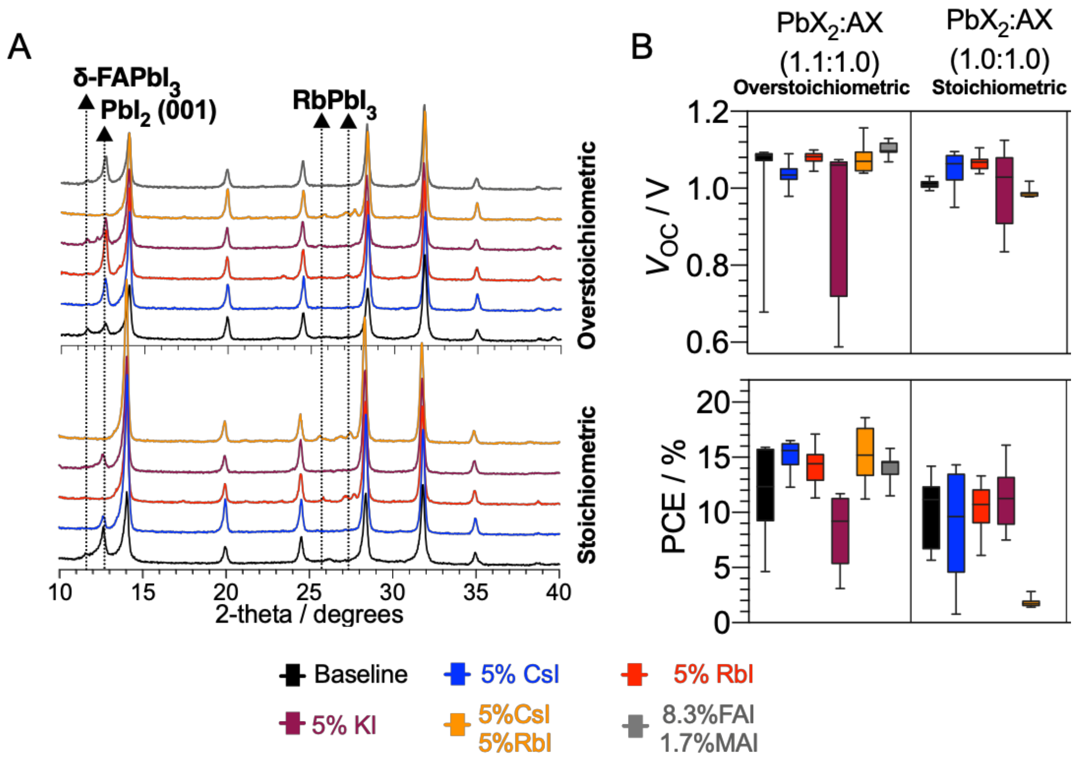

(A) X-ray Diffraction (XRD) spectrum for absorbers with different alkali ion additions and stoichiometric rations between lead halide and organic halide. (B) Device performance of absorbers in solar cells

Source: University of California, San Diego

The project team first highlights innovation in perovskite absorber chemistry for performance and stability. The typical state-of-the-art perovskite absorber has a complex chemistry and is comprised of six different elements (C, H, N, Pb, I, and Br), which creates a challenge in producing a homogeneous film — like a good puree — rather than a phase-segregated and poor-quality film. The research team's insight is that a homogenous perovskite absorber can be obtained through incorporation of alkali salts such as cesium iodide (CsI) and rubidium iodide (RbI). Using the advanced X-ray microscopy toolset, the project team found what appears to be counterintuitive: by adding more elements, specifically cesium (Cs) and rubidium (Rb), the perovskite film can be homogenized to achieve higher efficiencies, improve stability, and achieve tighter performance tolerances because the solar-cell processing is easier.

The project team found that improvement in the chemical uniformity of the absorber strongly correlates with enhanced device performance. Among the layers, the quality of perovskite absorber is critical in determining the overall device performance since that is where the photovoltaic (PV) energy conversion takes place. The team's breakthrough in perovskite absorber chemistry (as part of the California Energy Commission [CEC] project) was published in the journal *Science* (Correa-Baena et al., *Science*, 363 [6427], 627, 2019).

To show advances in perovskite absorber design, the project team directly imaged the elemental segregation common to any perovskite without the Cs and Rb additions, using X-ray fluorescence microscopy. An example is seen in Figure 3, where the project team observed dark regions deficient in the important halide Br. As shown, the degree of segregation decreases when 5 percent CsI, 5 percent RbI, or 5 percent CsI and 5 percent RbI alkali salts are added, yielding a more uniform Br:Pb distribution. Devices fabricated with alkali salt incorporation also displayed better PCE. Devices without alkali salts have a wider range of PCE, while samples with alkali additions have narrower ranges.

Figure 3: Perovskite Device Architecture and Elemental Distribution of Br in Absorbers with A-Site Cation Mixing

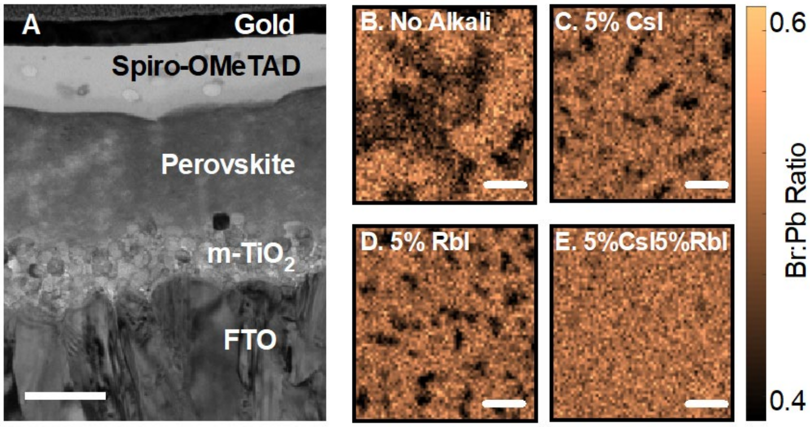

A) Cross-section of a perovskite cell. B-D) X-ray fluorescence mapping of Br:Pb ratio for differing nominal film composition. Scale bar is 5 µm.

Source: University of California, San Diego

Adding CsI and RbI yields the highest PCE device among the sample set, with 18.3 percent PCE.

This work led to significant advancement in the development of perovskites, indicated by its garnering well over 150 citations at the time of this report.

Lead-Free Exploration

Substituting lead (Pb) remains part of the effort to make environmental-friendly PSCs. Synthesis of lead-free perovskite and scrutinization of their usefulness for solar cell applications is needed to find a suitable substitution. Inspired by the prediction of a new library of lead-free double perovskite and perovskite-like compounds from computational chemistry from the research team's colleagues at UC San Diego (Li, Y., and Kesong, Y., 2019), the project team attempted to synthesize several new-to-science lead-free double perovskites based on computational prediction that they would be stable and tested their crystal structure and optoelectronic properties.

Based on its near-ideal tolerance factor, the project team focused on a nominal MA_2NaInI_3 double perovskite. This targeted perovskite has heterovalent B-sites, which if ordered on the B-site, could give rise to interesting optoelectronic and charge separating phenomena. Precursor solutions were prepared at 1M 2:1:1 MAI/NaI/InI_3 in DMSO. The precursor solutions were drop cast onto glass substrates that were treated with oxygen plasma to enhance wettability while the substrates were on a hotplate to form crystals for subsequent XRD measurement. The crystals were then examined by XRD and UV-VIS-NIR spectroscopy to understand the physical and optical properties.

The XRD pattern of the targeted $(MA)_2NaInI_6$ did not match that predicted by density functional theory calculation, though it did contain minimal precursor peaks, suggesting a largely single-phase outcome (Figure 4). Meanwhile, the extrapolated 2 eV band gap from absorbance spectrum showed great potential of this material for solar-cell applications.

Figure 4: Structure and Absorption Properties of Lead-Free Perovskites

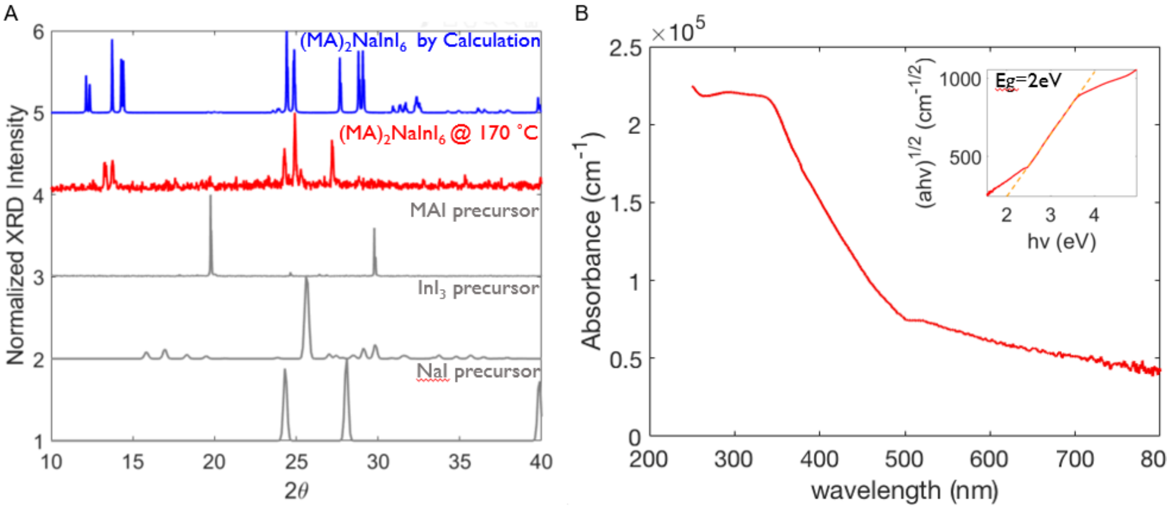

(A) X-ray Diffraction patterns of calculated (blue) lead-free double perovskite $(MA)_2NaInI_6$, synthesized (red) $(MA)_2NaInI_6$, precursors (gray) MAI, InI_3 and NaI from ICSD database. (B) Absorbance Spectrum of synthesized $(MA)_2NaInI_6$ thin film on quartz and extrapolated bandgap around 2 eV from Tauc plot.

Source: University of California, San Diego

Additional analysis by single-crystal X-ray diffraction showed the compound to be $MAInI_4$ with space group $P2_1/c$. This novel compound has been reported to the Cambridge Crystallographic Data Centre structural database. Further efforts at synthesis of the Na-In double perovskite were unsuccessful.

A separate effort was made to synthesize the double perovskite $MA_2ZnCdBr_6$ by similar solution processing. The resulting product was MA_2ZnBr_4 ($P2_1/c$). These results indicated the challenge of B-site modification in the hybrid perovskite structure.

B-Site Alloying

Another dimension to improve the stability of the photoactive hybrid perovskite and to reduce the Pb content is by alloying B-site with Pb. B-site-alloying targets, a necessary objective for development of high-efficiency PSCs. This remains an outstanding challenge: to energetically favor the black phase (α-$FAPbI_3$ (FA = formamidinium) relative to the photo-inactive yellow phase (δ-$FAPbI_3$, at both room and elevated temperatures). This effort pursues strain engineering to stabilize the high-performance photoactive perovskite phase: α-$FAPbI_3$. The slightly larger Ba cation offers a new dimension to alloying on the B-site and contrasts with previous efforts in the community using smaller A-site cations (methylammonium, Cs, and Rb) and smaller anions (Br, Cl) to stabilize α-$FAPbI_3$.

A dominant fraction of the A-site occupied by an organic dipolar cation appears to be critical to achieving the highest efficiencies. However, methylammonium is likely incommensurate with fielded temperatures, where it is volatile. Achieving a stable, near-pure $FAPbI_3$ absorber is a long-sought goal.

The project team focused on engineering stability and bandgap via the B-site. Considering the tolerance factor, enlarging the B-site can be analogous to shrinking the A-site. By incorporating the larger Ba^{2+} cation (R_{Ba}=1.35Å, R_{Pb} = 1.19Å (Shannon, R.D., 1976), the tolerance factor decreases in $FABa_xPb_{1-x}I_3$, suggesting improved formability.

Figure 5 shows enhanced performance and stability, with Ba added. The thin film resulted in larger grains and smoother surfaces as shown in Figure 5, which is beneficial for solar cell materials with long diffusion lengths like perovskite. Stronger photoluminescence (PL) intensity of Ba-alloyed perovskite further indicated the improved photoelectronic properties of Ba-alloyed perovskite. Ba-alloyed perovskite also has a high thermal-phase transition temperature, which can improve the thermal stability of PSCs under operational conditions.

Figure 5: Enhanced Performance and Stability With Ba Added

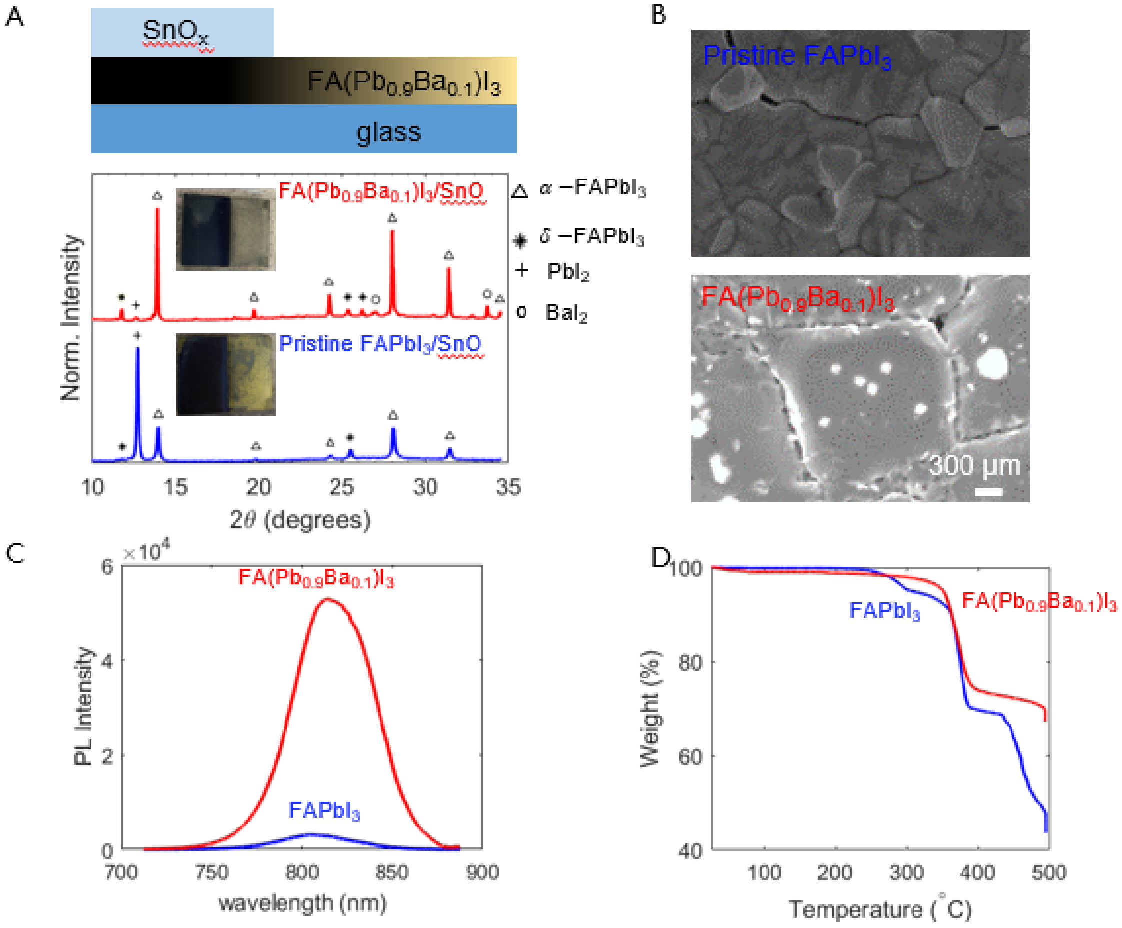

(A) X-ray diffraction patterns of pristine FAPbI3 and $FA(Pb_{0.9}Ba_{0.1})I_3$ under SnO_x encapsulation shows that Ba-alloyed perovskite remains in photoactive α-phase while the pristine perovskite degrades to unwanted δ-phase under room temperature. (B) Scanning Electron Microscopy images shows that Ba-alloyed perovskite has larger and smoother grains than the pristine perovskite, which is beneficial for perovskite solar cells. (C) Photoluminescence spectra show that Ba-alloyed perovskite has more photon yields. (D) Thermogravimetric Analyzer shows high thermal phase transition temperature of Ba-alloyed perovskite.

Source: University of California, San Diego

Development of Large-Area Film Deposition

Electrochemical Deposition for Fabricating Large-Area Perovskite Absorbers

The goal of this subtask was to develop an electrochemical method to fabricate large area perovskite solar cells (PSC). Electrochemical deposition techniques have shown great potential to deposit uniform layers in scaled-up fabrication process, including barrier coating on battery electrodes and metal contacts in interconnect (IC) technology (Frau, A, et al., 2010). Although a spin-coating approach has been utilized commonly in the semiconductor industry, it is challenging to have uniform layers in module-sized solar cells due to thickness variations perpendicular to the rotational axis (Scriven, L.E., 1988). Thus, to fabricate large-area higher performing perovskite modules, the project team adapted the electrochemical deposition method to achieve uniform deposition of the active absorber layer. Unlike the spin-coating technique, the thickness and quality of deposited thin film (using an electrochemical approach) relies on the applied current density and duration, which can be precisely tuned and controlled.

When using the electrochemical deposition method, the project team's approach to perovskite film formation involved two steps. The first was the deposition of lead oxide (PbO_x) via electrochemistry, and the second step was converting PbO_x into perovskites. Each step was individually optimized to successfully carry out the large-area deposition for cell and module applications.

Absorber deposition when using the electrochemistry technique involved two component developments that required independent optimization approaches. The first focused on the optimization of PbO_x layers deposited via the electrochemical method, which had success criteria such as film morphology, film coverage, and film thickness. The other component involved the conversion of PbO_2 to $APbX_3$ perovskites, which was optimized based on the quality of the absorber (including structural and optoelectronic performance). The detailed development on this effort was summarized separately in APPENDIX A. The project team scaled this approach to cover many square centimeters (Figure 6).

Figure 6: Large-Area Perovskite Absorber

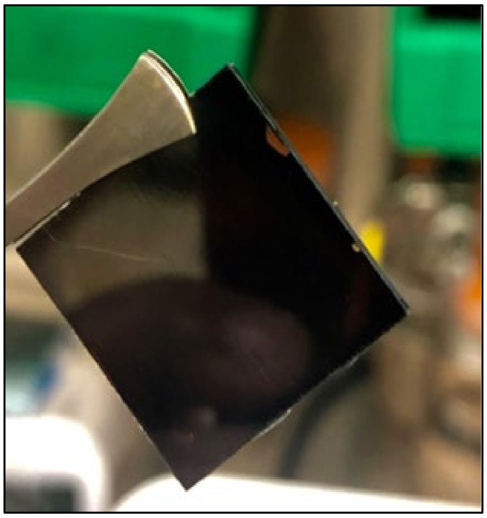

Photograph of the electrodeposited and converted perovskite large-area film

Source: University of California, San Diego

Using the chemical vapor conversion approach, the project team fabricated working solar cells using lead iodide (PbI_2) as the seed layer. The current density-voltage (JV) measurement, along with device parameters, is shown in Figure 7. This first vapor-converted device had PCE in the range of 3.5 to 4.9 percent. Although device performance was low in current development, the JV results provided both the possibility and potential to use a vapor-conversion method as the scaled-up approach.

Figure 7: Device Performance of a Device Prepared by Chemical-Vapor Conversion

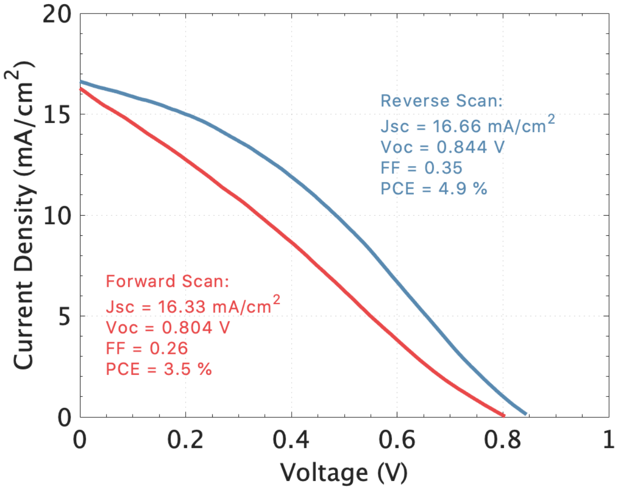

Current density-voltage curve for forward and reverse scan is shown as the red and blue line.

Source: University of California, San Diego

Outlook: Electrodeposition and Conversion of Perovskite Absorbers

Electrochemical deposition of PbO_x and its conversion to FA-containing perovskites showed initial success. Further investigation and optimization are needed to create high-performing PSCs over larger areas. In the subtask of electrodeposition, factors such as reactant concentration, applied current density, and electrolyte temperature were explored to achieve films with lower amounts of PbO_x clusters. Solution and vapor conversion methods were explored for the conversion subtask. Vapor conversion showed better results than solution conversion in terms of film coverage and smooth-surface morphology. Combining results from both electrodeposition and vapor conversion, reducing micron size PbO_x appears critical when adapting vapor conversion at scale. Unlike solution conversion, seed-layer morphology was carried onto the final converted perovskite films during vapor conversion.

CHAPTER 3:
Hole Transport Layer Development

This chapter describes the project team's results in evaluating the scalability of hole transport layer (HTL) materials, including examining varying ratios of additives to address water degradation and validating low-cost electrosynthesis of polymer HTLs.

The Role of the Hole Transport Layer in Perovskite Solar Cells

In the hole transport layer (HTL), holes are transported from the valence band of the perovskite to the contact while simultaneously blocking the passage of excited electrons. The perovskite generates electron-hole pairs after the absorption of photons from sunlight. The electrons can then be collected at the electron transport layer, so the electrons go to the external circuit. The electrons can later be recaptured by the hole transport layer to close the circuit. Ideally, there is no compositional change during the entire cycle that could thwart the long-term stability of the device.

The ideal HTL should have high-hole mobility (at least $>10^{-4}$ [$cm^2\ V^{-1}\ s^{-1}$]), close alignment with the valence-band maximum of perovskite materials, good conductivity, and high stability. Organic, inorganic, and polymeric materials are all part of the hole-transport layer in PSCs.

Figure 8 shows the project team's research progress related the development of HTLs suitable for the PSC supported from the CEC Electric Program Investment Charge (EPIC) Advance Breakthrough award (EPC-16-050). The main research goal was to apply cheap, effective, and stable HTL materials for the development of highly efficient PSCs with low manufacturing costs and superior device stability.

Figure 8: A Brief Summary of the Perovskite Solar Cells HTL Research for the CEC Project

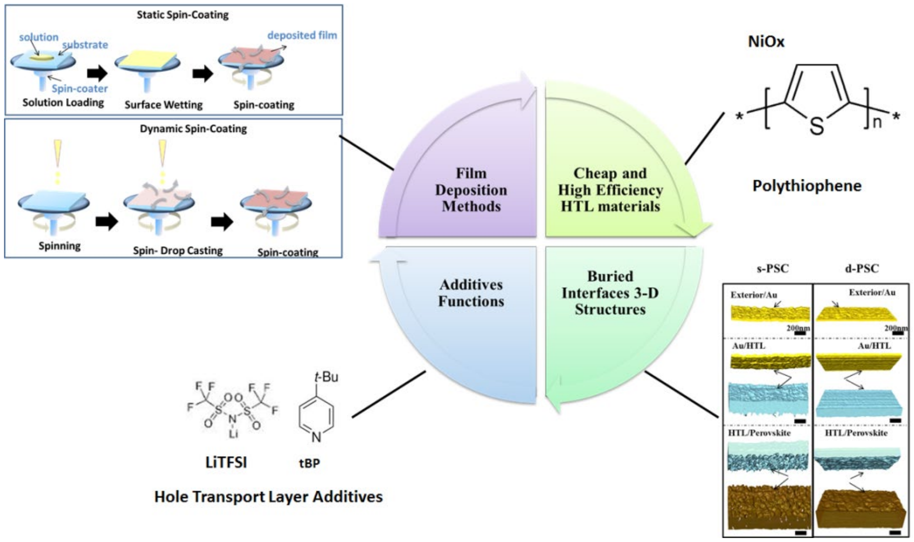

Source: University of California, San Diego

Typical HTL Chemistry and Tradeoffs

In general, there are three types of HTL materials in PSCs: molecular, polymeric, and inorganic.

Organic molecular materials can be easily dissolved in an organic solvent and, because of their small size, develop conformal contact with the perovskite layer (no matter which morphology the perovskite is in). Their physical properties can be adjusted by modifying their functional groups. Moreover, organic molecular materials have low price potential since the majority of the elements in these types of HTLs are abundant elements such as carbon, hydrogen, and nitrogen.

One of the most frequently applied molecular hole transport materials in PSCs is 2,2,7,7-tetrakis(N,N-di-p-methoxyphenylamine)-9,9-spirobifluorene (Spiro-OMeTAD). This material was applied to dye-sensitized solar cells prior to its adaptation for use in PSCs.

Conducting polymers are another route often employed as the hole transport layer in PSCs and are responsible for some of the highest reported efficiencies to date. The project team developed experimental parameters for uniform electropolymerization and deposition of polythiophene from cheap precursors over large areas (4-100 cm^2). The project team applied the deposited films into PSCs, demonstrating that the electrodeposited polythiophene has the potential to become a scalable method for HTL fabrication. The method uses cheap precursors, is compatible with large-area substrates, uses fewer toxic chemicals than in previously published studies, and is not dependent upon an inert atmosphere for synthesis. Nevertheless, the performance of the electrodeposited hole transport layer must be improved before it is ready for broad implementation. Future work will focus on improving both the performance and the conformality.

Understanding Additive Interactions in the Hole Transport Layer

While LiTFSI and tBP are termed as ”additives” indicating that they are not major components, on a molecular level tBP and LiTFSI are essential components in the HTL. For Spiro-OMeTAD-based HTLs, the composition of HTL is dominated by LiTFSI and tBP showing these additives play a significant role in the chemical environment of HTL (Figure 9).

Figure 9: Hole Transport Layer Components and Optical Images of tBP-LiTFSI Mixtures at Different Molar Ratios

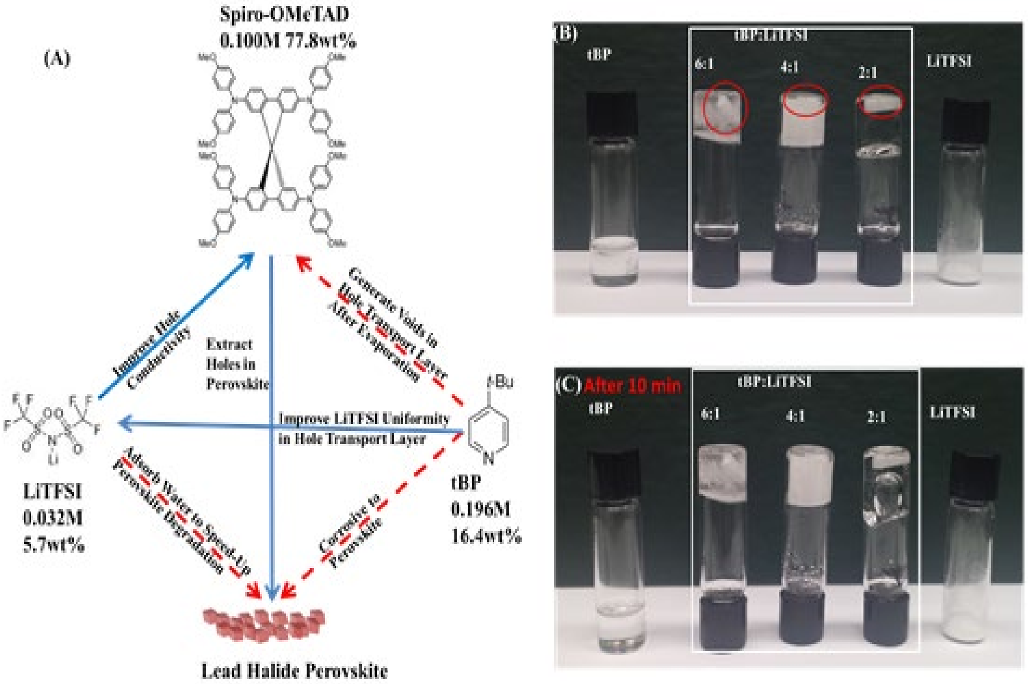

(A) Chemical structures of hole transport layer components (with molar concentration and weight percentage) in perovskite solar cells and interactions between the components and perovskite (the blue solid arrows show positive effects while the red dash arrows show negative effects). (B) tBP-LiTFSI mixtures in vials with black lids placed upside down (stir bars in the vials were marked with red circles). (C) tBP-LiTFSI mixtures after 10 min.

Source: University of California, San Diego

In this study, the formation of tBP-LiTFSI complexes at different molar ratios have been identified and characterized for the first time. Based on this study, in PSCs, the optimized tBP-LiTFSI molar ratio is 4:1, which shows better device stability, less hysteresis, and less variation in PCE. The understanding of interactions between tBP and LiTFSI shows pathways to further enhance the PSCs' performances and large-scale fabrications. This work, "*Unveiling the Role of tBP-LiTFSI Complexes in Perovskite Solar Cells,*" was published in the *Journal of the American Chemical Society* (Wang, S., et al., 2018).

To identify the formation of tBP-LiTFSI complexes, tBP and LiTFSI at various molar ratios were mixed together. At room temperature, tBP is liquid while LiTFSI is in a solid state. As shown in Figure 10, the 6:1, 4:1 and 2:1 mixtures have some distinguishable physical properties. The 6:1 mixture forms a gel, the 4:1 mixture is wax-like (without excess "free" liquid), and the 2:1 mixture forms a viscous liquid.

Detailed physical and chemical analyses, which can be found in the manuscript, suggested that the complex formation improves PSC stability. Planar PSCs were fabricated to test and understand the impact of these complexes on devices. Figure 10 shows the performance results, with over 60 PSCs fabricated to ensure statistically significant results. The PSCs consist of amorphous SnO_x as a compact electron transport layer, the planer $CH_3NH_3PbI_3$ intrinsic layer, Spiro-OMeTAD with tBP and LiTFSI HTL, and a gold-back contact.

Figure 10: PSC Performance Results for 60 Devices Fabricated With Different tBP:LiTFSI Ratios

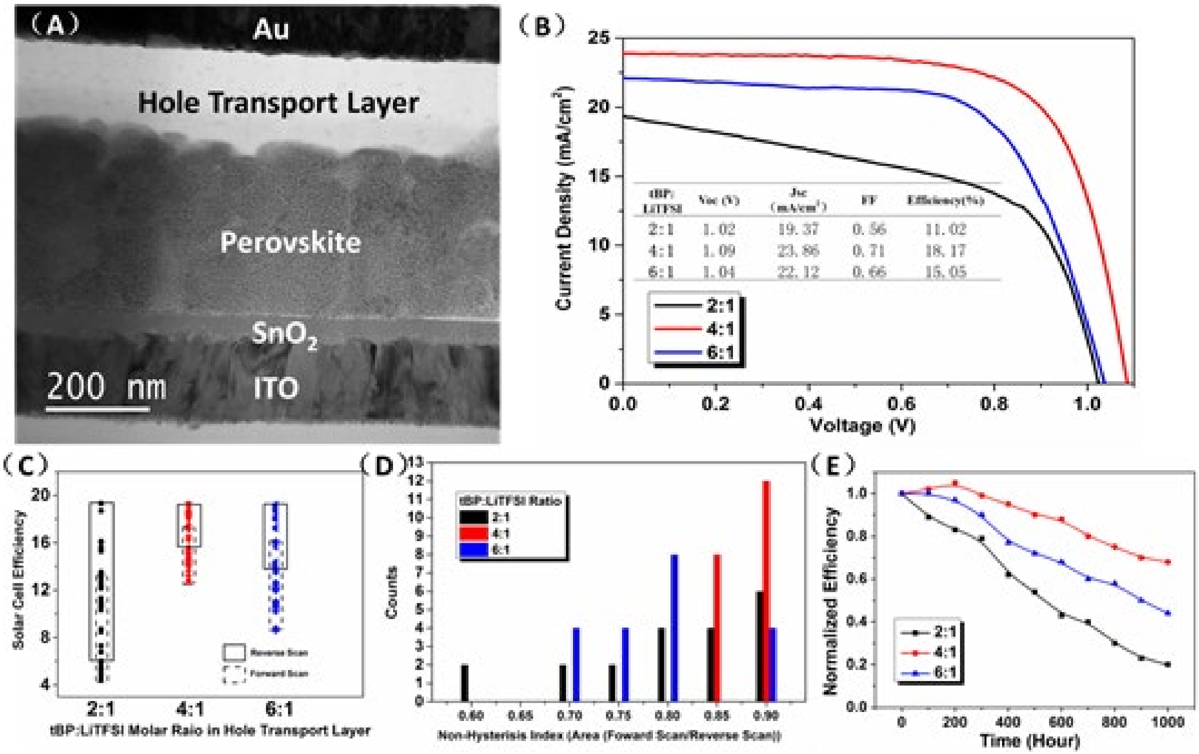

tBP: LiTFSI	Voc (V)	Jsc (mA/cm²)	FF	Efficiency(%)
2:1	1.02	19.37	0.56	11.02
4:1	1.09	23.86	0.71	18.17
6:1	1.04	22.12	0.66	15.05

PSC Performance Results for 60 devices (20 devices for each condition) fabricated with different tBP:LiTFSI ratios. (A) Bright Field Transmission Electron Microscope (BF-TEM) Cross-Section Image of the PSC. (B) Reverse scan JV curves, each curve is the average result for 20 devices. (C) Non-Hysteresis Index (the ratio of the area under the J-V curve for forward scan versus reverse scan) distribution. (D) Distribution of individual device performance plotted for all 60 devices. (E) Aging curves of the devices for 1000 hours in ambient condition. (The aging curves are only collected from the devices over 15 percent efficiency at the initial measurement; all data points are the average results.)

Source: University of California, San Diego

Electrochemical Polymerization as a Scalable Deposition Technique

Conducting polymers are often employed as the HTL in PSCs and are responsible for some of the highest reported efficiencies to date. Thiophene-based polymers are among the top performers, including poly(3-hexylthiophene) (P3HT) and poly(3,4-ethylenedioxythiophene) (PEDOT), which have demonstrated 22.7 percent (Jung, E.H. et al., 2019) and 18.7 percent (Kegelmann, L., et al., 2019) PCE, respectively. Unfortunately, both are expensive, with list prices at Sigma-Aldrich exceeding several hundred dollars per gram for PV-grade quality.

Yan et al. attempted to circumvent this issue by electrochemically polymerizing thiophene onto a transparent conducting electrode for use as the HTL in PSCs (Yan, W. et al., 2014). In this way, polythiophene (Figure 11) could be generated from the extremely low-cost thiophene monomer (<0.01$/g from Sigma-Aldrich), reducing the HTL material cost to a fraction of that of P3HT and other candidates. Furthermore, the electrochemical deposition technique allows for uniform film thickness over large areas (Kampmann, A., et al., 2000).

Figure 11: Molecular Structure of Polythiophene

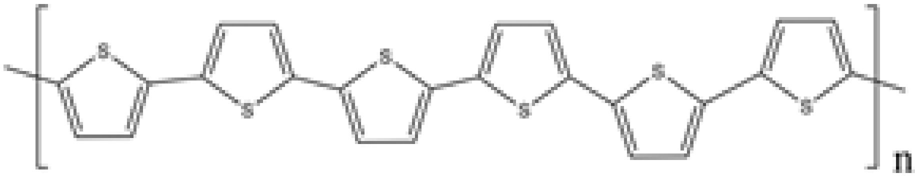

Source: University of California, San Diego

The project team developed experimental parameters for microscale and nanoscale uniform deposition of polythiophene from cheap precursors over large areas (4-100 cm2). The project team implemented the deposited films into inverted structure PSCs and investigated whether the method could additionally be applied to normal-structure PSCs.

Polythiophene Electrodeposition

The project team synthesized polythiophene following experimental parameters from a previous report (Krische, B., et al., 1989) and performed characterizations to verify its identity, established general electrochemical parameters for optimization of film uniformity, and applied the methodology to a large-area substrate. All films were deposited on indium tin oxide (ITO) working electrodes. All depositions were performed in ambient air to ensure that the overall process was suited for industrial implementation.

Large-Area Deposition

The electrochemical parameters developed for 2.5 x 2.5 cm^2 substrates were applied to a 10 x 10 cm^2 substrate. The deposition was done at 0.02 mA/cm^2 until reaching 5 mC/cm^2, with a working electrode-counter electrode separation of 0.5 cm (Figure 12). The resulting film appeared uniform to the naked eye, although there was some red hue from undoped polythiophene in the regions closest to the alligator clip. This non-uniform doping artifact can be easily mitigated by performing an additional doping step in thiophene-free electrolyte after polymerization.

Figure 12: Polythiophene Film Deposition

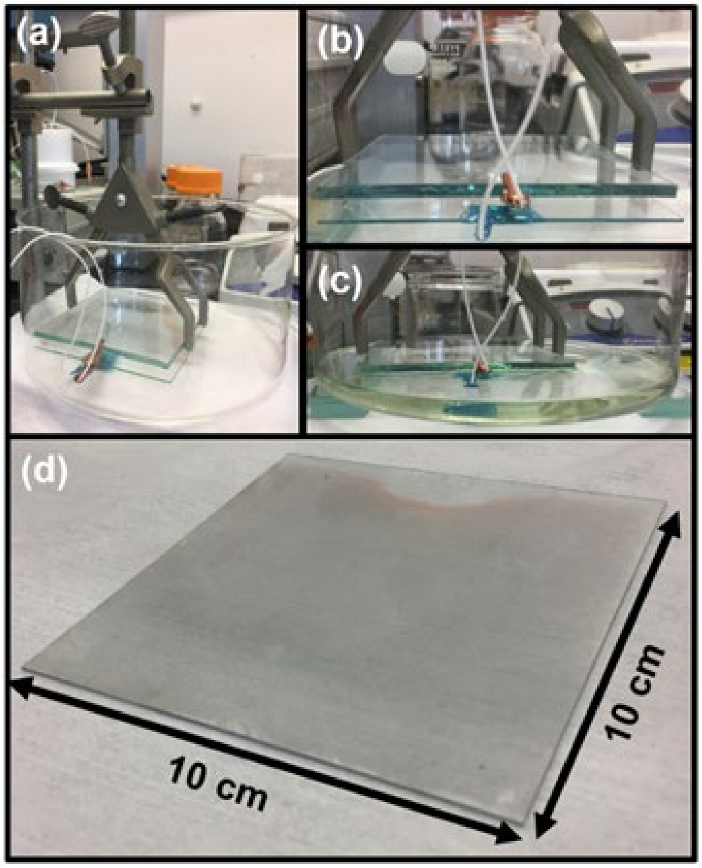

Electrochemical cell setup, before (A,B) and after (C) adding electrolyte. (D) 10 cm x 10 cm polythiophene film deposited on ITO.

Source: University of California, San Diego

Implementation Into Solar Cells

Polythiophene films were implemented into inverted structure solar cells as a targeted approach to verify whether they performed as an HTL in PSCs. The device architecture employed was ITO/polythiophene/$MAPbI_3$/phenyl-C61-butyric acid methyl ester (PCBM)/Au. The solar cell performance was diagnosed by running current-density voltage scans under AM1.5G illumination (100 mW/cm^2), where current density was recorded while voltage was swept from short-circuit (0 V) to open-circuit (V_{oc}).

The JV curves exhibited the characteristic shape expected for a PV device (Figure 13), so thus confirmed that polythiophene successfully performed its role as an HTL (for example, it demonstrated hole-accepting, hole-transporting, and electron-blocking properties). PCEs were normally in the 4.0 - 4.5 percent range, with the champion cell demonstrating a 6.97 percent PCE. The champion cell had a high short-circuit current density (Jsc) of 19.0 mA/cm^2, a mediocre open-circuit voltage (Voc) of 0.77 V, and a poor fill factor (FF) of 47.5 percent. The low FF and Voc imply a low shunt resistance (R_{shunt}).

Figure 13: Solar Cell Performance of Inverted Structure PSCs With Polythiophene as the HTL

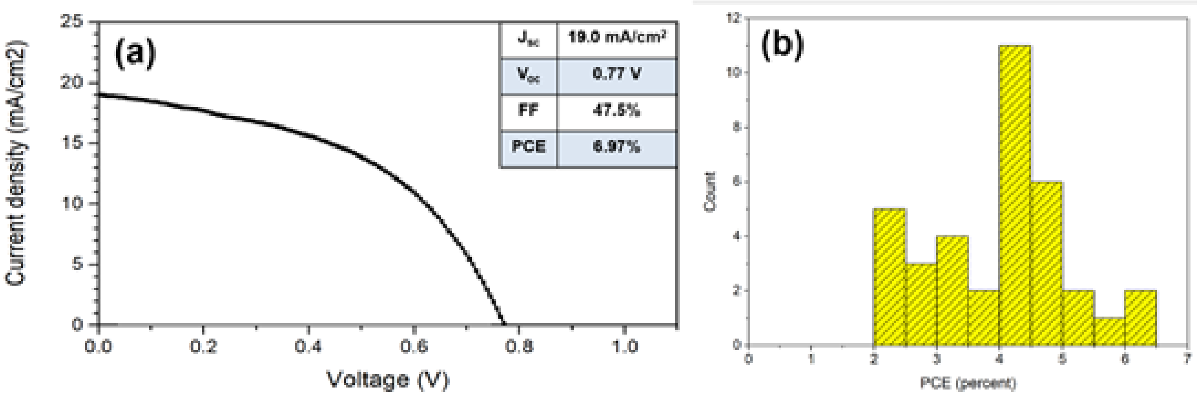

(a) JV curve and PV parameters of the champion cell. (b) Histogram of PCE efficiencies.

Source: University of California, San Diego

Future Promise and Critical Analysis

Inverted structure PSCs with electrodeposited polythiophene could potentially become a scalable method for HTL fabrication as it utilizes cheap precursors, is compatible with large-area substrates, uses fewer toxic chemicals than previously published studies, and is not dependent upon an inert atmosphere for synthesis. Nevertheless, the performance of the electrodeposited HTL in PSCs must be improved before it is ready for implementation (Jones-Albertus, R., et al., 2016). Future work will focus on improving the performance, that is, by applying surface treatments to the polythiophene films prior to perovskite deposition so that a more conformal polythiophene/perovskite interface is established.

Investigation of the Interface Between HTL and Metal Electrode and its Effect on Solar-Cell Stability

The time-dependent change in PV performance of PSCs employing silver (Ag) and gold (Au) electrodes was compared. Ag-based PSCs exhibit a clear s-shape kink in their JV curves in early stage; however, they recover to their best performance with 12 hours of aging time. On the other hand, Au-based PSCs perform their best at the beginning of testing.

To clarify this abnormal aging and recovery process in Ag-based PSCs, the project team investigated the time-dependent carrier dynamics alteration by PL and impedance spectroscopic methodologies as a function of aging time. By analyzing measurement and simulation results, the project team was able to verify that the work function difference between Ag and HTL materials, Spiro-MeOTAD, induces a significant injection barrier for holes, and it clearly caused the formation and alleviation of an s-shape kink in Ag-based PSCs. The project team finally demonstrated the potential of Ag electrodes for commercial use by demonstrating highly stable Ag-based PSCs over 350 hours under light-illumination, which is near the result of Au-based PSCs. Figure 14 shows different aging trends in device performance.

Figure 14: Different Aging Behavior of Perovskite Solar Cells Depending on Metal Counter Electrode

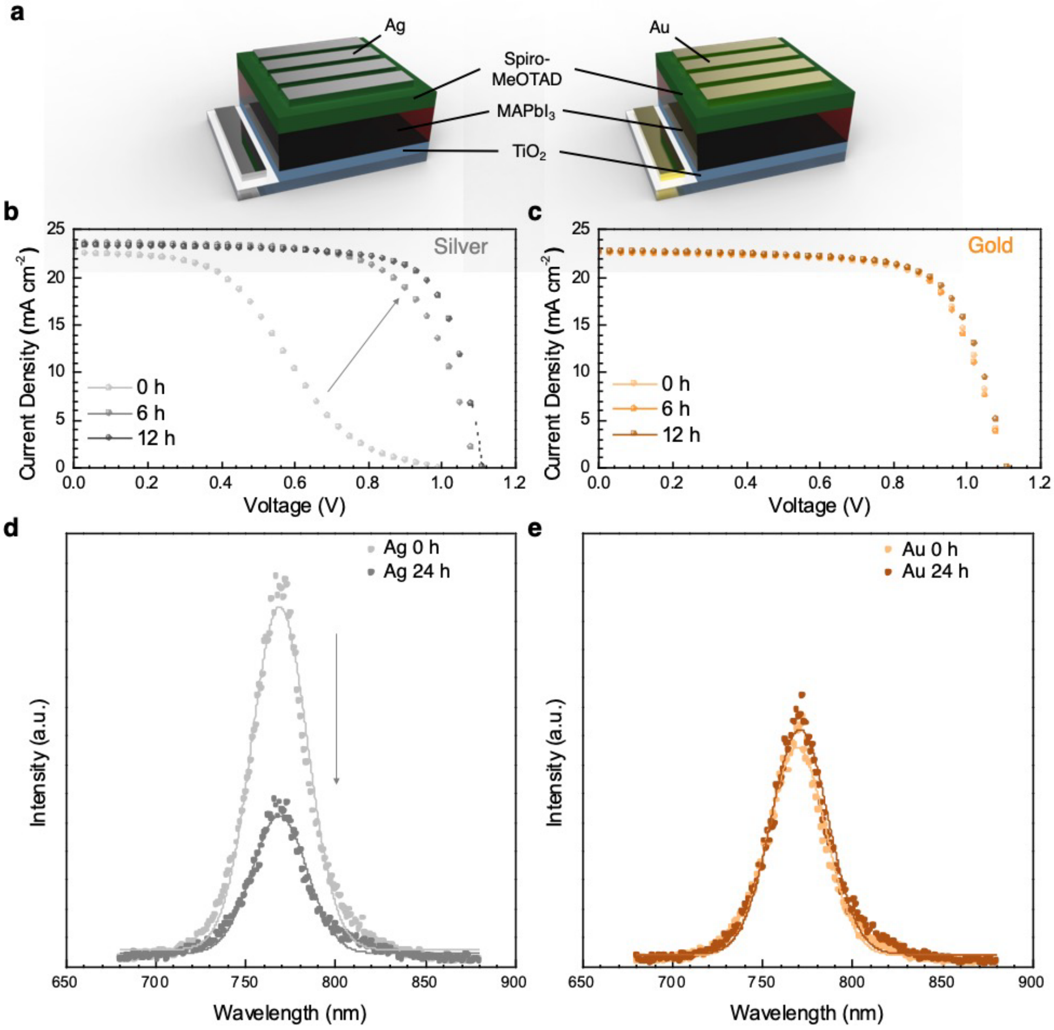

(A) Perovskite solar cell device structure (FTO/TiO$_2$/MAPbI$_3$/Spiro-MeOTAD/Ag or Au) and time evolution plot of JV curves for perovskite solar cells with (B) Ag and (C) Au for their metal counter electrode for different aging time (0, 6, 12 hours). Photoluminescence spectra of fresh (0 hours) and aged (24 hours) glass/perovskite/Spiro-MeOTAD/metal electrode structured device using (D) Ag and (E) Au metal electrodes.

Source: University of California, San Diego

The project team elucidated the fundamentals of the temporary performance instability of the PSCs with Ag electrodes described. Furthermore, the long-term stability of the recovered devices was tested in an argon atmosphere under 1-sun intensity illumination (white LED) to identify their long-term chemical stability, as shown in Figure 15.

Figure 15: Stability Testing of Devices With Ag Versus Au Contacts

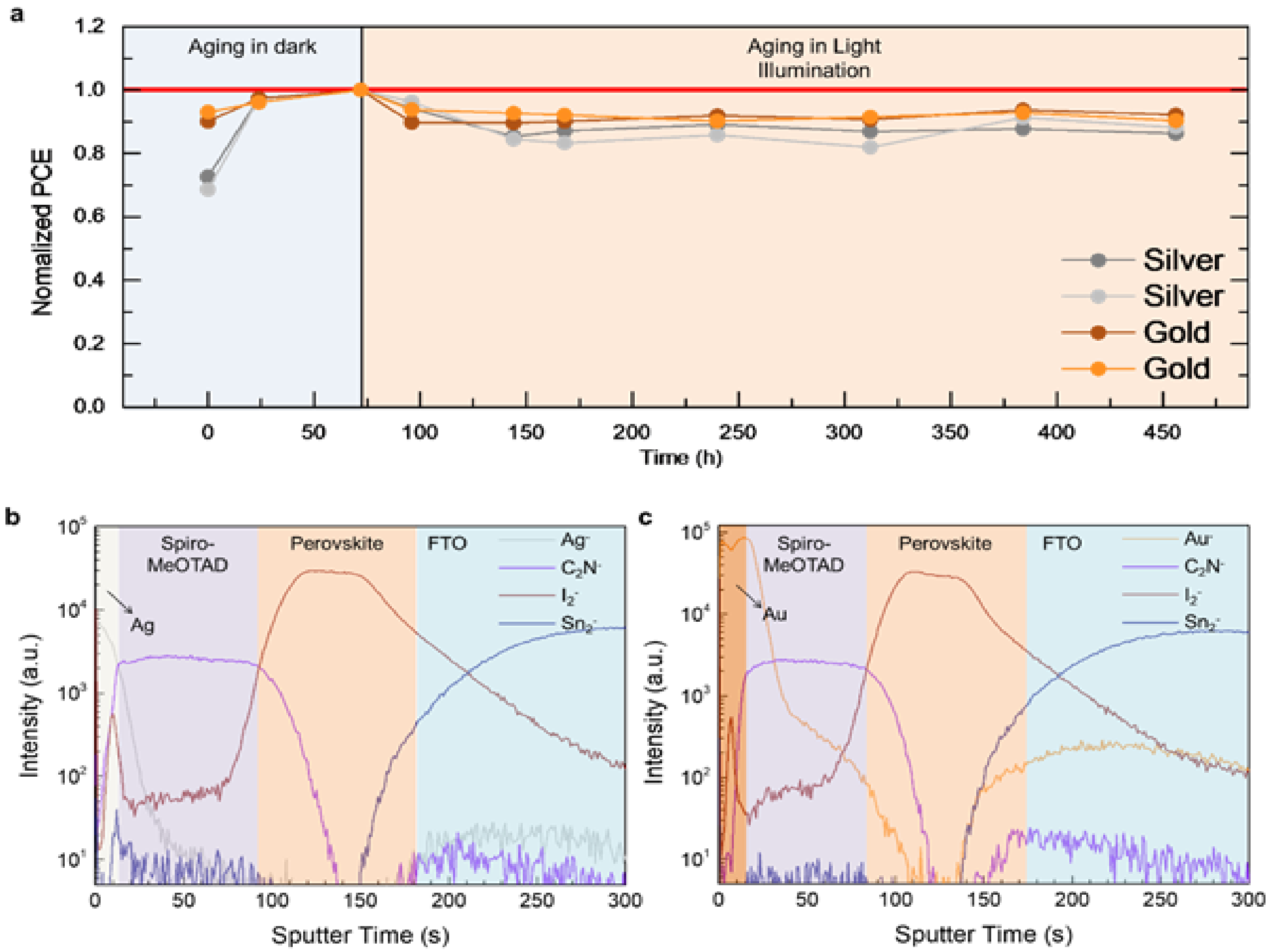

(A) Long-term stability test of Ag and Au metal electrode devices in argon atmosphere under 1-sun intensity illumination. ToF-SIMS depth profiles of (B) Ag and (C) Au electrode devices after long-term stability test.

Source: University of California, San Diego

Surprisingly, PSCs with Ag electrodes did not show a significant difference in long-term stability compared to PSCs with Au electrodes. Both devices maintained 85 to 90 percent of their initial performance for more than 350 hours under continuous light illumination. The project team also investigated the material transfer or ion migration of both devices using ToF-SIMS after a long-term stability test. There is no difference in iodide ion migration between the pristine and recovered devices regarding the illumination at both electrodes. According to the results, it can be concluded that Ag, which is much cheaper than Au, is able to be applied in the commercialized PSCs to substitute for Au electrodes. This work was published with the title of "Effect of Metal Electrodes on Aging-induced Performance Recovery in Perovskite Solar Cells" in *ACS Applied Materials and Interfaces*.

CHAPTER 4: Large-Area Graphene Barrier Layer Synthesis and Characterization

This chapter highlights the project team's results toward leveraging the unique properties of graphene as an encapsulant for perovskite solar materials. Both oxygen and water vapor are known to significantly degrade perovskite solar materials, including the absorber layer itself. As a result, the commercial deployment of PSCs will require implementation of an effective barrier.

Background, Motivation, and Methods for Growth

The air-instability of PSCs remains a major challenge toward their commercialization and deployment on a gigawatt scale. While the record efficiency of PSCs continues to rise (Green, M. et al., 2021), their sensitivity to ambient oxygen and moisture necessitates an encapsulation scheme in order to ensure viable long-term stability. Despite numerous reports of encapsulated devices, long-lasting PSCs often have a low PCE compared to record devices, which themselves often lack stability (Uddin, A. et. al., 2019). This discrepancy can be attributed at least in part to the annealing required to activate most high-quality edge-seal materials, which can destabilize the temperature-sensitive perovskite and/or the HTL within high-efficiency devices (Wang, P. et. al., 2019). Encapsulation of PSCs is critical for preventing the ingress of oxygen and moisture, both of which are known to degrade films and reduce performance (Song, Z. et. al., 2016; Aranda, C. et. al., 2019; Aristidou, N. et. al., 2015; Senocrate, A. et al., 2018).

Due to its impermeability to many small gaseous species, graphene has been widely investigated as a material for thin-film, flexible encapsulation. Numerous papers speculated a significant enhancement to the stability of PSCs when encapsulated with graphene (Zihong, H. et al., 2017). Graphene derivatives, including fluorine-doped nano platelets (Kim, G. et al., 2017) and graphene oxides (Li, H. et al., 2017; Yang, Q. et al., 2017), have also been shown to increase the stability of PSCs. Due to its optical transparency and electrical conductivity, various studies have also incorporated graphene into PSCs as an electrode material (Kim, J. et. al., 2019; Zhu, M., et al., 2019), either in tandem with or separate from barrier applications. Unfortunately, the presence of grain boundaries and defects within chemical vapor deposited (CVD) graphene suggests that a monolayer of graphene would provide numerous pathways to permeation for species such as water and oxygen, which are known to degrade perovskite films. Thus, improved PSC stability due to graphene encapsulation may not always be due to the graphene itself, but rather the polymeric support layer on which the graphene is adhered.

Stacking multiple layers of graphene has been shown to reduce permeation pathways due to grain boundaries being blocked by adjoining layers (Kim, H. et al., 2013), with a detriment to solar cell performance from increased optical losses with every subsequent layer of graphene added. In this study, the project team robustly analyzed graphene barrier films of various numbers of layers, as well as the control polymeric support material (Parylene-C, hereafter referred to as Parylene), prepared as shown in APPENDIX A. Using a low-temperature-activating polyisobutylene (PIB) edge seal resulted in a high-quality seal without causing film degradation and ensured that any small species ingress is through the barrier film being investigated (Cheacharoen, R. et al., 2018; Cheacharoen, R. et al., 2018), rather than through the edge seal. The project team studied barriers composed of up to three layers of graphene, beyond which the optical losses (and fabrication expense) would be impractical for industrial application.

Multilayer Graphene Experimental Results

Samples were placed in a humidity chamber at 65°C and 85 percent relative humidity (ISOS-D-3 testing protocol) (Khenkin, M. et al., 2020). One set of unencapsulated samples was also left in ambient conditions for comparison. Films were removed from the humidity chamber at regular intervals and analyzed via PL measurements and UV-visible (UV-vis) spectroscopy. PL measurements were taken using a Renishaw Raman/microPL microscope with a 633 nm excitation laser, 600 mm grating, 0.15 s dwell time, 0.1 percent power, and 8 μm spot size. A locator cross mark on the slide was used for finding the same location each time. UV-vis measurements were taken on a Perkin Elmer LAMBDA 1050+ UV/Vis/NIR spectrophotometer. At the end of the aging test, the encapsulation was removed from films to enable analysis via scanning electron microscopy (SEM) and x-ray diffraction (XRD). SEM images were taken using FEI Apreo SEM at 10 kV and 0.10 nA. XRD measurements were taken using a Rigaku SmartLab diffractometer. Pictures of the films before and after aging for 200 hours are shown in Figure 16.

Figure 16: Before/After Photographs of Multi-layer Graphene Test

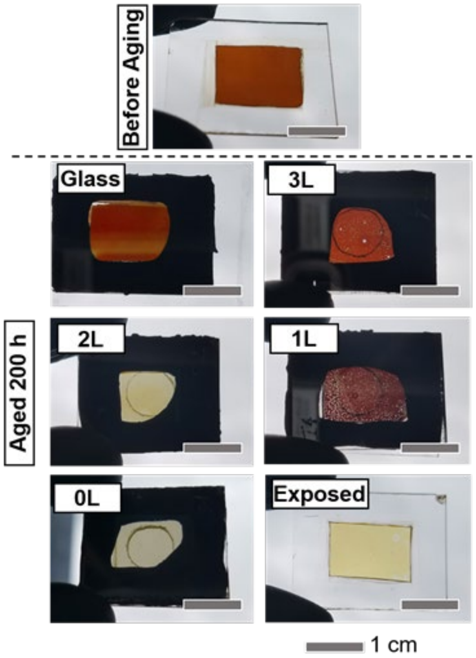

After a damp heat test, the glass-glass encapsulated film has no visible changes while the rest of the films show obvious degradation. The degradation rate is slowed with the incorporation of graphene.

Source: University of California, San Diego

To complement the information gained from tracking optical absorbance, the project team also monitored the films' photoluminescence behavior over time, which can give insight into the films' optoelectronic properties. These results are shown in Figure 17. To improve readability, the normalized PL evolution and peak wavelength evolution have each been split into two panels, with the same data from the 1L-graphene sample represented in both panels. The exposed samples (shown in Figure 17a) quickly decay, and by 100 hours exhibit no PL under laser excitation. In sharp contrast, the graphene/parylene films exhibit an increase in PL over time, despite their yellowing in color and increase in optical transparency. In early trials, the project team considered that this phenomenon could be due to condensation forming on the graphene/parylene barrier, potentially amplifying the PL emissions back to the detector. Thus, in later trials the project team carefully dried the exposed barrier films with an air gun prior to every PL measurement, and this phenomenon persisted. This behavior was not observed in the glass films (Figure 17b) which, much like their optical properties shown in Figure 17c, remained unchanged throughout aging. The graphene/parylene-encapsulated samples also exhibited a shift in the peak wavelength of PL emissions (Figure 17c), a behavior also not present in the glass films (Figure 17d). Thus, despite similar optical properties during aging between the exposed and graphene/parylene-encapsulated samples, results from PL indicated that the decay mechanisms within the respective perovskite films differed substantially.

Figure 17: Photoluminescence Evolution During Multi-Layer Graphene Test

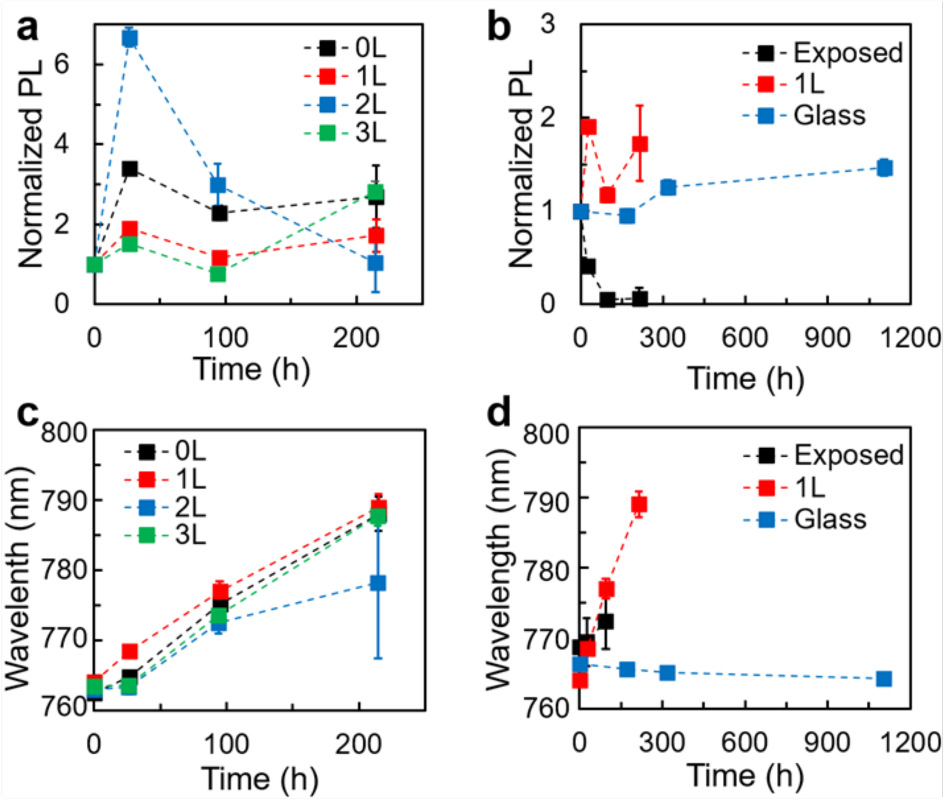

(A) Normalized average PL evolution for 0, 1, 2 and 3L-graphene. (B) PL evolution comparing 3L-graphene to glass and control samples. (C) Peak PL wavelength evolution for 0, 1, 2 and 3L-graphene. (D) Evolution of peak PL wavelength comparing 1L-graphene to glass and exposed samples.

Source: University of California, San Diego

Summary of Graphene as a Barrier Layer

Experimental results show that single-layer graphene can indeed confer improved barrier performance to a polymeric support film, with multi-layer graphene yielding further improved barrier performance. The project team noted that 2-layer graphene exhibited worse performance than 1-layer graphene due to defects introduced during film preparation. Nevertheless, all the project team's graphene/parylene-encapsulated films showed substantial degradation compared to glass-encapsulated films, suggesting that for rigid, non-flexible, long-lasting applications, the addition of graphene to a semi-permeable flexible polymer barrier is insufficient for generating a highly stable device. While modifications to the preparation procedure of the multi-layer graphene could result in improved barrier performance, the numerous grain boundaries in CVD graphene still result in a bulk material that is far from attaining the "impermeable" status of glass or molecular graphene, and the cost and optical losses associated with CVD graphene may limit its utility in commercial applications.

CHAPTER 5:
Solar-Cell Fabrication and Characterization

This chapter outlines and summarizes the development of the PSCs. The overarching goal was to develop high efficiency and stable perovskite solar cells. The project team fabricated solar cells with several state-of-the-art architectures and compositions of the PSC absorber and analyzed both their efficiency and degradation over time.

Laboratory-Scale Process Description and Efficiency Results

Double Cation Process

The FAMA double cation perovskite chemistry mixes cations to improve stability (Pellet, N., et al., 2014). This section discusses the process, device architecture, efficiency, and reproducibility of fabricated PSCs using this chemistry.

The FAMA double cation can be fabricated with a spin-coating process. “All-in-one” or two-step coating processes are commonly used. However, high-efficiency PSCs are mostly fabricated with a two-step spin-coating process (Jiang, Q. et al., 2017). In this project, a two-step coating process was found to achieve the highest efficiency, using a sequential deposition of PbI_2 precursor followed by coating with an organic halide solution in isopropyl alcohol (IPA).

Figure 18 provides micrograph images of the fabricated FAMA perovskite films. Double cation perovskite films fabricated by a 2-step spin-coating process can be deposited onto either the electron transport later (ETL) or the HTL, which means the device can be fabricated as either n-i-p (ETL, then perovskite, then HTL) or p-i-n (HTL, then perovskite, then ETL) structure (Jiang, Q., et al., 2017; Kim, M., et al, 2019). As can be seen in Figure 18, an n-i-p structure was used to fabricate PSCs, using SnO_2 as a bottom ETL and Spiro-OMeTAD as a top HTL. The film thickness of perovskite layer deposited by the 2-step spin-coating process was 800-900 nm, as confirmed with SEM images. The thick film with the lower bandgap of the double cation composition resulted in a higher current density for the PSCs.

Figure 18: Double Cation Perovskite Absorbers and Device Structure

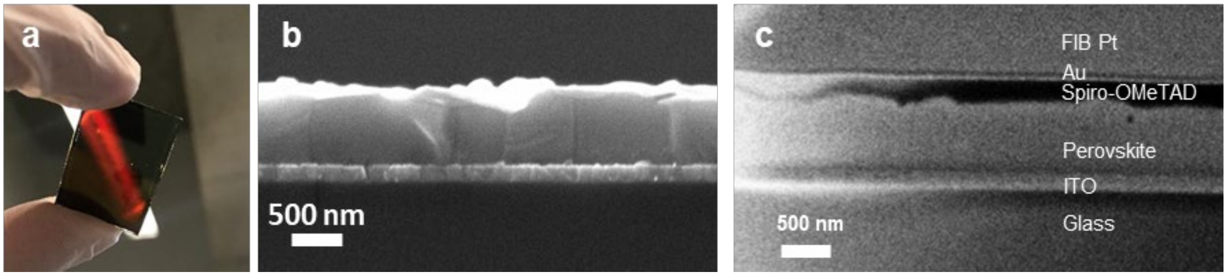

(A) Photo and (B) SEM image of deposited FAMA perovskite film. (C) Transmission electron microscopy (TEM) image for the full device, using FAMA perovskite chemistry.

Source: University of California, San Diego

Efficiency, Reproducibility, and Moisture Effects on Performance

PSCs fabricated with FAMA double cation chemistry exhibit more than 20 percent PCE (Figure 19). PV parameters for the best performing device are 23.99 mA/cm^2 short circuit current density (Jsc), 1.06 V of Voc, and 80.64 percent fill factor (FF), showing higher J_{sc} than $MAPbI_3$ (22-23 mA/cm^2) due to thicker film and wider absorbing wavelength. This FAMA chemistry also provided lessened hysteresis behavior depending on the voltage sweep direction (reverse scan: from V_{oc} to J_{sc}, forward scan: from J_{sc} to V_{oc}) as shown in Figure 19b. The difference between reverse scan and forward scan only showed 0.4 percent of PCE, indicating a nearly hysteresis-less device.

Figure 19: Double Cation Perovskite Solar-Cell Performance

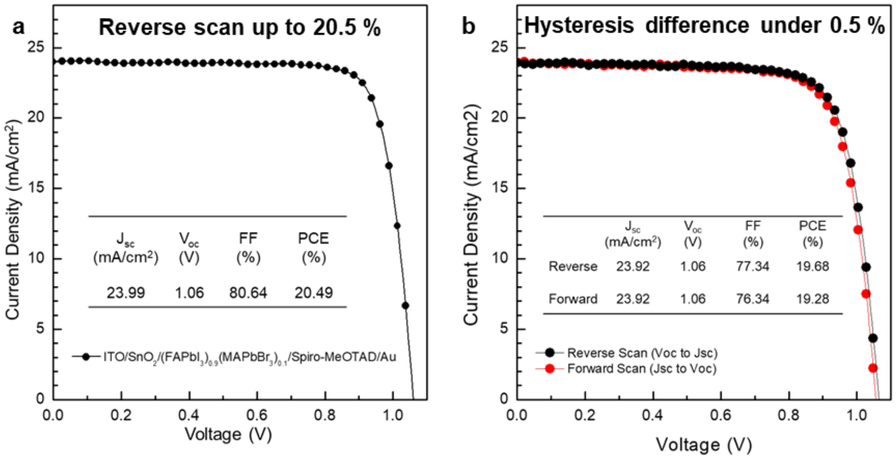

J_{sc} (mA/cm^2)	V_{oc} (V)	FF (%)	PCE (%)
23.99	1.06	80.64	20.49

	J_{sc} (mA/cm^2)	V_{oc} (V)	FF (%)	PCE (%)
Reverse	23.92	1.06	77.34	19.68
Forward	23.92	1.06	76.34	19.28

(A)Current density – voltage curve and photovoltaic parameters for the optimized FAMA perovskite solar cell. (B) Current density – voltage curves and photovoltaic parameters of reverse scan (V_{oc} to J_{sc}) and forward scan (J_{sc} to V_{oc}) for FAMA perovskite solar cell.

Source: University of California, San Diego

The project team also found that the reproducibility of FAMA double-cation perovskite film deposited from a 2-step spin-coating process was excellent. Figure 20 shows the box charts of each PV parameters (J_{sc}, V_{oc}, FF, and PCE) for 25 devices of FAMA PCSs; the average PCE was more than 19 percent (19.04 percent).

Figure 20: Box Charts of Photovoltaic Parameters for the 25 Different Devices of FAMA Perovskite Solar Cells

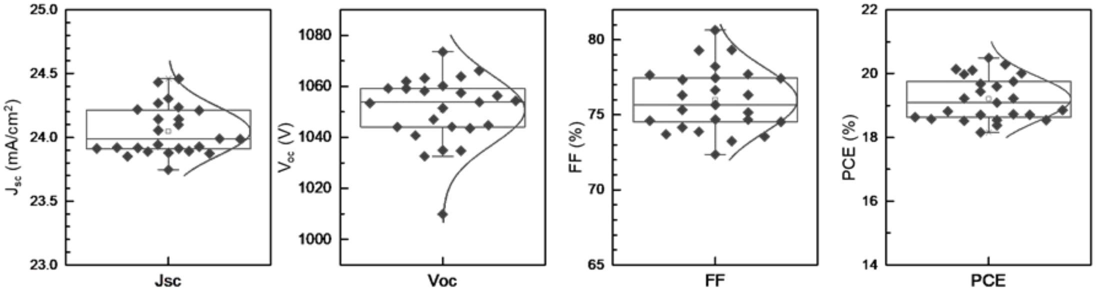

Typical batch statistics for FAMA perovskite solar cell performance parameters

Source: University of California, San Diego

Interestingly, FAMA PSCs exhibited great performance only if the films were annealed with the existence of moisture (outside the glovebox). They showed very poor PV performance (11-14 percent PCE) when the films were annealed without the moisture (inside the glovebox, nitrogen filled, 0 ppm of moisture). The project team expect the MACl in the organic halide solution played a critical role in altering the crystallization during the annealing condition. MACl is not directly incorporated to the perovskite structure but helps the formation and preservation of the black perovskite phase and is finally evaporated during the annealing process (Kim, M. et al., 2019). It was verified from this result that the evaporation of MACl needed the existence of moisture or oxygen to take place.

Characterization of Degradation Over Time and Recovery

As a strategy for enhancing the stability of PSCs, it was important to properly characterize the degradation of FAMA PSCs. There are several well-known factors that influence the degradation of PSCs: oxygen, moisture, charge carrier (light illumination), and electric field (photovoltage, bias-induced) (Kim, D., et al., 2019; Bryant, D., et al., 2019; Artistidou, N., et al., 2017; Song, Z., et al., 2016). As shown in Figure 21, after 16 hours of continuous light illumination with ambient nitrogen, the PSC degraded from 18.7 percent initial PCE to 14.3 percent PCE. While J_{sc} remains same (23.6 mA/cm^2 to 23.5 mA/cm^2), decreased FF and V_{oc} were mainly attributed the performance degradation after the light soaking.

The project team found that the degraded devices self-recover upon storing the devices in the dark for 16 hours. The degraded devices recovered to the initial PCE (18.8 percent) after undergoing the dark recovery process (Figure 21c). However, the recovery of the performance is mainly due to the FF increase and the V_{oc} cannot be recovered to the initial V_{oc} (Figure 21b, initial: 1.04 V, recovered: 0.98 V). This result indicated a light-induced (or bias-induced) defect generation inside the perovskite layer. In situ observation for the crystallographic information of perovskite materials under light illumination or under the electrical bias may provide more detailed information in the future.

Figure 21: Current – Voltage Curves and Voc, PCE Plots for Perovskite Solar Cells

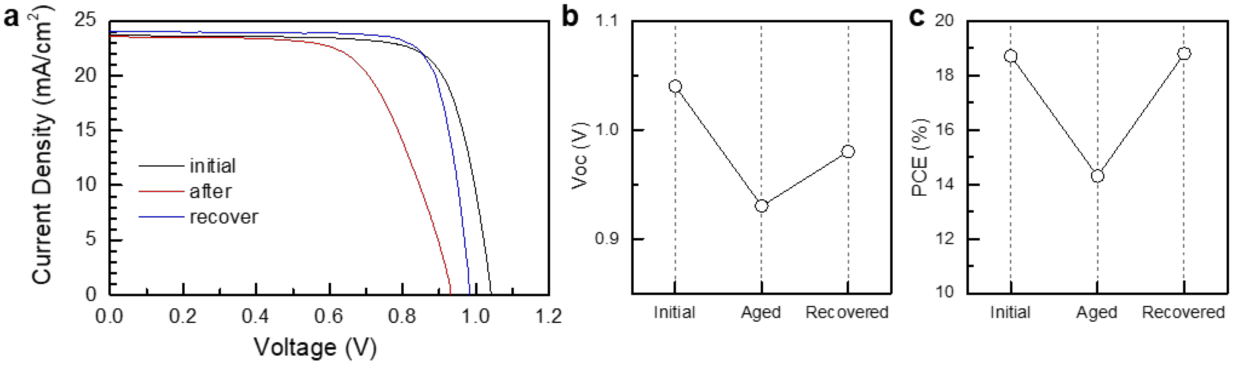

(a) Current – voltage curves. (b) open circuit voltage. (c) PCE plots for PSCs (initial, after light-induced degradation, after recovery at dark)

Source: University of California, San Diego

Thermal Effect on the Recovery of Perovskite Solar Cells

Since the project team found that continuous light illumination was detrimental to the FAMA PSCs, and also that they can be recovered through resting in the dark, the team needed to find methods for rapid recovery. The light-induced and bias-induced degradation were the result of ion migration, especially halide ion migration. During the dark recovery following an electrically biased test, ions may move back to the initial location by diffusion and heal the defect sites or recrystallize the perovskite. In that manner, the project team expected that activating the ion redistribution by external stimuli such as thermal energy or applying a reverse electric bias may help to promote the recovery process.

As shown in Figure 22, the project team found that keeping the degraded device at a higher temperature in the dark 122°F (50^{o}C) helped promote faster recovery. While keeping a device at room temperature in the dark did not recover its initial PCE after two hours, the device kept at the higher temperature in the dark recovered to the initial PCE within two hours. This result confirmed that the light-induced degradation is mainly caused by ion migration and can be resolved by rapid ion redistribution.

Figure 22: Thermal Effect on the Recovery of FAMA Perovskite Solar Cells After Light-Induced Degradation

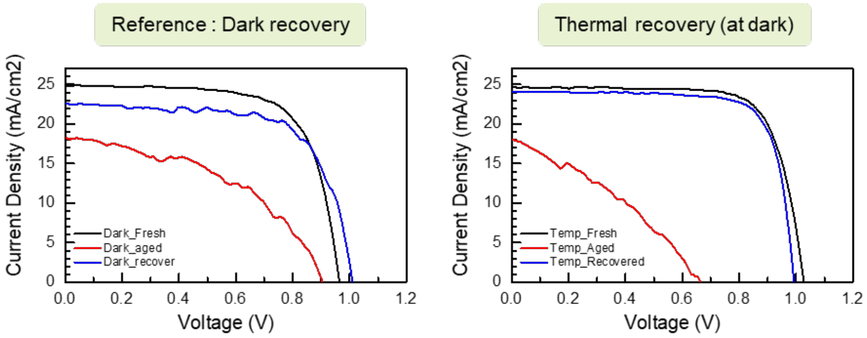

		Jsc (mA/cm2)	Voc (V)	FF (%)	PCE (%)
Fresh	Dark	24.84	0.96	70.02	16.77
	Thermal	24.60	1.03	75.22	19.01
Aged	Dark	18.22	0.90	46.54	7.66
	Thermal	18.05	0.66	34.06	4.07
Recovered	Dark	22.48	1.01	68.44	15.55
	Thermal	24.06	0.99	77.51	18.52

Current density-voltage curves show recovery in the dark and accelerated recovery with mild heating. Device parameters are detailed in the table.

Source: University of California, San Diego

Triple-Cation Solar Cell Development

Composition engineering has been shown to be an effective approach to improve absorber stability (Eperon, G., et al., 2014; Saliba, M. et al., 2016); PSCs appear to have better stability and longer operational lifetimes as composition complexity increases. The FAMA composition was one of the early-developed systems to yield high-performing PSCs. Recently, cesium (Cs) has been used as the A-site cation to explore more complex compositions, such as in CsMA, CsFA and CsFAMA (Lee, J. et al., 2015; Yi, C. et al., 2016; Saliba, M. et al., 2016).

Incorporating a small fraction of CsI in the perovskite precursor solution has been widely adopted to fabricate Cs-containing A-site PSCs with repeatability, stability, and performance (Bai, S. et. al, 2019; Xu, J. et. al, 2020). In this subtask, the project team aimed to understand the mechanisms that form the basis for improved electronic properties, performance, and stability upon the additions of alkali metals, such as Cs and/or Rb, in PSCs (Correa-Baena, J., et al., 2019).

See Figure 23 for representative current density-voltage curves, including the backward and forward scans, for PSCs with FAMA baseline composition ($(FAPbI_3)_{0.87}(MAPbBr_3)_{0.13}$) and 5 percent RbI and 5 percent CsI addition, denoted as RbCsFAMA. The champion device for FAMA PSCs yielded an open-circuit voltage (V_{OC}) of 1.09 V, short-circuit current density (J_{SC}) of 22.8 mA/cm2, fill factor (FF) of 51 percent, and PCE of 12.6 percent under AM1.5 illumination. In contrast, the champion device prepared with RbCs yielded V_{OC} = 1.10 V, J_{SC} = 22.7 mA/cm^2, FF = 76 percent, and PCE = 19 percent.

Figure 23: Perovskite Device Architecture and Performance

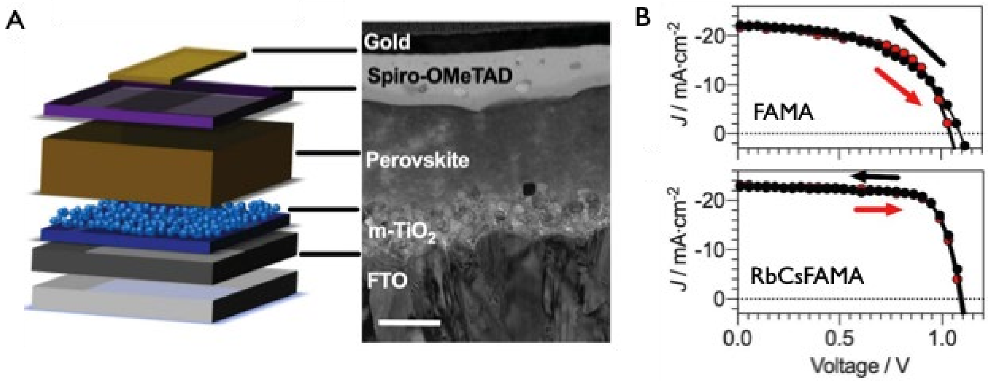

(A) Schematic of PSCs fabricated and studied along with a cross-sectional transmission electron microscopy (TEM) image. Scale bar is 200 nm. (B) Perovskite solar cell current-voltage characteristic for FAMA and RbCsFAMA perovskite absorbers

Source: University of California, San Diego

Anisole Anti-Solvent for a Wider Process Window

The project team also introduced methoxybenzene (anisole) as an alternative anti-solvent in place of chlorobenzene (CB), to widen the processing window for the 1-step anti-solvent dripping fabrication method (Yavari, M., et al., 2018; Zhao, P., et al., 2018). Anisole has a higher boiling point and viscosity, and the intermolecular interaction between anisole and the perovskite precursor solvent (DMF/DMSO) is larger than with CB, so therefore can have a wider processing window and large-area spin-coating compatibility. Plus, anisole is less toxic than CB or toluene, which allows anisole to be a more viable solvent for commercialization.

Efficiency and Reproducibility

The best-performing triple cation PSCs using anisole as an anti-solvent showed PCE of 19.58 percent with J_{sc} of 23.90 mA/cm^2, V_{oc} of 1.09 V, and FF of 75.18 percent in reverse scan, as shown in Figure 24. Devices showed almost no hysteresis behavior depending on the voltage sweeping direction. Forward scan performance was PCE of 19.49 percent, which is less than

0.1 percent different from the reverse scan. Using anisole in a 1-step method, the reproducibility of the devices was more uniform than the 2-step method in the previous chapter. Twenty-nine devices using this method showed PCE of 18.89 percent, with the standard deviation of 0.38 (as shown in the box charts in Figure 24b).

Figure 24: Triple-Cation Device Performance and Excellent Repeatability

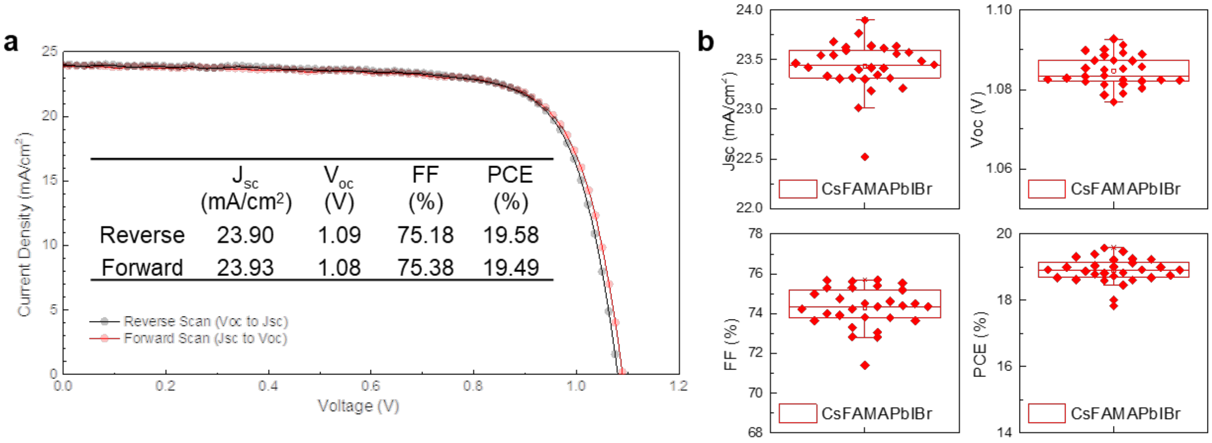

	J_{sc} (mA/cm^2)	V_{oc} (V)	FF (%)	PCE (%)
Reverse	23.90	1.09	75.18	19.58
Forward	23.93	1.08	75.38	19.49

(A) Current – voltage curves for the triple cation perovskite solar cells with reverse and forward voltage scan. (B) Box charts for photovoltaic parameters of the triple cation perovskite solar cells

Source: University of California, San Diego

Methylammonium-Free Perovskites: Issues with Phase Segregation Under Operation

The instability of perovskite absorbers under various environmental stressors is the greatest hindrance to its potential PV deployment. Although the mixed A-site MA-free PSCs have demonstrated high efficiency with enhanced thermal and operational stability, investigation of remaining degradation mechanisms in MA-free and triiodide devices upon aging under operational conditions is needed. Microscopic evaluation of the device performance loss may help elucidate reaction and degradation mechanisms. In this subtask, the project team monitored performance of high-performing MA-free ($FA_{0.9}Cs_{0.1}PbI_3$) PSCs with more than 600 hours of various environmental stressors intrinsic to PV operation (Li, N., et al., 2020).

In devices with simpler compositions without acidic methylammonium cations that achieved 20 percent PCE, the project team monitored device performance under four distinct conditions: 185°F (85˚C) heating in the dark, 1-sun illumination at near room temperature at open circuit conditions, and stabilized power output at the maximum power point at near room temperature. Device degradation appeared to worsen with increased carrier concentration. Reference devices showed almost no loss in efficiency (~1 percent) after 600 hours. These data suggest that the methylammonium-free pure iodide perovskite has good thermal stability but is unstable over long periods in illuminated conditions. Developing processes that maintain uniform but complex alloy compositions over large areas appears to be a necessity.

Device Fabrication and Stress Testing Conditions

The PSCs in this project all have a nominal composition of $FA_{0.9}Cs_{0.1}PbI_3$ and are fabricated in the conventional device architecture: ITO/SnO_2/Perovskite/Spiro-OMeTAD-PTAA/Au. The distribution of device performance is shown in Figure 25, where which the average PCE of 19.2 percent and the champion device achieve a PCE of 20.12 percent.

Figure 25: MA-Free Perovskite Solar Cell Device Performance and Repeatability

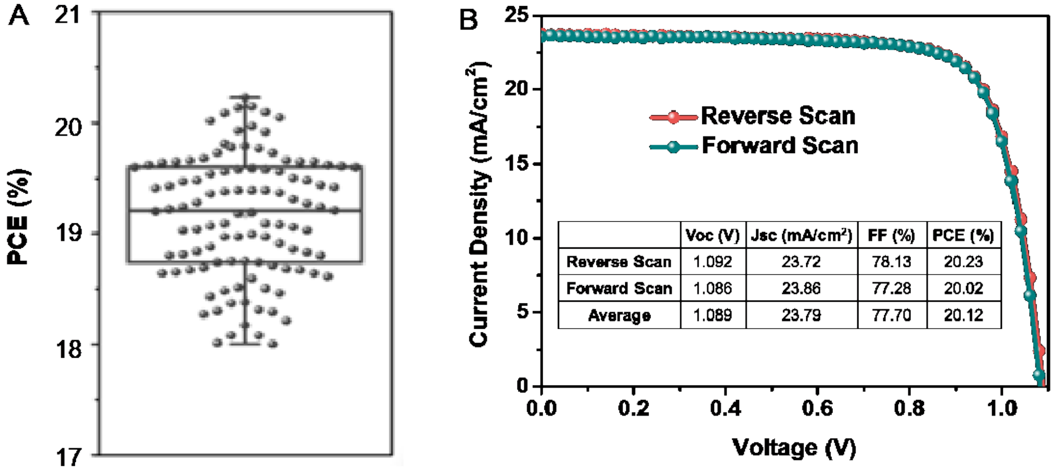

	Voc (V)	Jsc (mA/cm²)	FF (%)	PCE (%)
Reverse Scan	1.092	23.72	78.13	20.23
Forward Scan	1.086	23.86	77.28	20.02
Average	1.089	23.79	77.70	20.12

(A) The distribution of PCE of 109 PSCs with absorber chemistry of $FA_{0.9}Cs_{0.1}PbI_3$. (B) The current density-voltage curves of the champion device out of the batch of devices studied .

Source: University of California, San Diego

To assess PSC instability and underlying failure modes under prolonged testing, the project team monitored the device performance in four distinct conditions: 185°F (85°C) heating in dark (labelled "Heat"); 1-un illumination at near room temperature 95±18°F (35±10°C) at open circuit conditions (labelled "Light"); and stabilized power output at the maximum power point at near room temperature (labelled "SPO"). The reference sample (labelled "Ref") was stored in the dark. All stress conditions were maintained under an N_2 ambient for a total of 600 hours.

Device Degradation Appears to Worsen With Increased Carrier Concentration

The changes in device performance when subjected to stress-testing are shown using JV measurements in Figure 26. JV data indicated that while the reference devices showed nearly no loss in PCE (~1 percent) after 600 hours, the "Heat", "SPO", and "Light" devices all showed significant performance losses in PCE (~18.0, ~47.7, and ~66.3 percent relative loss, respectively). The PSCs showed thermal stability as the Heat samples exhibited the slowest PCE decay with a slight decrease in fill factor (FF). On the other hand, SPO and Light were the stronger stressors that affected device performance considerably, resulting in significant declines in V_{OC}, J_{SC}, and FF, as shown in Figure 26. These JV data suggested that the $FA_{0.9}Cs_{0.1}PbI_3$ absorber had good thermal stability but was unstable over long periods in illuminated conditions.

Figure 26: Device Performance as a Function of Aging Time

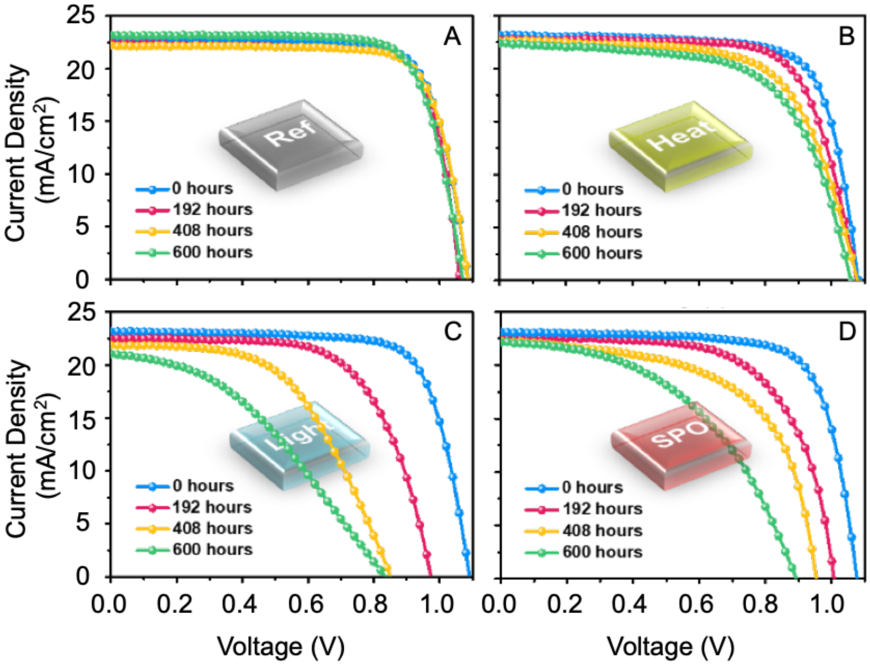

(A-D) are JV curves of samples stored in the dark at near room temperature 95±18˚F (35±10˚C), in elevated temperature at 185°F (85˚C), in 1-sun illumination at near room temperature, and in stabilized power output with applied voltage of 0.9 V, respectively [35]

Source: University of California, San Diego

From X-ray microscopy data detailed in Li et al., 2020, the project team found that either 1-sun illumination or heating at 185°F (85˚C) was enough to form inactive Cs-rich secondary phases, when using $FA_{0.9}Cs_{0.1}PbI_3$ absorber composition. The efficiency correlated inversely with the number density of the Cs-rich clusters found on the microscopic scale, which varies by stress condition. These findings revealed the cation-dependent instability of $FA_{0.9}Cs_{0.1}PbI_3$ perovskites and provided future guidance on composition engineering to improve photostability in alloy perovskites.

Improved Durability With Silicon-Spiro HTL Material

The novel modified spiro-OMeTAD compound studied in this subtask, with the center carbon atom replaced with a silicon (Si) atom (denoted as Si-Spiro), has the potential to improve durability of the PSC. Figure 27 shows the molecular and chemical differences between Spiro-OMeTAD, denoted as Ref-Spiro, and Si-Spiro.

Figure 27: Molecular and Chemical Differences in Modified Spiro-OMeTAD

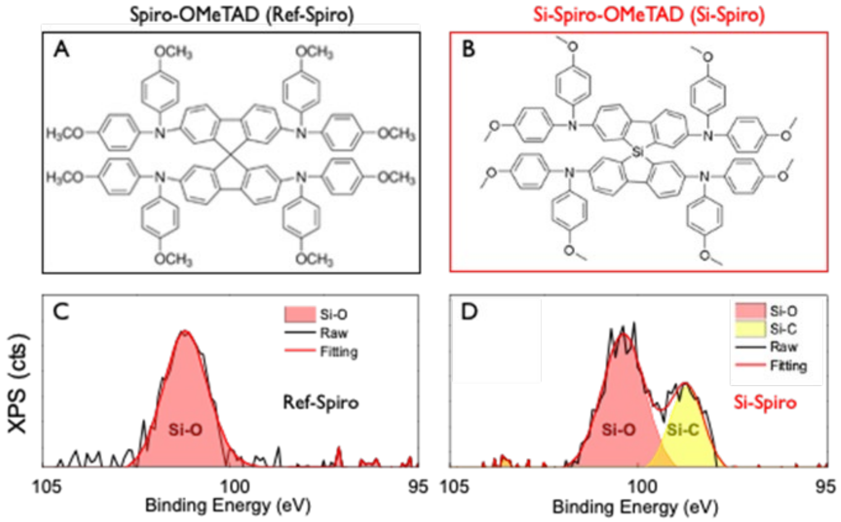

A-B) Chemical structure. C-D) X-ray photoelectron spectroscopy of the pristine and modified spiro-OMeTAD

Source: University of California, San Diego

The estimated energy levels from X-ray photoelectron spectroscopy suggested that Si-Spiro should have similar band structure and alignment as Ref-Spiro, which can be utilized as the potential HTL material. On the other hand, hole mobility in Si-Spiro appeared to be one order of magnitude larger than Ref-Spiro from the space-charge limited current measurement, and therefore very promising for application in PSCs.

The project team observed enhanced device performance and stability when using Si-Spiro as the HTL materials, shown in Figure 28.

Figure 28: Device Performance and Stability Using Ref- and Si- Spiro as HTL Materials

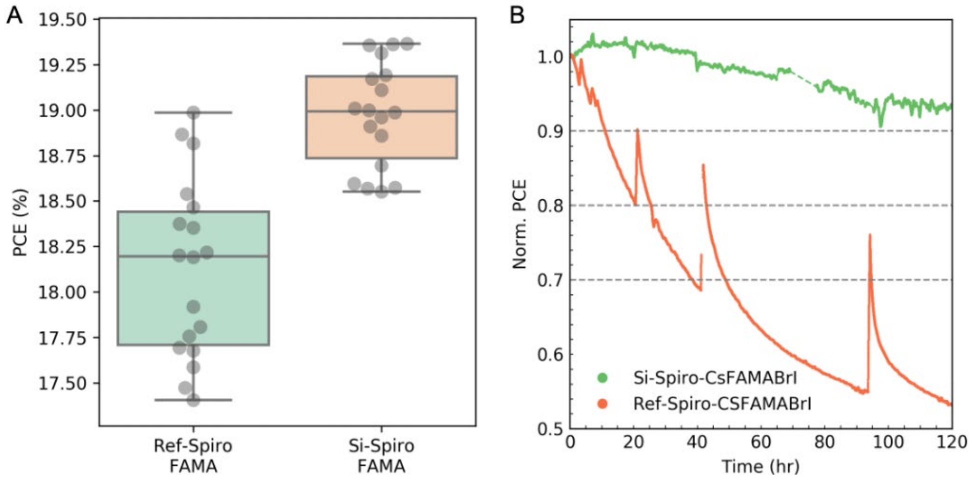

Device performance and stability using Ref- and Si- Spiro as the HTL materials. Comparison of (A) device performance and (B) device stability of PSCs prepared using Ref- and Si- Spiro HTL materials.

Source: University of California, San Diego

CHAPTER 6:
Mini-Module Fabrication and Testing

This chapter outlines and summarizes the results of scale-up techniques for fabricating large-area high-performing perovskite solar modules and testing in challenging outdoor environments and in accelerated laboratory testing.

Fabricating Large-Area Perovskite Cells

There are significant challenges to fabricating large-scale PSCs. The two most critical obstacles are: depositing high-quality large-area perovskite films and designing modules to be robust in the face of the perovskite absorber's environmental sensitivity. The goal of this task was to fabricate large-area PSCs and encapsulate them into small-scale modules for studies of operational durability. Success was achieved in the fabrication of high-quality perovskite absorbers using a blade-coating process. The project team chemically tuned the perovskite and blade-coating process to produce high-performing, stabilized perovskite films with large areas. The project team also developed a blade coating compatible with the anti-solvent-assisted perovskite film fabrication method, depicted in Figure 29.

Figure 29: Schematics for Large-Area Perovskite Film Fabrication Using Anti-Solvent Bath Process-Assisted Blade Coating

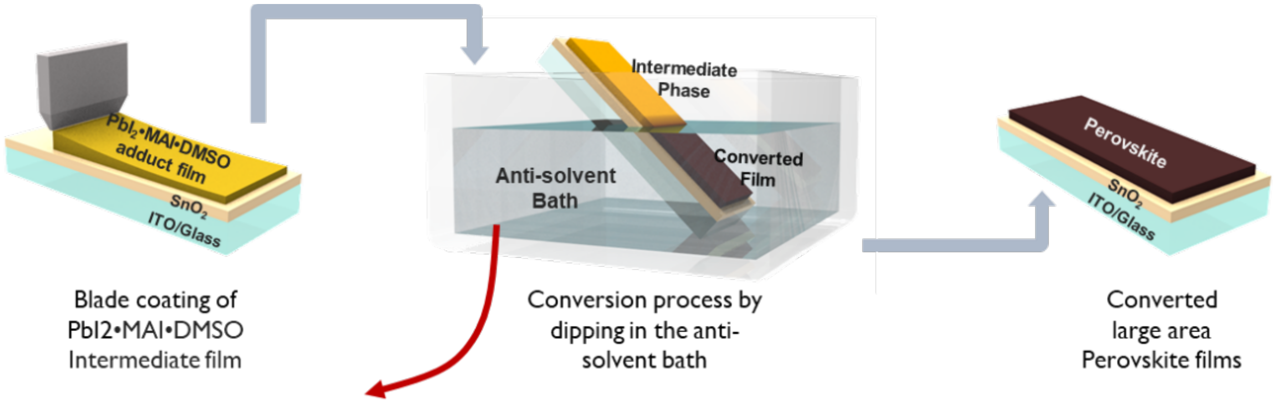

The large-area fabrication process begins with a blade-coating step, followed by a dip in an anti-solvent bath, and finally an annealing step to form the perovskite.

Source: University of California, San Diego

Meniscus coating, a simple and scalable manufacturing technique, includes methods such as dip coating, blade coating, and slot-die coating (Li, Z., et al., 2018). Among these techniques, blade coating is a promising and reproducible method to deposit perovskite films.

To achieve high quality large-area blade-coated perovskite layers, the project team needed to first optimize blade-coating parameters such as blading speed, the gap between the blade and the substrate, and the precursor amount. Depending on blade-coating speed, the method exhibits two completely different behaviors: evaporation and Landau-Levich (Le Berre, M., et al., 2009). Evaporation is dominant at low speeds where the coated film dries as the blade moves. Landau-Levich, on the other hand, is dominant at high speeds, where the wet films form and remain on the substrate due to relatively low drying speeds compared to the coating speed. The two regimes not only determine the thickness of the film (Deng, Y. et al., 2018) but also the film orientation. Under the evaporation regime, the film tends to form highly aligned morphology; under the Landau-Levich regime, large isotropic plate domains are formed (Li, J., et. al., 2017). Therefore, in this report, the project team chose the evaporation regime (slow speed) blade-coating process for better morphology control and faster evaporation of the coated films.

Prior to blade coating, the project team deposited a high-volume manufacturable tin oxide (SnO_x) layer onto large area fluorine-doped tin-oxide (FTO) substrates via thermal evaporation and validated the coverage and electronic properties of the tin oxide layer.

For blade coating, a perovskite solution optimized for the best optoelectronic properties and ink stability was prepared. Using blade coating, the perovskite solution was spread onto the large-area FTO/SnO_x substrate. The perovskite precursor containing PbI_2 and FA or MA halide can be easily coated with blade coating; however, anti-solvent dripping was unable to be performed with the blade coater. Therefore, the project team decided to dip intermediate films coated by the blade coater into the anti-solvent bath to convert the film to perovskite film. A conversion process was used where, after deposition of the PbI_2-MAI-DMSO adduct, exposure to an anti-solvent bath drove away the solvent and nucleated the perovskite.

Like the baseline spin-coating process, an annealing step was followed for both electrochemical and blade coating methods to fully convert the perovskite. Once the perovskite layer was converted, Spiro-MeOTAD and Au were deposited to finish the full device. The large-area cell was then evaluated, using device testing methods.

A large single perovskite device was avoided because the resistance loss in the transparent conducting oxide (TCO) layer is substantial in a large substrate. Therefore, the large cells were divided into small subcells to mitigate the resistance loss. Despite the success on small perovskite devices achieving more than 25 percent PCE, the module efficiency of perovskite remains substantially lower. Figure 30 shows the perovskite solar module design. To make the PSCs into a module, two major interconnection strategies were used: a singulated interconnection and a monolithic interconnection (Reese, M., et al., 2018). The singulated interconnection was literally connecting individual cells by external circuits and is widely used in silicon solar cells. The problem is that the external connection creates a relatively large dead area. The monolithic interconnection, on the other hand, was achieved by depositing large-area films and subsequently scribing through specific layers during the fabrication process. This approach resulted in a relatively small amount of dead area. The perovskite films can be fabricated into uniform and large-area films, which makes monolithic interconnection more suitable. The monolithic module has the same structure as the typical n-i-p perovskite cell (metal/HTL/Perovskite/ETL/TCO), but is divided into subcells, using P1, P2, P3 scribing.

Figure 30: Schematic Illustration of the Monolithic Perovskite Solar Module

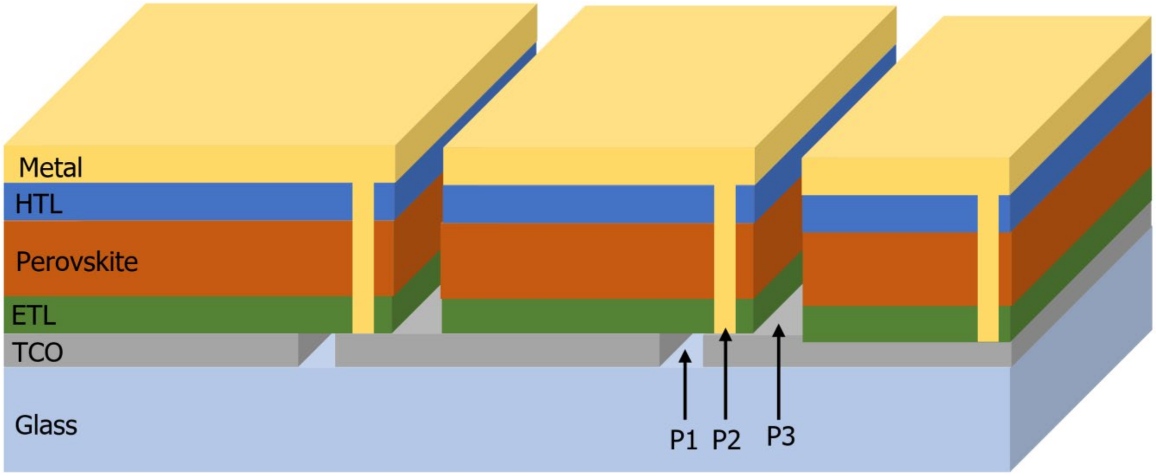

Monolithic integration of perovskite solar cells using laser scribing of P1, P2, P3 lines as indicated by arrows left to right

Source: University of California, San Diego

Full-Area Electron Transport Layer Development and Results

The project team developed a vacuum thermally evaporated SnO_2 electron transport layer (ETL) to produce stable and efficient PSCs. With this technique, the project team readily produced large batches of films with excellent ETL coverage and uniformity on substrates ranging from 1 cm^2 to 100 cm^2. Small-area devices (6.25 cm^2, active area 0.07 cm^2) had comparable device performances for devices that used SnO_2 synthesized from standard spin-casting procedures.

The surface coverage and band-edge of the tin oxide was probed with an in-house electro-chemical apparatus prior to the completion of the perovskite device to ensure the quality of tin oxide deposition (Figure 31). In this cyclic voltammetry (CV) measurement, an aqueous solution of potassium chloride and potassium ferro/ferricyanide was used as an electrolyte, Ag/AgCl was used as a reference electrode, Pt was used as a counter electrode, and SnO_x/FTO was used as a working electrode. Representative scans for different working electrodes are shown in Figure 31b. For the bare FTO (black solid line), sharp current peaks were seen around 0.25 V versus (vs.) Ag/AgCl, which corresponds to the redox reaction between Fe^{2+} and Fe^{3+}. Once tin oxide was deposited onto FTO, this reaction was quenched.

Figure 31: Thermal Evaporation of SnO$_x$ Electron Transport Layers

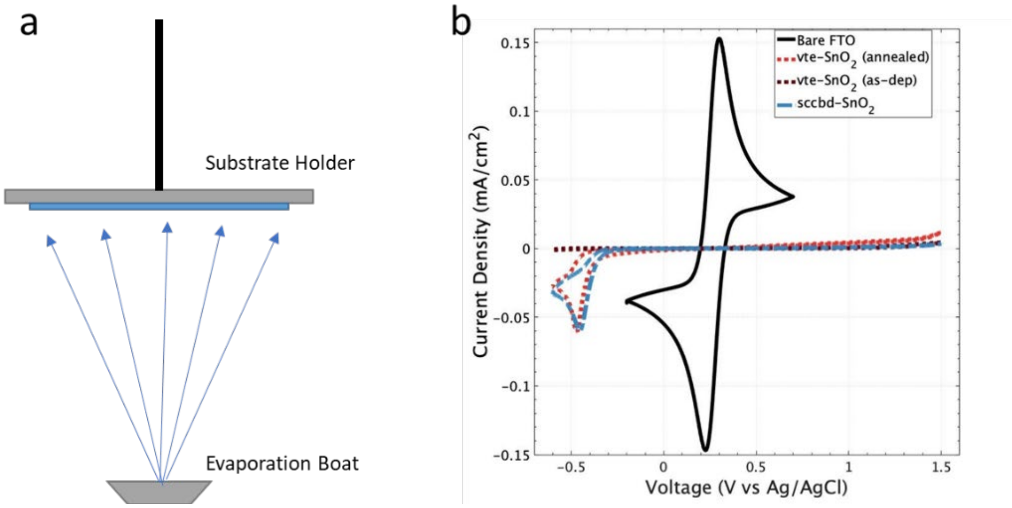

(A) Simple schematic of the evaporation chamber (vacuum pump and quartz crystal monitor not depicted). (B) Representative CV scans of bare FTO (black solid line), evaporated and annealed SnO$_x$ (red dotted line), evaporated SnO$_x$ (black dotted line), and spin-cast SnO$_x$ (blue dotted line).

Source: University of California, San Diego

The cathodic current seen around -0.5 V vs. Ag/AgCl corresponds to the conductive band minimum of the project team's tin oxide. The position of this current onset (and therefore the band edge) was manipulated through annealing (which controls the oxidation state of the material). In general, the project team found that current onsets of -0.5 V vs. Ag/AgCl (or lower) yielded the highest performing devices. If pinholes were present in the tin oxide film, the bare FTO would be exposed, allowing charge transfer in the same energy regime as the tin oxide bandgap. The amount of current leakage can be used to calculate pinhole density (Kavan, L., et al., 2017). Further insight into the correlation between CV and device results is presented in the next section.

Device Results and Reproducibility

Once suitable tin oxide films were fabricated, the rest of the device was completed. For the project team's baseline device, this included the triple cation perovskite and spiro-OMeTAD. Au was used as a back contact for the device.

To date, the evaporation method produces devices with comparable performance to the project team's devices, based on spin-casted tin oxide ETLs (Figure 32). Furthermore, this technique was highly repeatable and could be used to fabricate many films in a single batch (the project team deposited 25 films at a time with plans to approach 100 films per deposition).

Figure 32: Device Performance for Large-Area Thermal Evaporated SnO_x

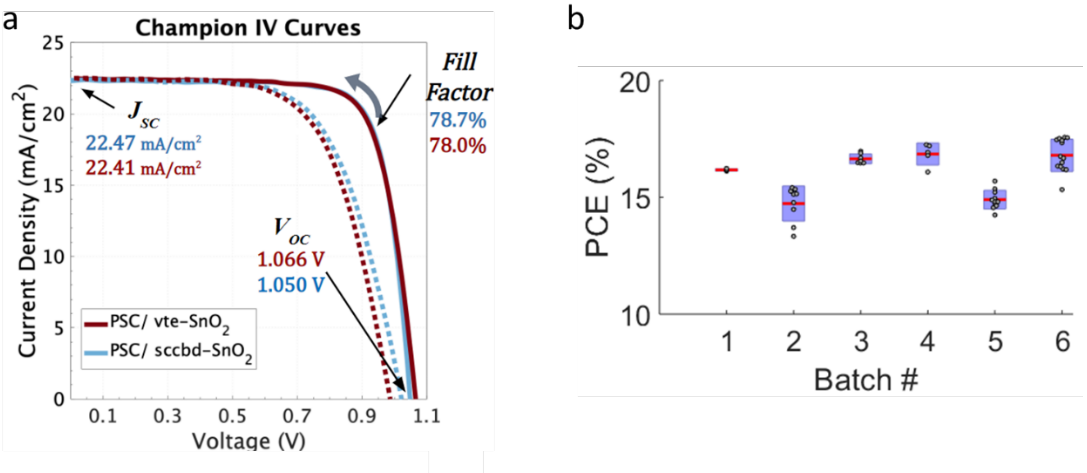

(A) JV characteristic curves from champion devices with evaporated tin oxide (red) and spin-cast tin oxide (blue) ETLs. (B) Several batches of devices (arranged chronologically) highlighting the reproducibility of device results from this technique

Source: University of California, San Diego

Capacity for Large-Area Fabrication

A major appeal for the blade coating evaporation technique, is its ability to deposit on large-area substrates with minimal adaptations from the small-area process. This is necessary for the commercial deployment of PSCs, whether as single-junction devices or as silicon-perovskite tandem cells. Figure 33 shows a proof-of-concept for the viability of thermally evaporated tin oxide as a large-area ETL. From Figure 33b, the project team saw that six large SnO_x/FTO pieces (originally deposited as a single 100 cm^2 tin oxide on FTO film) demonstrated nearly identical CV curves. This demonstrated the uniformity of the film across the entire substrate and promises effective integration into a large-area device assembly.

Figure 33: Large-Area SnO_x Characteristics

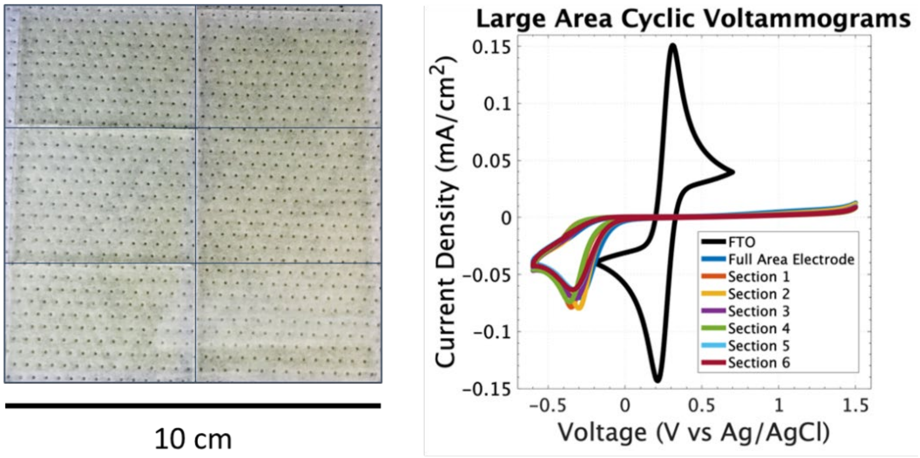

(A) Optical image of the 100 cm^2 SnO_x thermally evaporated onto FTO conductive glass and broken into six pieces for testing. (B) CV results from the different tin oxide pieces showing they are nearly identical and that the overall film would be suitable for a large-area PSCs

Source: University of California, San Diego

Blade Coated Layers and Device Results

Prior to the conversion process by dipping in the anti-solvent bath, the project team needed to ensure the uniform coating of the intermediate film. As seen in Figure 34, perovskite precursor solution was unable to be coated uniformly on the substrate without the guidance rail, because the gap between substrate and actuator was critical for uniform coating. After making the guidance rail to maintain the gap distance, the precursor could be coated uniformly, which enabled the project team to have viable films for conversion in an anti-solvent bath.

Figure 34: Optimization of the Blade-Coater

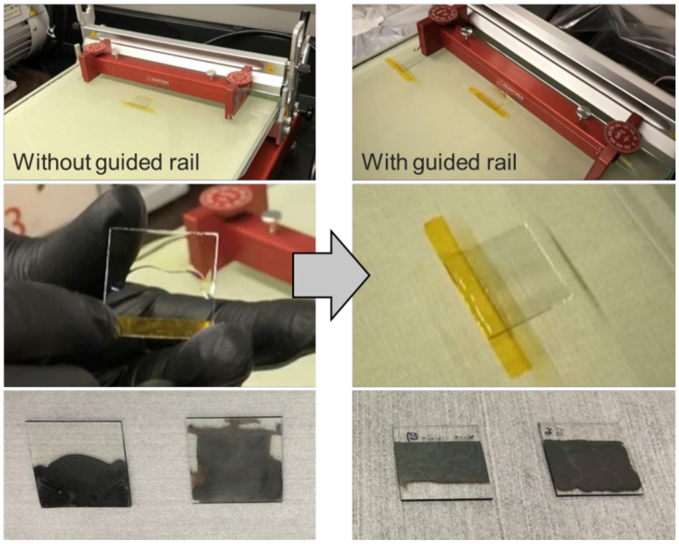

Images of blade coater and blade coated perovskite films without guided rail (left) and with guided rail (right)

Source: University of California, San Diego

Small Area

The project team compared morphology and optoelectronic properties between spin-coated and blade-coated cells fabricated on 2.5 x 2.5 cm^2 substrates to evaluate the film quality made by blade coating. In Figure 35, the blade-coated and spin-coated film have similar grain sizes; however, blade-coated films have relatively rough surfaces compared to spin-coated films. From the cross-sectional SEM image, the blade-coated layer also has irregular voids.

Figure 35: SEM Images of Spin-Coated and Blade-Coated Films

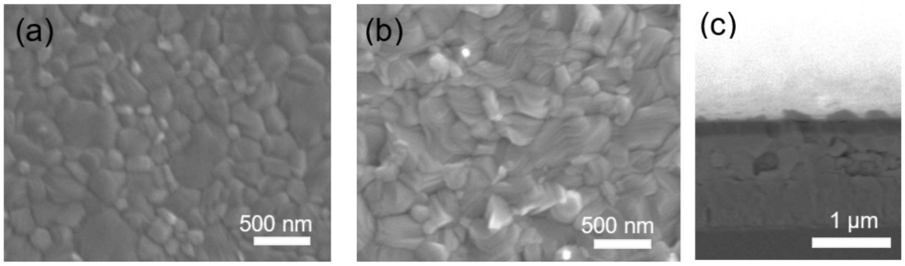

SEM images of (A) spin-coated $MAPbI_3$; (B) blade-coated $MAPbI_3$; (C) cross-section of blade-coated perovskite device

Source: University of California, San Diego

UV-vis absorption spectroscopy was also performed. The overall absorption intensity around 400 - 750 nm is lower in blade-coated samples though the onset of the absorbance is nearly identical. With the UV-vis data, a Tauc plot was plotted and confirmed that optical bandgap of spin-coated and blade-coated films was 1.6 eV and 1.59 eV, respectively. This bandgap value corresponds to other literature reporting E_g of methylammonium lead iodide (Jeon, N. et al., 2015). Although the peak intensity was relatively low for the blade-coated sample, the PL spectra had a peak position at 775 nm (1.6 eV), indicating that the bandgap of both films was the same (Figure 36).

Figure 36: Optoelectronic Comparison of Blade- and Spin-Coated Films

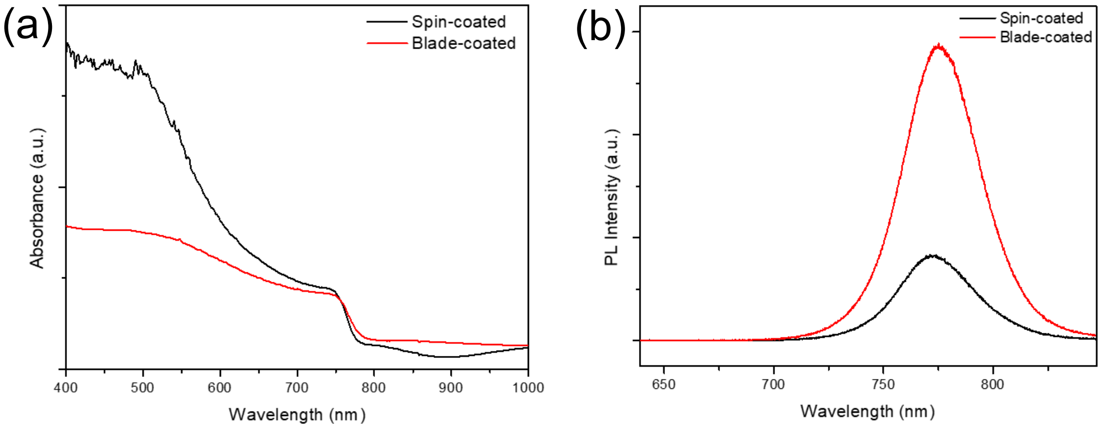

(a)UV-vis spectra of spin-coated (black) and blade-coated (red) $MAPbI_3$/glass. (b) Photoluminescence (PL) spectrum of spin-coated (black) and blade-coated (red) $MAPbI_3$

Source: University of California, San Diego

The current density-voltage measurement was performed on both spin-coated and blade-coated devices (Figure 37). The best performing blade-coated cell showed PCE of 15.35 percent, which is compatible to 16.35 percent PCE for spin-coated samples.

Figure 37: JV Curves of Spin-Coated and Blade-Coated PSCs

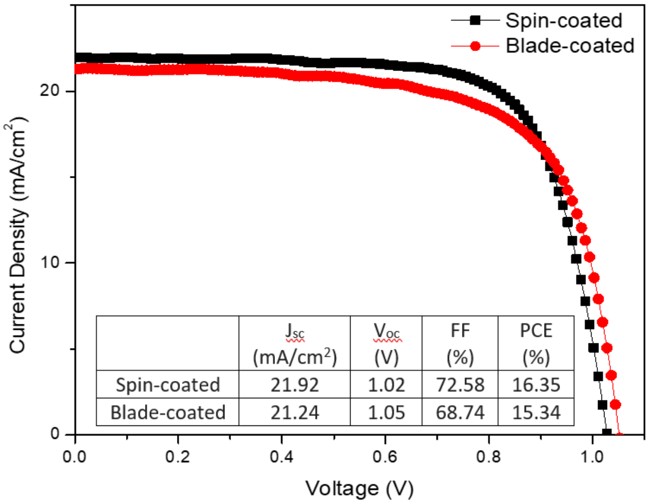

	J_{SC} (mA/cm^2)	V_{OC} (V)	FF (%)	PCE (%)
Spin-coated	21.92	1.02	72.58	16.35
Blade-coated	21.24	1.05	68.74	15.34

Blade-coated devices are competitive with spin-coated reference devices.

Source: University of California, San Diego

Larger Area

The blade-coated large-area perovskite cells were fabricated in two ways: the single-cell combined structure and the monolithic module.

The first strategy (Figure 38) was performed to evaluate the uniformity and film quality of blade-coated perovskite films for large areas without monolithic module designs. Since the monolithic structure involved numerous new factors such as scribing quality, structure design, optimization of large-area ETL and HTL, the project team first established a proper perovskite blade-coating protocol for a large substrate, then moved on to a module structure. The project team blade-coated the perovskite solution on 2.5 x 5 cm^2 substrate, then cut it into two 2.5 x 2.5 cm^2 solar cells.

Figure 38: Single-Cell Combined Solar-Cell Scheme on Small to Larger Substrates

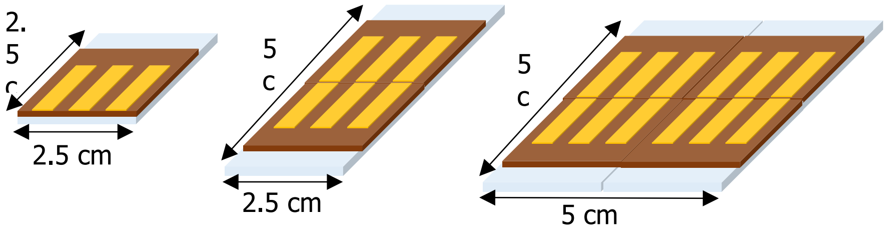

Cleaving of large area substrates after fabrication of the absorber and device layers enables testing of the large-area processing separate from mini-module monolithic integration challenges.

Source: University of California, San Diego

The other layers besides perovskite, such as ETL, HTL and top electrode deposition, were fabricated in the same way as in the small area cells. In Figure 39 the first half of the substrate showed PCE of 13.77-percent and the other half showed 0.97-percent, indicating the large-area perovskite coating was not yet optimized.

Figure 39: Large-Area Devices Made by Blade Coating

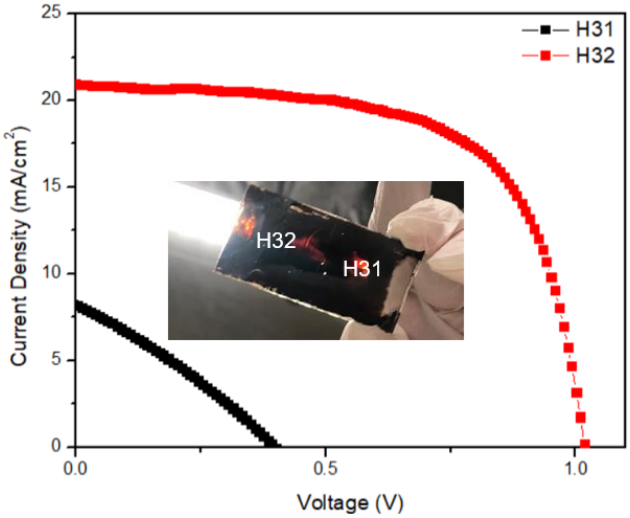

	J_{sc} (mA/cm^2)	V_{oc} (V)	FF (%)	PCE (%)
H31	8.21	0.40	29.53	0.97
H32	20.93	1.02	64.61	13.77

JV curves of two cells, blade-coated in a large substrate (2.5 x 5 cm^2) and subsequently divided into small cells (2.5 x 2.5 cm^2)

Source: University of California, San Diego

A monolithic perovskite solar module was fabricated with the active module area of 9.12 cm^2. The physical vapor deposited SnO_2 and was laser scribed (the so-called P1 scribe). $MAPbI_3$ precursor solution and spiro-MeOTAD was blade-coated on top of the SnO_2 and P2 and scribed. Finally, each subcell was divided after gold evaporation. The J_{sc} was 3.65 mA/cm^2, which is significantly lower than for a 2.5 x 2.5 cm^2 single cell. Fill factor and PCE are also lower than single-cell data. However, V_{oc} of 1.72 V indicates that the subcells are successfully series-connected, resulting in higher V_{oc} than in the small cells (around 1.2 V).

Outdoor Testing

The goal of this subtask was to develop outdoor testing facilities capable of tracking the operational stability of perovskite devices and modules under realistic operational conditions (for example, ambient conditions under natural sunlight without temperature control) to estimate their expected lifetimes in real-world deployment.

Hardware

To run outdoor operational stability tests, the project team developed the outdoor testing hardware pictured in Figure 40.

Figure 40: Outdoor Testing Setup

Hardware used for outdoor testing included an air-conditioned box to house and protect the electronics, a waterproof junction box to connect the electronics to the cells, and an angle adjustable mounting rack to mount the cells.

Source: University of California, San Diego

The outdoor test system is in the rooftop research facility on the rooftop of Atkinson Hall at UCSD, which receives approximately 1500 hours of usable sunlight per year (Google Project Sunroof estimate). The system consists of an air-conditioned outdoor enclosure to protect the electronics, a junction box to allow waterproofing and easily swappable connections between the cell and the electronics, and an angle/spacing-adjustable mounting rack to mount the cells. The electronics include a high-resolution source measure unit to characterize the cells through either maximum power-point tracking or current voltage sweeps or both, several simple loads to hold cells near maximum power point where they would be during standard operation, and a relay-board capable of switching up to 24 minimodules between the load and measurement units. This system is coupled with a silicon photodiode light sensor to track light intensity and a thermocouple sensor to measure the temperature of the cells. Together these systems can age the mini modules under real world conditions while tracking stressors and calculating performance metrics from measurements that are insightful for understanding both device operation and degradation.

Because of the custom nature of the hardware and software desired for the outdoor testing at small laboratory scales, the project team contracted SOLARC GmbH to provide UCSD designs for hardware and a full software solution for outdoor testing. SOLARC previously designed a similar system for the Zürich University of Applied Sciences. After delays in designing the system with SOLARC (due to COVID-19), the project team finalized plans for a minimodule adjustable mounting rack, which the team constructed. The researchers also received a relay board from SOLARC to route electronic connections from devices to measurement units. In addition to hardware, SOLARC was contracted in 2020 to provide software to operate the relay board with electronic loads nominally designed to operate the hardware and measure solar-cell characteristics over time. SOLARC provided the project team iterations of improving software over the last 12 months of the project but did not permit the project team to directly collaborate on their proprietary software. Unfortunately, the software remained incapable of running the hardware to the unique specifications of the tests for the PSCs by the end of the project period.

In the end, the project team at UCSD wrote its own software to carry out basic tests on one to two modules at a time and will finalize software implementation of the 24-cell outdoor test facility past the project period.

Verification of System

To verify that the setup was operating as intended, the project team first studied an encapsulated silicon cell and monitored various device parameters through intermittent JV curves over a ~60-hour period. Due to the natural cycles of the sun, a 24-hour oscillatory fluctuation in all parameters, dominated by short-circuit current density, was expected. Results, shown in Figure 41, were in line with expectations and indicated that the software and hardware were behaving as intended. At night and under heavy shading, however, the lack of sunlight caused noise in the performance metrics.

Figure 41: Silicon Solar Cell Performance Metrics Over Time

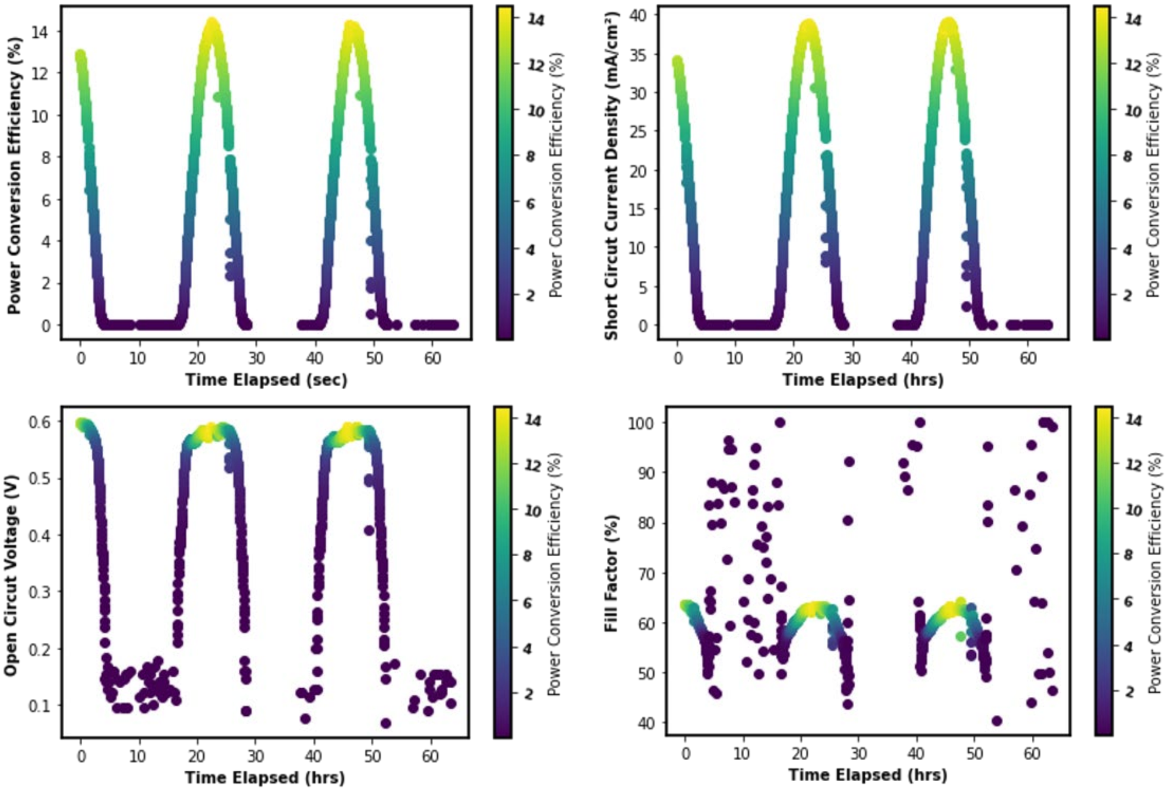

Power conversion efficiency, short circuit current density, open circuit voltage, and fill factor of a silicon device over time as a function of power conversion efficiency show the expected 24-hour periodicity due to the natural cycle of the sun, verifying that the setup is working as expected.

Source: University of California, San Diego

Perovskite Solar Cell Encapsulation

While many laboratory tests gauge cell response to a particular stressor or set of stressors, outdoor tests require the cells to be stable to all stressors expected during normal cell operation including: light, bias, temperature, oxygen, and humidity. Due to the well-documented moisture and oxygen sensitivity of perovskites, this requires a robust encapsulation scheme to keep moisture out of the cells. This stringent requirement for a moisture impermeable barrier has led much of the field to employ a glass encapsulant with a hermitic edge seal. As previous work of the project team showed that this can be achieved with a polyisobutylene (PIB) rubber edge seal (Runser, R., et al., 2021), this task employed the encapsulation strategy shown in Figure 42, resulting in the cells shown in Figure 43.

Figure 42: Encapsulation Scheme

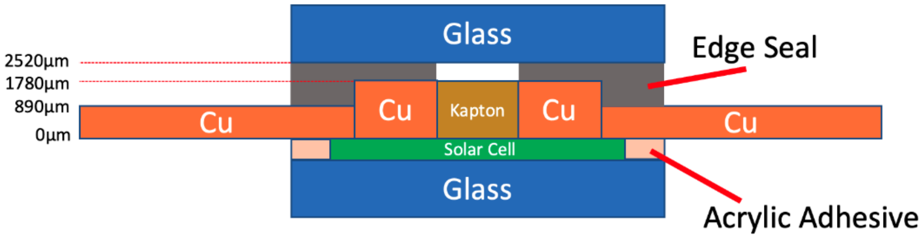

Current encapsulation scheme to contact the solar cell and protect it from external stressors.

Source: University of California, San Diego

Figure 43: Encapsulated Device

Top and bottom picture of encapsulated PSCs. Light enters the cell through the bottom of the device.

Source: University of California, San Diego

Initial Outdoor Perovskite Testing

As a final demonstration, the project team encapsulated a n-i-p FTO/nanoparticle SnO_2/$FA_{0.78}Cs_{0.22}Pb(I_{0.85}Br_{0.1}Cl_{0.05})_3$ perovskite/Spiro-OMeTAD/Au device using the encapsulation scheme just described and degraded it using the outdoor testing facility described at the beginning of this section. Results displayed in Figure 44 indicate that PCE losses are dominated by a rapid decrease in short-circuit current density. Additionally, these changes correspond well with a general discoloration of the film, likely indicating that the encapsulation needs improvement.

Figure 44: Perovskite Solar Cell Performance Metrics Over Time

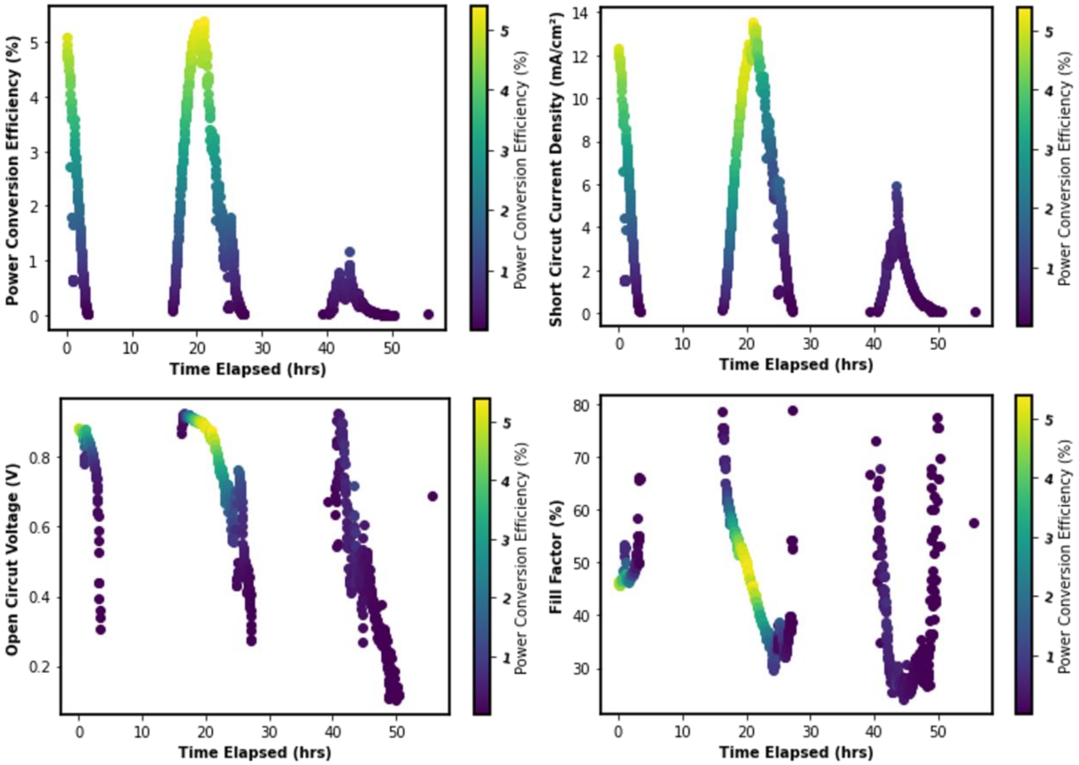

Power conversion efficiency, short circuit current density, open circuit voltage, and fill factor of a perovskite device over time as a function of power-conversion efficiency.

Source: University of California, San Diego

Conclusion

The principal components required for outdoor testing were established. Moving forward, the project team plans to improve the software received from SOLARC, improve the contact/encapsulation scheme, and build predictive models that correlate outdoor testing results with laboratory testing. Due to insufficient SOLARC software, the project team will develop software that achieves full control of the measurement instrumentation as originally designed. For encapsulation, the team intends to move towards the scheme displayed in Figure 45.

Figure 45: New Encapsulation Schematic

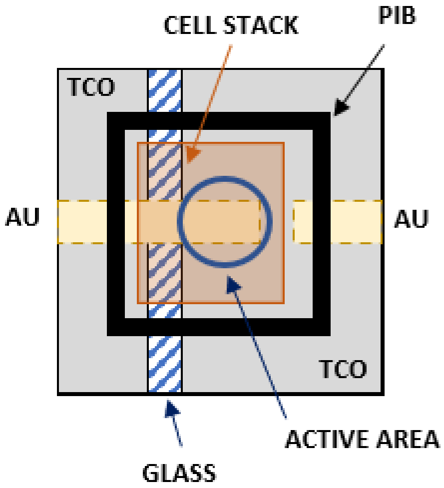

Schematic for the new encapsulation strategy. The new design allows encapsulation further away from the cell to minimize damage to the cell and removes the water permeable adhesive beneath the copper tape.

Source: University of California, San Diego

Overall, the project achieved the technical goals of the agreement. Studies in heated environments indicate that the durability of PSCs can be sufficient to pass industry standard damp heat testing using glass-glass encapsulation (CHAPTER 4). Large-area capable manufacturing processes were demonstrated and tested and achieved greater than 15-percent efficiency on substrates using processing achievable for ~100 cm^2 substrates (CHAPTER 5). During the project, the PCE of the cells improved 15-percent absolute to more than 20 percent. The project costs of perovskite PV remain significantly below existing commercial technology according to the literature, suggesting the potential for significant reductions in the unit cost of renewable-energy generation. The project also showed that accelerated stress testing over hundreds of hours make it likely that PSCs can potentially survive in the field for years.

CHAPTER 7: Technology and Knowledge Transfer

The project team's goal was to communicate critical advances in PSCs to as broad a base of stakeholders as reasonably achievable. The target audience primarily included the scientific and academic communities, relevant industry stakeholders in PV, printing, and electrochemical processing, and PV R&D specialists.

The primary means for knowledge transfer was dissemination of the project team's findings through peer-reviewed journal publications. Peer reviews reflect the high standard of the scientific community in evaluating work efforts and is a primary indicator of the value of the knowledge generated within the project. The project team published 16 articles in leading scientific journals including high-impact factor journals including *Science*, *Nature, Advanced Functional Materials*, *Advanced Materials*, *Chemistry of Materials*, and the *Journal of the American Chemical Society*.

In addition, the project team communicated the project findings at a number of meetings of professional societies and industry including both in-state conferences and national meetings. These efforts occurred throughout the project at regular intervals, at least annually.

The bibliography of the project team's publications and conference presentations is detailed in APPENDIX C.

Finally, toward the end of the project, the project team also presented the project's development efforts, analytical approaches, durability testing procedures, and results to several PV industry players interested in the development of the project including Swift Solar, Tandem PV, and Hunt Perovskite Technologies. Ultimately, this industry interaction led to one follow-on collaborative project led by Tandem PV, Inc., that will be supported by the U.S. Department of Energy for technology R&D and demonstration.

CHAPTER 8: Benefits to California

After 3.5 years, the project team successfully demonstrated:

1. Installing and integrating cost-effective distributed resources and energy generation, including renewable resources. This project advanced PSCs from early lab demonstrations to testing prototypes in a relevant operational environment, through both accelerated laboratory and outdoor testing. Further development and validation of PSCs may ensure their commercial deployment as distributed renewable-energy resources.
2. Reducing greenhouse gas emissions. Solar PV is a promising technology for reducing the embedded carbon cost of the grid. However, silicon PV retains a non-negligible carbon cost. Perovskite PV holds promise to further shave the energy and carbon cost of PV because of its low-temperature manufacturing.
3. Reducing capital costs. Although solar PV is now one of the cheapest, if not the cheapest, form of electricity production in sunny climates, continued reduction of PV costs would facilitate the introduction of complimentary load-balancing technologies such as batteries. PSCs promise to reduce manufacturing costs by using printing and other low-temperature processes.
4. Improving operating efficiency and reliability. This project extended the durability of perovskite solar cells to 100-1,000s of hours of constant operation and showed that intermittent "resting" could recover much of their observed degradation. By applying a mild temperature overnight, PSCs may be able to operate for commercially relevant lifespans (10+ years).
5. Developing new resources and processes, particularly renewable resources and processes which further supply technologies. The low-temperature manufacturing approaches introduced here for perovskite syntheses may enable new renewable-resource generation.

Advanced training of an innovative energy workforce is key to achieving California's current and future statutory environmental goals. The project supported up to 10 people working at UCSD, working 87 person-months during the project. This project contributed to the education and training of at least seven graduate students and two postdoctoral researchers. It led to two doctoral dissertations and several masters theses. One project alumnus is now working in California at a PSC startup. Another alumnus is working in California at a CO_2 conversion startup.

GLOSSARY AND LIST OF ACRONYMS

Term	Definition
Ag	Silver
Au	Gold
CB	chlorobenzene
CV	cyclic voltammetry
CVD	chemical vapor deposited
DMF	dimethylformamide
DMSO	Dimethyl sulfoxide
ETL	electron transport layer
EPIC	Electric Program Investment Charge
FA	Formamidinium
FTO	Fluorine-doped tin oxide
HTL	hole transport layer
ITO	indium tin oxide
JV	current density-voltage
LiTFSI	Lithium bis(trifluoromethanesulfonyl)imide
MA	Methylammonium
PCE	Power conversion efficiency
PIB	polyisobutylene
PL	photoluminescence
PSC	perovskite solar cells
PTAA	polytriarylamine
SnO_x	Tin oxide
SPO	Stabilized power output
SEM	Scanning electron microscopy
spiro-OMeTAD	2,2′,7,7′-tetrakis(N,N-di-p-methoxyphenyl-amine)9,9′-spirobifluorene
TA	transient absorption
tBP	4-Tert-butylpyridine
TCO	Transparent conducting oxide
XRD	X-ray diffraction
UCSD	University of California, San Diego / UC San Diego
Voc	Open circuit voltage

References

Meng, Ying Shirley, *et al.* 2019. Homogenized Halides and Alkali Cation Segregation in Alloyed Organic-Inorganic Perovskites. *Science* 363(6427), 627–31. https://doi.org/10.1126/science.aah5065.

Li, Yuheng and Kesong Yang. 2019. High-Throughput Computational Design of Organic–Inorganic Hybrid Halide Semiconductors beyond Perovskites for Optoelectronics. *Energy & Environmental Science* 7, 2233-2243. https://doi.org/10.1039/C9EE01371G.

Shannon, R. D. 1976. Revised Effective Ionic Radii and Systematic Studies of Interatomie Distances in Halides and Chaleogenides. *Acta Cryst* A32, 751-767. https://doi.org/10.1107/S0567739476001551.

Frau, Antonio F., Roderick B. Pernites and Rigoberto C. Advincula. 2010. A Conjugated Polymer Network Approach to Anticorrosion Coatings: Poly(Vinylcarbazole) Electrodeposition. *Industrial and Engineering Chemistry Research* 49(20), 9789–97. https://doi.org/10.1021/ie100813t.

Scriven, L. E. 1988. Physics and Application of Dip Coating and Spin Coating. *MRS Online Proceedings Library* 121, 717–29. https://doi.org/10.1557/PROC-121-717.

Wang, Shen, *et al*. 2018. Unveiling the Role of tBP–LiTFSI Complexes in Perovskite Solar Cells. *Journal of the American Chemical Society* 140(48), 16720-16730. https://doi.org/10.1021/jacs.8b09809.

Jung, Eui Hyuk, *et al.* 2019. Efficient, stable and scalable perovskite solar cells using poly(3-hexylthiophene). *Nature* 567, 511–515. https://doi.org/10.1038/s41586-019-1036-3.

Kegelmann, Lukas, *et al.* 2019. Mixtures of Dopant-Free Spiro-OMeTAD and Water-Free PEDOT as a Passivating Hole Contact in Perovskite Solar Cells. *ACS Appl. Mater. Interfaces* 11(9), 9172-9181. https://doi.org/10.1021/acsami.9b01332.

Yan, Weibo, *et al.* 2014. High-performance hybrid perovskite solar cells with polythiophene as hole-transporting layer via electrochemical polymerization. *RSC Advances*, 4(62), 33039-33046. https://doi.org/10.1039/C4RA05578K.

Kampmann, A., V. Sittinger, J. Rechid, and R. Reineke-Koch. 2000. Large area electrodeposition of CuInGaSe. *Thin Solid Films* 361, 309–313.

Krische, Bernd, Malgorzata Zagorska. 1989. Polythiophene synthesis by electropolymerization of thiophene and bithiophene. *Synthetic Metals* 33(3), 257-267. https://doi.org/10.1016/0379-6779(89)90472-4.

Jones-Albertus, Rebecca, *et al.* 2016. Technology advances needed for photovoltaics to achieve widespread grid price parity. *Progress in photovoltaics: research and applications* 24(9), 1272-1283. https://doi.org/10.1002/pip.2755.

Choi, Kyoungjun, *et al.* 2015. Reduced Water Vapor Transmission Rate of Graphene Gas Barrier Films for Flexible Organic Field-Effect Transistors. *ACS Nano* 9(6), 5818–24. https://doi.org/10.1021/acsnano.5b01161.

Green, Martin, *et al.* 2021. Solar Cell Efficiency Tables (Version 57). *Progress in Photovoltaics: Research and Applications* 29(1), 3–15. https://doi.org/10.1002/pip.3371.

Uddin, Ashraf, *et al.* 2019. Encapsulation of Organic and Perovskite Solar Cells : A Review. *Coatings* 9(2), 65. https://doi.org/10.3390/coatings9020065.

Wang, Peng, *et al.* 2019. Solution-Processable Perovskite Solar Cells toward Commercialization: Progress and Challenges. *Advanced Functional Materials* 29(47), 1807661. https://doi.org/10.1002/adfm.201807661.

Song, Zhaoning, *et al*. 2016. Perovskite Solar Cell Stability in Humid Air: Partially Reversible Phase Transitions in the PbI_2-CH_3NH_3I-H_2O System. *Advanced Energy Materials* 6(19), 1600846. https://doi.org/10.1002/aenm.201600846;

Aranda, Clara, Antonio Guerrero and Juan Bisquert. 2019. Crystalline Clear or Not: Beneficial and Harmful Effects of Water in Perovskite Solar Cells. *ChemPhysChem* 20(20), 2587–99. https://doi.org/10.1002/cphc.201900393;

Aristidou, Nicholas, *et al*. 2015. The Role of Oxygen in the Degradation of Methylammonium Lead Trihalide Perovskite Photoactive Layers. *Angewandte Chemie* 127(28), 8326–30. https://doi.org/10.1002/ange.201503153;

Senocrate, Alessandro, *et al*. 2018. Interaction of Oxygen with Halide Perovskites. *Journal of Materials Chemistry A* 6(23), 10847–55. https://doi.org/10.1039/C8TA04537B.

Xihong Hu *et al.*, "Air and Thermally Stable Perovskite Solar Cells with CVD-Graphene as the Blocking Layer," *Nanoscale* 9, no. 24 (2017): 8274–80, https://doi.org/10.1039/C7NR01186E; Peng You *et al.*, "Efficient Semitransparent Perovskite Solar Cells with Graphene Electrodes," 2015, https://doi.org/10.1002/adma.201501145.

Kim, Gi-hwan, *et al.* 2017. Fluorine Functionalized Graphene Nano Platelets for Highly Stable Inverted Perovskite Solar Cells. *Nano Lett*. 17(10), 6385-6390. https://doi.org/10.1021/acs.nanolett.7b03225.

Li, Hao, *et al.* 2017. Enhancing Efficiency of Perovskite Solar Cells via Surface Passivation with Graphene Oxide Interlayer. *ACS Applied Materials & Interfaces* 9(44), 38967–76. https://doi.org/10.1021/acsami.7b10773;

Yang, Qing Dan, *et al.* 2017. Graphene Oxide as an Efficient Hole-Transporting Material for High-Performance Perovskite Solar Cells with Enhanced Stability. *Journal of Materials Chemistry A* 5(20), 9852–58. https://doi.org/10.1039/c7ta01752a.

Kim, Jong Min, Sung Kim and Suk-Ho Choi. 2019. High-Performance n-i-p- Type Perovskite Photodetectors Employing Graphene-Transparent Conductive Electrodes N-Type Doped with Amine Group Molecules. *ACS Sustainable Chem. Eng*. 7(1), 734–39. https://doi.org/10.1021/acssuschemeng.8b04322;

Zhu, Menghua, *et al.*, 2019. Graphene-Modified Tin Dioxide for Efficient Planar Perovskite Solar Cells with Enhanced Electron Extraction and Reduced Hysteresis. *ACS Appl. Mater. Interfaces* 11(1), 666–673. https://doi.org/10.1021/acsami.8b15665.

Kim, Hyo Won, *et al.* 2013. Supplementary Material for Selective Gas Transport Through. *Science* 342(6154), 91–95, https://doi.org/10.1126/science.1236098.

Cheacharoen, Rongrong, *et al.* 2018. Encapsulating Perovskite Solar Cells to Withstand Damp Heat and Thermal Cycling. *Sustainable Energy and Fuels* 11, 2398–2406. https://doi.org/10.1039/c8se00250a;

Cheacharoen, Rongrong, *et al.* 2018. Design and Understanding of Encapsulated Perovskite Solar Cells to Withstand Temperature Cycling. *Energy & Environmental Science* 11(1), 144–50. https://doi.org/10.1039/C7EE02564E.

Khenkin, Mark V., *et al.* 2020. Consensus Statement for Stability Assessment and Reporting for Perovskite Photovoltaics Based on ISOS Procedures. *Nature Energy* 5(1), 35–49. https://doi.org/10.1038/s41560-019-0529-5.

Pellet, Norman, *et al.* 2014. Mixed-Organic-Cation Perovskite Photovoltaics for Enhanced Solar-Light Harvesting. *Angewandte Chemie - International Edition* 53(12), 3151–57. https://doi.org/10.1002/anie.201309361.

Jiang, Qi, *et al.* 2017. Planar-Structure Perovskite Solar Cells with Efficiency beyond 21%. *Advanced Materials* 29(46), 1–7. https://doi.org/10.1002/adma.201703852.

Jiang, Qi, *et al.* 2017. Enhanced Electron Extraction Using SnO2 for High-Efficiency Planar-Structure HC(NH2)2 PbI3-Based Perovskite Solar Cells. *Nature Energy* 2(16177). https://doi.org/10.1038/nenergy.2016.177;

Kim, Min Cheol, *et al.* 2019. Moth-Eye Structured Polydimethylsiloxane Films for High-Efficiency Perovskite Solar Cells. *Nano-Micro Letters* 11(1), 1–10. https://doi.org/10.1007/s40820-019-0284-y.

Kim, Minjin, *et al.* 2019. Methylammonium Chloride Induces Intermediate Phase Stabilization for Efficient Perovskite Solar Cells. *Joule* 3(9), 2179–92. https://doi.org/10.1016/j.joule.2019.06.014.

Kim, Dohyung, *et al.* 2019. Light- and Bias-Induced Structural Variations in Metal Halide Perovskites. *Nature Communications* 10(1), 1–9. https://doi.org/10.1038/s41467-019-08364-1;

Bryant, Daniel, *et al.* 2016. Light and Oxygen Induced Degradation Limits the Operational Stability of Methylammonium Lead Triiodide Perovskite Solar Cells. *Energy and Environmental Science* 9(5), 1655–60. https://doi.org/10.1039/c6ee00409a;

Aristidou, Nicholas, *et al.* 2017. Fast Oxygen Diffusion and Iodide Defects Mediate Oxygen-Induced Degradation of Perovskite Solar Cells. *Nature Communications* 8(15218), 1–10. https://doi.org/10.1038/ncomms15218;

Song, Zhaoning, *et al.* 2016. Perovskite Solar Cell Stability in Humid Air: Partially Reversible Phase Transitions in the PbI_2-CH_3NH_3I-H_2O System. *Advanced Energy Materials* 6(19), 1600846. https://doi.org/10.1002/aenm.201600846;

Eperon, Giles E., *et al.* 2014. Formamidinium Lead Trihalide: A Broadly Tunable Perovskite for Efficient Planar Heterojunction Solar Cells. *Energy and Environmental Science* 7(3), 982–88. https://doi.org/10.1039/c3ee43822h;

Saliba, Michael, *et al.* 2016. Cesium-Containing Triple Cation Perovskite Solar Cells: Improved Stability, Reproducibility and High Efficiency. *Energy & Environmental Science* 9, 1989-1997. https://doi.org/10.1039/C5EE03874J.

Lee, Jin Wook, *et al.* 2015. Formamidinium and Cesium Hybridization for Photo- and Moisture-Stable Perovskite Solar Cell. *Advanced Energy Materials* 5(20), 1501310. https://doi.org/10.1002/aenm.201501310;

Yi, Chenyi, *et al.*, 2016. Entropic Stabilization of Mixed A-Cation ABX 3 Metal Halide Perovskites for High Performance Perovskite Solar Cells. *Energy & Environmental Science* 9(2), 656–62. https://doi.org/10.1039/C5EE03255E;

Saliba, Michael, *et al.* 2016. Cesium-Containing Triple Cation Perovskite Solar Cells: Improved Stability, Reproducibility and High Efficiency. *Energy & Environmental Science* 9, 1989-1997. https://doi.org/10.1039/C5EE03874J

Bai, Sai, *et al.* 2019. Planar Perovskite Solar Cells with Long-Term Stability Using Ionic Liquid Additives. *Nature* 571(7764), 245–50. https://doi.org/10.1038/s41586-019-1357-2;

Xu, Jixian, *et al.* 2020. Triple-Halide Wide-Band Gap Perovskites with Suppressed Phase Segregation for Efficient Tandems. *Science* 367(6482), 1097–1104. https://doi.org/10.1126/science.aaz4639.

Yavari, Mozhgan, *et al.* 2018. Greener, Nonhalogenated Solvent Systems for Highly Efficient Perovskite Solar Cells. *Advanced Energy Materials* 8(21), 1800177. https://doi.org/10.1002/aenm.201800177;

Zhao, Pengjun, *et al.* 2018. Antisolvent with an Ultrawide Processing Window for the One-Step Fabrication of Efficient and Large-Area Perovskite Solar Cells. *Advanced Materials* 30(49), 1–8. https://doi.org/10.1002/adma.201802763.

Li, Nengxu, *et al.* 2020. Microscopic Degradation Mechanism in MA-Free Perovskite Solar Cells under Various Stressors Intrinsic to Operation Nengxu. *Joule* 4(8), 1743-1758. https://doi.org/10.1016/j.joule.2020.06.005.

Li, Zhen, *et al.* 2018. Scalable Fabrication of Perovskite Solar Cells. *Nature Reviews Materials* 3(4), 18017. https://doi.org/10.1038/natrevmats.2018.17.

Le Berre, Mael, Yong Chen and Damien Baigl. 2009. From Convective Assembly to Landau-Levich Deposition of multilayered phospholipid films of controlled thickness. *Langmuir* 25(5), 2554–57. https://doi.org/10.1021/la803646e.

Deng, Yehao, *et al.* 2018. Surfactant-Controlled Ink Drying Enables High-Speed Deposition of Perovskite Films for Efficient Photovoltaic Modules. *Nature Energy* 3(7), 560–66. https://doi.org/10.1038/s41560-018-0153-9.

Li, Jianbo, *et al.* 2017. Solution Coating of Superior Large-Area Flexible Perovskite Thin Films with Controlled Crystal Packing. *Advanced Optical Materials* 5(11). https://doi.org/10.1002/adom.201700102.

Reese, Matthew O., *et al.* 2018. Increasing Markets and Decreasing Package Weight for High-Specific-Power Photovoltaics. *Nature Energy* 3(11), 1002–12. https://doi.org/10.1038/s41560-018-0258-1.

Kavan, Ladislav, Ludmilla Steier and Michael Gratzel. 2017. Ultrathin Buffer Layers of SnO2 by Atomic Layer Deposition: Perfect Blocking Function and Thermal Stability. *Journal of Physical Chemistry C* 121(1), 342–50. https://doi.org/10.1021/acs.jpcc.6b09965.

Jeon, Nam Joong, *et al.* 2015. Compositional Engineering of Perovskite Materials for High-Performance Solar Cells. *Nature* 517(7535), 476–80. https://doi.org/10.1038/nature14133.

Runser, Rory, *et al.* 2021. Stability of Perovskite Films Encapsulated in Single- and Multi-Layer Graphene Barriers. *ACS Appl. Energy Mater*. 4(9), 10314–10322. https://doi.org/10.1021/acsaem.1c02240.

Huang, Jin-hua, *et al.* 2015. Direct Conversion of $CH_3NH_3PbI_3$ from Electrodeposited PbO for Highly Efficient Planar Perovskite Solar Cells. *Scientific Reports* 5(15889). https://doi.org/10.1038/srep15889;

Annal Therese, G. Helen, and P Vishnu Kamath. 2000. Electrochemical Synthesis of Metal Oxides and Hydroxides. *Chemistry of Materials* 12(5), 1195–1204. https://doi.org/10.1021/cm990447a.

Peulon, Sophie, and Daniel Lincot. 1996. Cathodic Electrodeposition from Aqueous Solution of Dense or Open-Structured Zinc Oxide Films. *Advanced Materials* 8(2), 166–70. https://doi.org/10.2514/6.2013-2163.

Lim, Jonghun, and Michael R. Hoffmann. 2019. Substrate Oxidation Enhances the Electrochemical Production of Hydrogen Peroxide. *Chemical Engineering Journal* 374, 958–64. https://doi.org/10.1016/j.cej.2019.05.165.

Sawatani, Seiichi, *et al.* 2005. Formation of Highly Crystallized β-PbO Thin Films by Cathodic Electrodeposition of Pb and Its Rapid Oxidation in Air. *Advanced Functional Materials* 15(2), 297-302. https://doi.org/10.1002/adfm.200400086;

Zhitomirsky, I., *et al.* 1995. Electrochemical Preparation of PbO Films. *J. Mater. Sci. Lett*. 14(11), 807–10. https://doi.org/10.1007/BF00278136.

Jiang, Yan, *et al.* 2018. Combination of Hybrid CVD and Cation Exchange for Upscaling Cs-Substituted Mixed Cation Perovskite Solar Cells with High Efficiency and Stability. *Advanced Functional Materials* 28(1). https://doi.org/10.1002/adfm.201703835;

Chen, Haining, *et al.* 2015. A Scalable Electrodeposition Route to the Low-Cost, Versatile and Controllable Fabrication of Perovskite Solar Cells. *Nano Energy* 15, 216–26. https://doi.org/10.1016/j.nanoen.2015.04.025.

CALIFORNIA
ENERGY COMMISSION

CALIFORNIA
NATURAL
RESOURCES
AGENCY

ENERGY RESEARCH AND DEVELOPMENT DIVISION

Appendix A: Electrochemical Deposition of Perovskite Seed Layer

June 2024 | CEC-500-2024-029

APPENDIX A: Electrochemical Deposition of Perovskite Seed Layer

Electrochemical Deposition of Seed Layer

Electrochemical deposition has shown promise to produce conformal coating as long as there is a uniform conductive path. For metal oxide deposition, the cathodic reaction or the "electro-generated base" method is commonly used (Huang, J. et al., 2015; Therese, G. et al., 2000) and relies on the initial metal hydroxide formation at the cathode electrode where the most amount of OH^- ions are found. This is followed by the metal hydroxide conversion to metal oxide due to hydration (Peulon, S. and Lincot, D., 1996). In this project, a 3-electrode system was used with cathodic current applied on the working electrode. The working electrode is the device substrate, coated with a transparent conducting oxide, the counter electrode used was Pt mesh, and the reference electrode was Ag/AgCl. In the research environment, the 3-electrode configuration was utilized to finely control and monitor the deposition profiles such as change of current density and voltage applied on working electrodes as a function of time.

To start, the project team looked into the effect of hydrogen peroxide (H_2O_2) concentration on film morphology. Since H_2O_2 can be decomposed on the cathode surface (Lim, J. and Hoffman, M. 2019), controlling H_2O_2 tuned the reaction rate by limiting the reactant concentration. A total of four hydrogen peroxide concentrations were tested in the range of 0.03 to 0.19 molar concentration. When the concentration was high (> 0.1 M), the surface of the deposited films has a large density of clusters that have a size in the micron-scale. On the other hand, relatively uniform films were deposited with lower concentrations of hydrogen peroxide. Aside from controlling the concentration of H_2O_2, the amount of lead can also affect the film quality and final composition significantly. Leveraging previous efforts made on lead oxide deposition, the concentration of lead acetate is kept at low concentration (2 mM) to obtain films with PbO_x as opposed to Pb or $Pb(OH)_2$ formation when Pb^{2+} concentration is higher (above 20 mM) (Sawantani, S. et al., 2015; Zhitomirsky, I. et. al, 1995). Thus, to achieve uniform films with good coverage, the project team limited the concentration of hydrogen peroxide to be 0.06 M.

In addition to concentration of reactants, current density and deposition temperature were two variables that can affect rate of reaction considerably. Applied current density appeared to be a stronger factor than electrolyte temperature on affecting reaction rate. Lowering both current density and temperature allowed the electrodeposited film to have as smooth a surface as possible. A two-dimension experimental space was used to study the impact of both current density and deposition temperature on final film morphology. The corresponding SEM image of each condition is shown in Figure A-1, where electrolyte temperature is grouped by row and applied current density is listed as column. Comparing the SEM images on Figure A-1 row 2, the project team found that number of clusters decreases as current density reduced from 0.16 to 0.11 mA/cm^2. High density small clusters were found using high current density (0.16 mA/cm^2), while the cluster density was gradually decreased as current density becomes smaller. Unlike current density, electrolyte temperature had a smaller impact on surface morphology. This is shown clearly in the case of using 0.13 mA/cm^2, as shown in Figure A-1, Column 2. These observations suggest that the combination of lower temperature and small current density yielded films with a smoother surface and a lesser number of aggregates. PbO_x films prepared using 0.13 or 0.11 mA/cm^2 at 113°F (45°C) were used to perform the conversion experiment.

Figure A-1: Effect of Temperature and Applied Current Density on Film Morphology

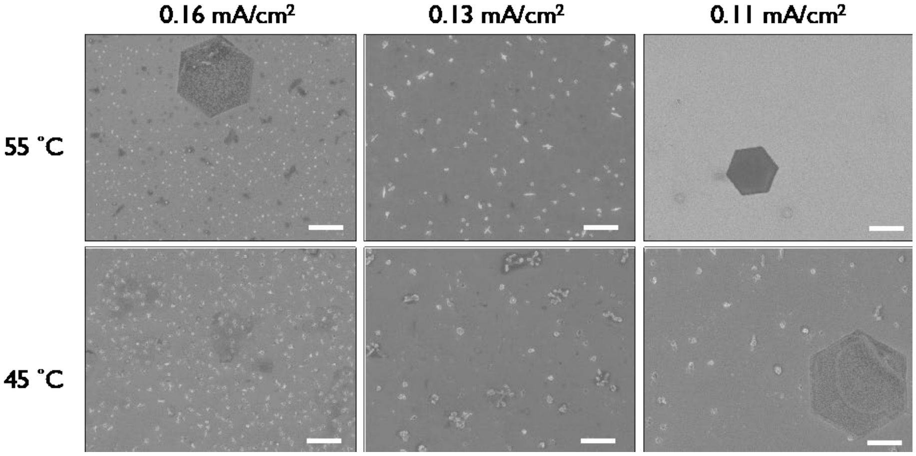

SEM images of films deposited at using the corresponding current density and electrolyte temperature stated on the top and the left, respectively. The films are deposited using the same amount of H_2O_2 (0.06 M) with total charge density of 0.065 C/cm^2. Length of scale bar is 10 µm.

Progress and Development in Conversion from Seed Layer to Absorber

Solution and chemical vapor conversion were the two common that the project team use to turn perovskite seed layers (PbI_2 or PbO_x) into photoactive lead halide perovskite absorbers. The solution approach was one of the earlier conversion steps developed for producing high performance solar cells. In solution conversion, the organic halide components are introduced to the seed layers (PbI_2 or PbO_x) by submerging them in a bath that contains organic cations and halide ions. Selecting proper solvent for the conversion bath can be challenging, as organic halide salts have high solubility in polar solvents but polar solvents will also cause perovskite to degrade. IPA is commonly used as the solvent in conversion bath while considering the relative solubility of organic halide and converted perovskite. Unlike solvent conversion, chemical vapor conversion has nitrogen as the carrying medium and the conversion depends upon on the rate of organic halide vapor reaching the seed layer. Generally speaking, the rate of crystallization of perovskite is slower in vapor conversion than solution conversion based on the reported reaction time in literatures (Jiang, Y. et al., 2018; Chen, H. et al., 2015). In this subtask, the project team explored these two conversion methods on both spin-coated PbI_2 and electrochemically deposited PbO_x films.

The project team found that chemical vapor conversion is a better alternative and yields better film morphology and optoelectronic performance. A 2-zone tube furnace was utilized for vapor conversion, for achieving mixed halide, and A-site cation perovskites. With 2-zone furnace, the vapor ratio between MABr and FAI was easily tuned by adjusting the set temperature on each zone. MABr has a lower temperature than FAI. The project team first tested the project team's chemical vapor setup using PbI_2 substrates. During the process, the yellow color spin-coated PbI_2 films were successfully converted to dark brown halide perovskite. This was confirmed by the corresponding XRD and PL.

To achieve the target composition, the project team adapted a two-step vapor conversion using the same setup. This two-step (2-Step) vapor conversion showed promising results by comparing the change of structural and optoelectronic property with respect to one-step conversion as shown in Figure A-2. XRD patterns of 2-Step converted films align well with the literature reported $FAPbI_3$ diffraction pattern, which also agrees with PL peak position. Two-step vapor conversion was considered due to conversion rate difference between FAI and MABr vapor. FAI vapor had a slower reaction rate than MABr based on experimental observation. When there was only FAI vapor present, PbI_2 or PbO_x layers take almost 1 hour to fully convert to $FAPbI_3$. However, the conversion process took less than 10 minutes if FAI/MABr mixed vapor is used. This suggests that MABr can react with seed layer thin film much more quickly than FAI, which may yield high MA or Br concentration in the converted absorbers. To avoid forming absorbers with high Br content, the project team implemented a two-step vapor conversion approach, in which the project team used FAI vapor only to convert seed layers to $FAPbI_3$ first, and then exposed the $FAPbI_3$ absorber to FAI/MABr mixed vapor. This relied on ion exchange process to gradually replacing FA/I to MA/Br on perovskite crystal lattice.

Figure A-2: Structural and Optoelectronic Properties Comparison Between 1-Step and 2-Step Vapor Converted Films

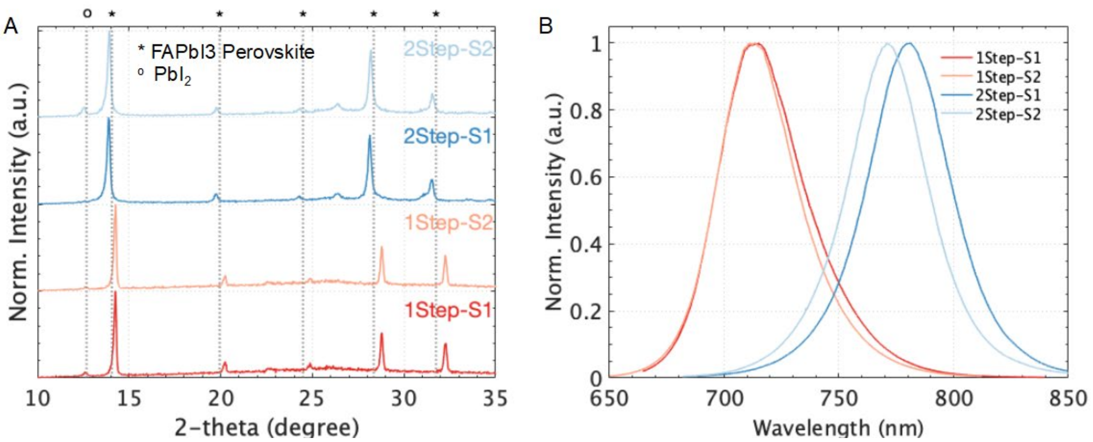

XRD and PL spectra is shown in (A) and (B) respectively. These are the converted films using PbI_2 as the seed layers.

Two-step vapor converted films had smooth surface morphology and good coverage compared to solution conversion. SEM images of surface morphology and converted film thickness, using both PbI_2 and PbO_x thin films, are shown in Figure A-3. Although converted films using electrodeposited PbO_x had large perovskite clusters with size in the range of ~ 2 µm. the surrounding regions look smooth and packed with larger crystallites than converted film using PbI_2. Glass, FTO and perovskites are the three layers the project team can identify from cross-section images. When looking at the perovskite layer, converted PbO_x films also had good columnar grains and their thickness in the range of 300 to 400 nm. In contrast to converted PbO_x films, converted PbI_2 films had small grains stacked up from substrates to film surface, which can create barriers for charge extraction due to carrier recombination at grain boundaries.

Figure A-3: Surface Morphology of 2-Step Vapor Converted Films

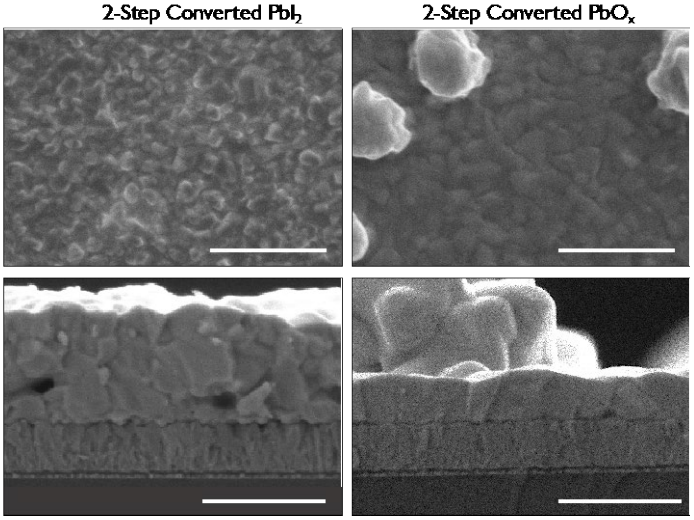

Plan view and cross-section view SEM images are shown as top and bottom row. Images on the left column are taken on converted PbI_2 film and the ones on the right are measured on converted PbO_x films. Scale bar in plain view and cross-section image is 3 and 1 µm, respectively.

CALIFORNIA
ENERGY COMMISSION

CALIFORNIA
NATURAL
RESOURCES
AGENCY

ENERGY RESEARCH AND DEVELOPMENT DIVISION

Appendix B: Characterization of Graphene Barrier Layer Properties and Evaluation for Perovskites

June 2024 | CEC-500-2024-029

APPENDIX B: Characterization of Graphene Barrier Layer Properties and Evaluation for Perovskites

The fabrication procedure for 2-layer graphene on a Parylene support polymer is shown in Figure B-1. Monolayer graphene was obtained from GrollTex, Inc., adhered to 5 µm thick Parylene-C, and was used without further modification. Two- and three-layer graphene were prepared as follows. First, monolayer graphene on copper foil (5 cm × 5 cm) was spin-coated with a 4 weight (wt) percent PMMA solution in anisole at 4000 rpm for 60 s. After annealing at 302°F (150°C) for 5 minutes to remove any remaining anisole, the copper was etched in a 0.05 g/mL solution of ammonium persulfate (APS) in water for two hours, until fully removed. The resulting floating PMMA/graphene was transferred to a clean water bath. Separately, a 5 cm × 5 cm piece of graphene/Parylene-C was taped to a glass slide, graphene facing up. The PMMA/graphene was transferred directly onto the graphene/Parylene-C/glass slide, with the two graphene layers in direct contact, and allowed to dry overnight in a desiccator. Finally, the PMMA was removed by etching in a 122°F (50°C) bath of acetone for five minutes, then rinsed with IPA and allowed to dry. This process was repeated once more to yield 3-layer graphene. Successful graphene transfer was confirmed via UV-vis (Figure B-3) showing a successive decrease in optical transmission with each additional layer of grapheme.

Figure B-1: Schematic Showing the Preparation of Multi-layer Graphene Barrier Films

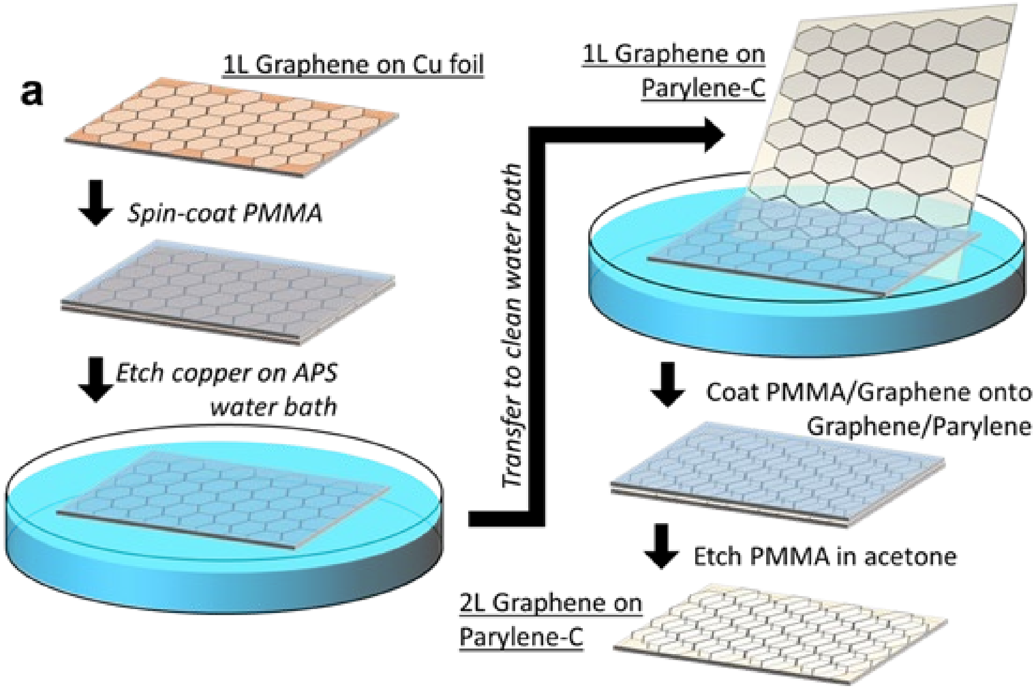

The CVD deposited graphene is protected with PMMA and the copper growth substrate is removed. It can then be transferred to another graphene sheet. This process is iterative and can be used to adhere several layers of graphene to one another.

Characterization of Transport and Defect Properties in Graphene

Air Transmission Rate

Transmission of air through the project team's barrier films was measured using a custom-built isochoric gas permeability measurement apparatus. Figure B-2 shows a schematic and picture of the project team's setup along with a trace of pressure vs time for the project team's control Parylene-C (0L) and the project team's graphene barrier layers (1L to 3L). The project team observed a greater rate of pressure increase from the project team's control sample, indicating that the project team's graphene barrier possesses a decreased air transmission rate and is thus a better barrier against air (and presumably oxygen) transmission. Upon the addition of multiple graphene layers, the barrier function of the encapsulant demonstrates potential for marginal improvement. However, the preparation of multi-layer graphene requires extensive handling which can introduce additional defects to the graphene films potentially counteracting the effects.

Figure B-2: Measurement of Air Transmission Rate

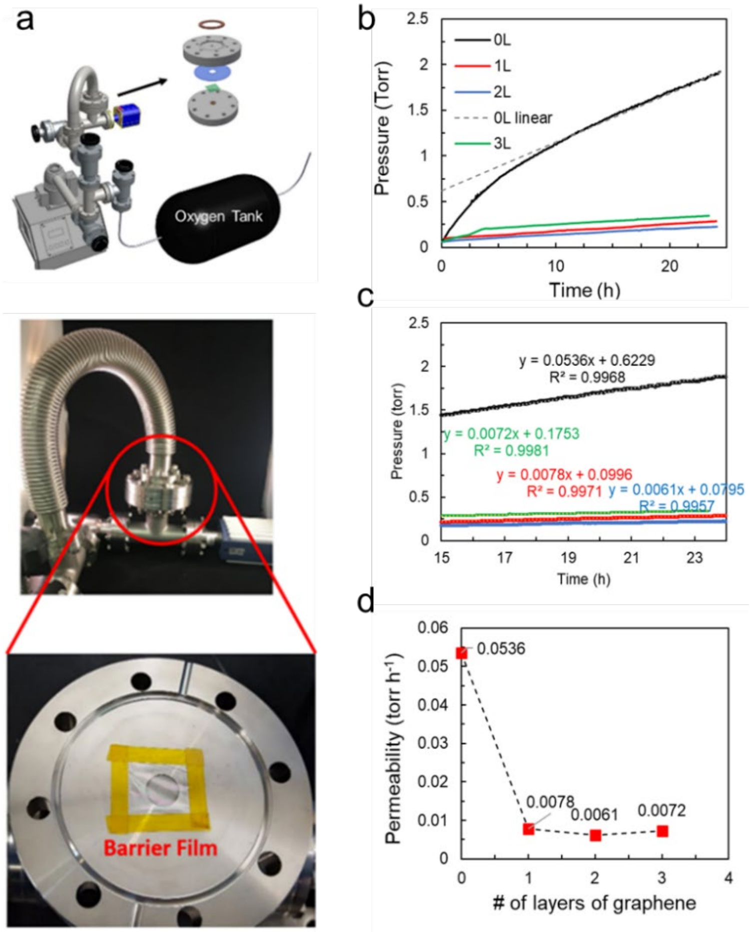

(A) Schematic of apparatus setup and photograph of device, showing attachment of barrier film for testing. (B) The pressure increases over time for 0 to 3 layers of graphene on parylene backbone showing the graphene's enhanced resistance to air transmission. (C) A closer look at the linear portion of the trace from which the permeability is extracted. (D) The summary of permeability as a function of the number of graphene layers.

UV-Visible-NIR Transmission Spectroscopy

Shown in Figure B-3, the UV-Vis spectrum from 350-800 nm was taken for encapsulants with 0-3 layers of graphene. With each additional graphene layer, the transmission decreases by ~2 percent over the range. As expected, thin-film interferences are observed in the oscillatory nature of the spectrum.

Figure B-3: UV-Vis Transmittance of Graphene Barrier Layers

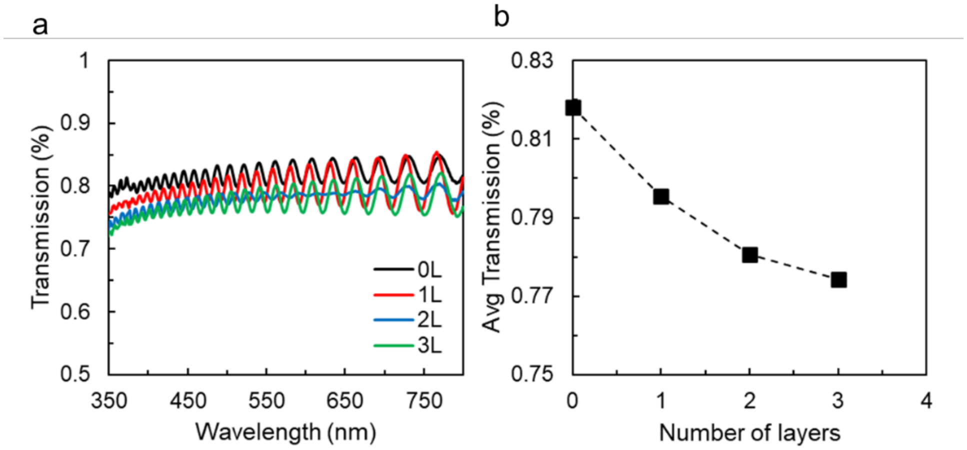

(A) UV-Vis spectrum of graphene and parylene control, over a range of wavelengths from 350 to 800 nm. (B) The integrated transmittance over the range as a function of the layers of graphene.

Characterization of Perovskite Robustness when Using Graphene Barriers

Understanding the differences in perovskite decay required probing the crystallographic properties of the films, namely through XRD and SEM. This in turn required removing the encapsulation to directly probe the surface (both PL and UV-vis could be done through the glass slide on which the perovskite film had been spun). While these metrology techniques could therefore only provide before/after comparisons, they nonetheless provided valuable insight into the degradation and evolution of the perovskite film. The x-ray diffractograms for the project team's films after aging for 200 hours are shown in Figure B-4a. The glass-encapsulated films remain virtually unchanged compared to films analyzed before aging, in alignment with the trends observed with UV-Vis and PL. In contrast, the graphene/parylene films all exhibit a substantial decrease in intensity of the main triple perovskite peak at $2\theta = 14°$, while also gaining a peak at $2\theta = 11.5°$, corresponding to the simpler perovskite δ-$FAPbI_3$ (a yellow-colored perovskite which gives rise to the color of these films after aging, as seen in Figure B-4). The formation of δ-$FAPbI_3$ is a water-catalyzed reaction wherein the methylammonium cation (MA) is liberated:

$$PSK + H_2O \rightarrow FAPbI_3 + HI + HMA + O_2$$

Interestingly, this peak is not seen in the exposed films, which decay completely to PbI_2. Thus, the presence of the semi-permeable parylene encapsulation material is necessary for the decay/healing behavior observed. Despite the overall ~50 percent mass loss observed via UV-vis among the graphene/parylene samples, the evolution of δ-FAPbI3 explains the continued active PL behavior observed during aging.

Figure B-4: X-Ray Diffraction Evolution During Multi-layer Graphene Test

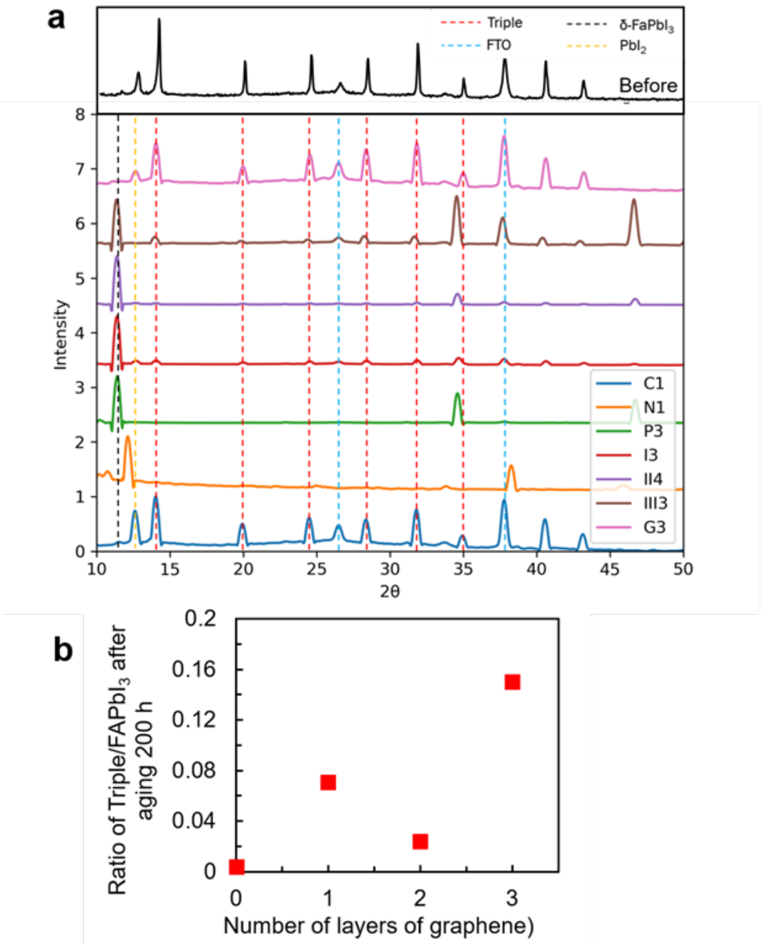

(A) XRD diffractograms for films after aging. (B) Ratio of peak intensity of triple-cation perovskite ($2\theta=14°$) to peak intensity of δ-FaPbI$_3$ ($2\theta=11°$) as a function of number of layers of graphene.

The x-ray diffractograms also allow for quantification of the degree of conversion between triple perovskite and δ-FAPbI$_3$ in the graphene/parylene films, by comparing the intensities of the peaks at 14° and 11.5°. This ratio is plotted in Figure B-4b and shows the dramatic effect that the addition of graphene conveys to the parylene support layer. While the triple perovskite in the 0L graphene has almost completely decayed into δ-FAPbI$_3$ (the ratio is not quite 0, but rather 0.007), the 1L graphene film has a 10-fold higher ratio of triple to δ-FAPbI$_3$, which itself is more than doubled again between the 1L and 3L graphene. The 2L graphene likely exhibits worse performance than the 1L due to the handling required to coat the additional graphene layer onto the commercial 1L graphene/parylene, which can induce defects/tears in graphene. These defects appear to be negated and improved upon by the addition of a third layer of graphene.

The films were also observed through scanning electron microscopy to observe morphological changes after the damp heat test. As shown in Figure B-5, the glass-aged films appear to be unchanged with no obvious degradation. However, while largely degraded, portions of the graphene encapsulated films (only 2L-graphene is shown here) exhibit significant grain growth. The unencapsulated control film is completely degraded.

Figure B-5: Before/After Scanning Electron Microscopy Imaging From Multi-Layer Graphene Test

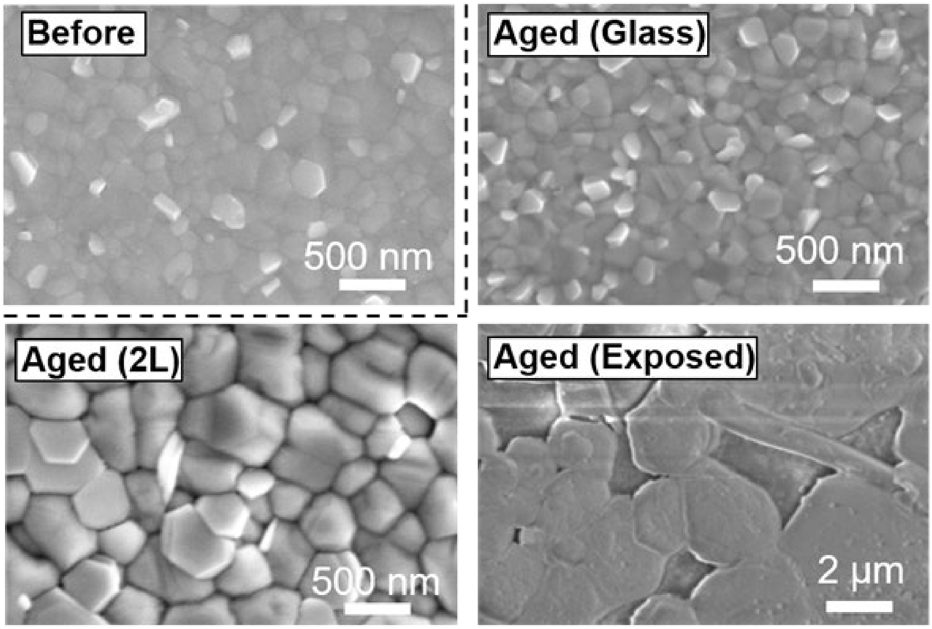

SEM images of representative films before and after aging showing the glass encapsulated films do not exhibit any significant morphological changes, the 2L-graphene films experience grain growth, and the exposed films are completely degraded.

CALIFORNIA
ENERGY COMMISSION

CALIFORNIA
NATURAL
RESOURCES
AGENCY

ENERGY RESEARCH AND DEVELOPMENT DIVISION

Appendix C: Published Articles, Presentations, and Work Products

June 2024 | CEC-500-2024-029

APPENDIX C: Published Articles, Presentations, and Work Products

---

Peer-Reviewed Publications:

1. Y. Luo, D. P. Fenning, *et al.* "The Relationship Between Chemical Flexibility and Nanoscale Charge Collection in Hybrid Halide Perovskites" **Advanced Functional Materials**, 28 (18), 1706995, 2018.
2. G. W. P. Adhyaska, S. Brittman, H. Abolins, A. Lof, X. Li, Y. Luo, T. Duevski, D. P. Fenning, E. C. Garnett, "Understanding Detrimental and Beneficial Grain Boundary Effects in Halide Perovskites," **Advanced Materials**, 30 (52), 1804792, 2018.
3. J.-P. Correa-Baena, Y. Luo, T. M. Brenner, J. Snaider, S. Sun, X. Li, M. A. Jensen, N. T. P. Hartono, L. Nienhaus, S. Wieghold, J. R. Poindexter, S. Wang, Y. S. Meng, T. Wang, B. Lai, M. V. Holt, Z. Cai, M. G. Bawendi, L. Huang, T. Buonassisi*, D. P. Fenning, "Homogenized halides and alkali cation segregation in alloyed organic-inorganic perovskites," **Science**, 363 (6427), 627, 2019.
4. X. Li, Y. Luo, M. V. Holt, Z. Cai, D. P. Fenning*,"Residual Nanoscale Strain in Cesium Lead Bromide Perovskite Reduces Stability and Shifts Luminescence," **Chemistry of Materials**, 31 (8), 2778, 2019.
5. R. Wang, J. Xue, K.-L. Wang, Z-K. Wang, Y. Luo, D. P. Fenning, G. Xu, S. Nuryyeva, T. Huang, J. L. Yang, Y. Zhao, J. Zhu, S. Tan, I. Yavuz, K. Houk, Y. Yang, "Unveiling the Constructive Molecular Configuration in Surface Defect Passivation of Perovskite Photovoltaics," **Science**, 366 (6472), 1509, 2019.
6. M. Kodur, R. E. Kumar, Y. Luo, D. N. Cakan, X. Li, M. Stuckelberger, D. P. Fenning, "X-ray Microscopy of Halide Perovskites: Techniques, Applications, and Prospects," **Advanced Energy Materials**, 10.1002/aenm.201903170.
7. S. Wang, Y.S. Meng*, et al.,* "Unveiling the Role of tBP-LiTFSI Complexes in Perovskite Solar Cells" , **Journal of the American Chemical Society**,2018,140 (48), 16720-16730, 2018.
8. Dong Geon Lee, Min-cheol Kim, Shen Wang, Byeong Jo Kim, Ying Shirley Meng, Hyun Suk Jung, "Effect of Metal Electrodes on Aging-Induced Performance Recovery in Perovskite Solar Cells," **ACS Appl. Mater. Interfaces** 2019, 11, 51, 48497-48504.
9. S. Wang, A. Cabreros, Y. Yang, A. S. Hall, S. Valenzuela, Y. Luo, J.-P. Correa- Baena, M.-C. Kim, Ø. Fjeldberg, D. P. Fenning, Y. S. Meng*, "Impacts of the Hole Transport Layer Deposition Process on Buried Interfaces in Perovskite Solar Cells," **Cell Press Physical Science**, 1(7), 100103, 2020.

10. Y. Luo, P. Parikh, T. M. Brenner, J.-P. Correa-Baena, T. Buonassisi, Y. S. Meng, D. P. Fenning, "Quantitative Specifications to Avoid Degradation during E- beam and Induced Current Microscopy of Halide Perovskite Devices," **Journal of Physical Chemistry C**, 10.1021/acs.jpcc.0c06733, 2020.
11. Y. Lei, Y. Chen, Y. Li, S. Lee, W. Choi, H. Tsai, K. Wang, Y. Luo, X. Zheng, C. Wang, C. Wang, H. Hu, Y. Li, B. Qi, M. Lin, Z. Zhang, D.P. Fenning, S. Dayeh, T. N. Ng, K. Yang, J. Yoo, W. Nie, S. Xu, "A Fabrication Process for Flexible Single-Crystal Perovskite Devices," **Nature**, 583, 790-795, 2020
12. M. E. Stuckelberger, T. Nietzold, B. M. West, Y. Luo, X. Li, J. Werner, B. Niesen, C. Ballif, V. Rose, D. P. Fenning, M. I. Bertoni, "Effect of X-rays on Perovskite solar cells," **Journal of Physical Chemistry C**, early view online, 2020
13. José Carlos Germino, R. Szostak, S. G. Motti, R. F. Moral, P. E. Marchzi, H. S. Seleghini, L. G. Bonato, F. Lopes de Arau`jo, T. D. Z. Atvars, L. M. Herz, D. P. Fenning, A. Hagfeldt, A. F. Noguiera, "Post-passivation of Multication Perovskite with Rubidium Butyrate," **ACS Photonics**, early view online, 2020.
14. N. Li, Y. Luo, Z. Chen, X. Niu, X. Zhang, J. Lu, R. Kumar, J. Jiang, H. Liu, X. Guo, B. Lai, G. Brocks, Q. Chen, S. Tao, D. P. Fenning, H. Zhou, "Microscopic Degradation in Formamidinium-Cesium Lead Iodide Perovskite Solar Cells under Operational Stressors," **Joule**, early view online, 2020.
15. M.-C. Kim, N. Ahn, D. Cheng, M. Xu, X. Pan, S. J. Kim, Y. Luo, D. P. Fenning, S.-Y. Ham, K. Jeong, M. Choi, Y. S. Meng, "Imaging Real-time Amorphization of Perovskite Solar Cells under Electrical Bias," **ACS Energy Letters**, 2021, 6, 3530.
16. Rory Runser, Moses Kodur, Justin Skaggs, Deniz Cakan, Juliana B. Foley, Mickey Finn III, David Fenning, Darren J. Lipomi. "Stability of perovskite films encapsulated in single- and multi-layer graphene barriers." **ACS Applied Energy Materials, 2021**, 4, 9, 10314-10322.

Conference Presentations (Talks)

- Yanqi Luo, P. Khoram, S. Brittman, B. Lai, E. C. Garnett, D. P. Fenning, "Detection of A Shifting Bromine Concentration in Hybrid Perovskites By X-ray Fluorescence Microscopy," IEEE Photovoltaic Specialists Conference, Washington D.C., June 2017.
- Yanqi Luo, B.-E. Cohen, X. Li, B. Lai, L. Etgar, D. P. Fenning, "Investigating Nanoscale Determinants of Charge Collection in Quasi-2D Perovskite Solar Cells," IEEE Photovoltaic Specialists Conference, Washington D.C., June 2017.
- David P. Fenning, "In Pursuit of Perfection: How Non-Stoichiometry at the Nanoscale Affects Perovskites Solar Cells," UC Solar Symposium, Public Utilities Commission, San Francisco, CA, October 2017.
- Yanqi Luo, P. Khoram, S. Brittman, Z. Zhu, B. Lai, S. P. Ong, E. C. Garnett, D. P. Fenning, "Direct Detection of Halide Migration and its Link to Photoluminescence in a

Thin Hybrid Perovskite Single Crystal," Spring Materials Research Society, Phoenix, AZ, March 2018.

- Rory Runser. Solution drawing of ultra-thin conjugated polymer films for large-area solar tarps. Emerging Material Technologies Summit, Hanoi, Vietnam, November 2018.
- Yanqi Luo, J-P Correa-Baena, T. M. Brenner, J. Snaider, S. Sun, X. Li, M. A. Jensen, L. Nienhaus, S. Wieghold, J. R. Poindexter, S. Wang, Y. S. Meng, T. Wang, B. Lai, M. G. Bawendi, L. Huang, T. Buonassisi, and D. P. Fenning, "Halide Homogenization vs. Cation Segregation: A Balancing Act to achieve High-Performance Alloyed Perovskite Solar Cells," Spring Materials Research Society, Phoenix, AZ, April 2019.
- Yanqi Luo, P. Parikh, T. M. Brenner, J.-P. Correa-Baena, T. Buonassisi, Y. S. Meng, D. P. Fenning, "Quantitative Specifications for Successful E-beam Induced Current Microscopy of Halide Perovskite Devices," IEEE Photovoltaic Specialists Conference, Chicago, IL, June 2019.
- Yanqi Luo, J.-P. Correa-Baena, T. M. Brenner, J. Snaider, S. Sun, X. Li, M. A. Jensen, L. Nienhaus, S. Wieghold, J. R. Poindexter, S. Wang, Y. S. Meng, T. Wang, B. Lai, M. G. Bawendi, L. Huang, T. Buonassisi, and D. P. Fenning, "Halide Homogenization vs. Cation Segregation: A Balancing Act to Achieve High-Performance Alloyed Perovskite Solar Cells," IEEE Photovoltaic Specialists Conference, Chicago, IL, June 2019.
- David P. Fenning, "Shining Light on the Complex Compositional Landscape in Halide Perovskite Absorbers," Molecular Foundry User Meeting, Berkeley, CA, August 2019.
- Rory Runser, Solution drawing of ultra-thin conjugated polymer films, SPEC Center Elevator Pitch competition, UC San Diego, October 2019.
- Moses Kodur, D. P. Fenning, "Leveraging Electrochemical Techniques to Augment and Accelerate Halide Perovskite Technology Development," 2020 Virtual Materials Research Society Spring/Fall Meeting.
- Yanqi Luo, "The Impacts and Origins of A-Site Instability in Methylammonium- Free Perovskite Solar Cells Under Extended Operation," 47th IEEE Photovoltaic Specialists Conference, virtual meeting, June, 2020.
- Yanqi Luo and David P. Fenning, "A Bird's Eye View of Composition-Performance Relationships in Halide Perovskites via Correlative Microscopy," Spring and Fall joint Materials Research Society, Phoenix, December 2020.

Conference Presentations (Posters)

1. Y. Luo, S. Aharon, M. Stuckelberger, E. Magaña, B. Lai, M. I. Bertoni, L. Etgar, D. P. Fenning, "Nanoscale Halide Segregation Determines Charge Collection in Mixed-Halide Hybrid Perovskite Solar Cells," Spring Materials Research Society, Phoenix, AZ, March 2017.
2. Y. Luo, X. Li, M. Kodur, D. P. Fenning, "Stabilizing Next Generation Perovskite PV Modules," 2018 Annual EPIC Symposium, Sacramento, CA, February 2018.

3. Rory Runser, Samuel E. Root, Derick E. Ober, Charles Dhong, Darren J. Lipomi. Interfacial drawing of ultra-thin polymer films for large-area solar tarps. Jacobs Research Expo, UC San Diego, April 2018.
4. Rory Runser, Samuel E. Root, Derick E. Ober, Charles Dhong, Darren J. Lipomi. Interfacial drawing of ultra-thin polymer films for large-area solar tarps. UP Summit (Understanding and Protecting Our Planet), UC San Diego Supercomputing Center, May 2018.
5. Rory Runser, Samuel E. Root, Derick E. Ober, Charles Dhong, Darren J. Lipomi. Interfacial drawing of ultra-thin polymer films for large-area solar tarps. Nano XPo, UC San Diego Nanoengineering, May 2018.
6. M. Kodur, D. P. Fenning, "Increasing Perovskite Solar Cell Lifetimes Through Graphene Encapsulation," Sustainable Nanotechnology Conference Organization, San Diego, CA, November 2019.
7. Rory Runser, Samuel E. Root, Derick E. Ober, Charles Dhong, Armando D. Urbina, Kartik Choudhary, Alex Chen, Darren J. Lipomi. Roll-to-Roll Fabrication of Large-Area Solar Tarps via Interfacial Drawing. Jacobs Research Expo, UC San Diego, 2019.